Investigation of Electrodeposited Magnetite Films: Formation and Characterization

Chien-Lung Teng

Thesis submitted in fulfilment of the requirements for the degree of Doctor of Philosophy of Imperial College London

2008

Acknowledgement

Firstly I greatly appreciate Dr. Mary Ryan for her guidance throughout this work. I think I could not have not done this thesis without her support and encouragement either on my project or life.

Also I would like to thank the members of Dr. Mary Ryan's research group, Thanawat Meesak, Eleanor Schofield, Hao Wang, Benoit Illy, Rong Zhu and Steven Feng for help and many useful discussions, and the following individuals from Materials and Physics Department, Richard Sweeney, Dr. Mahmound Ardakani, Richard Chater and Dr. Will Branford for help on experimental work. Dr. Michael Tony, Dr. Bridget Ingham (Stanford Synchrotron Radiation Center, USA) Professor Ru–Shi Liu (National Synchrotron Radiation Research Center, Taiwan) for assistance on synchrotron X-ray scattering and absorption techniques.

I would like to acknowledge the award of an Overseas Research Students (ORS) Scholarship and departmental funding that enabled this work to be fulfilled.

Finally, I would like to thank my family for their love and support, particularly my Mum.

Abstract

Magnetite (Fe_3O_4) is of both scientific and technological interest because of its fascinating magnetic properties. It has a high Curie temperature of 860 K and a theoretical 100% spin polarization at the Fermi level. There are a variety of deposition techniques to form thin films of magnetite, such as molecular beam epitaxy (MBE), pulsed laser deposition (PLD), iron oxidation, sputtering and so on. In comparison with other deposition methods mentioned above, electrodeposition has a key advantage of relatively low processing temperature. The intention of this work was to investigate magnetite (Fe_3O_4) thin films grown *via* an electrochemical route by using various kinds of characterization techniques, especially on morphology, chemical composition, structure and magnetic properties. Fe_3O_4 thin films were obtained by using a galvanostatic or potentiostatic deposition from simple aqueous solutions of ferrous salts.

Iron oxide thin films have been grown at different current densities and temperatures onto polycrystalline copper substrates. XRD results indicate that Fe_3O_4 is formed at 90 ^oC at an applied current density of 0.05 $mA \cdot cm^{-2}$. Lower growth temperatures can cause the formation of another phase, α-FeOOH at a certain concentration of Fe^{2+} and pH buffer. Time-dependent growth of the iron oxides exhibits nucleation and coalescence. In order to obtain uniform Fe_3O_4 film surface, longer deposition times are needed.

The influence of applied potential on the characteristics of the deposited iron oxide was examined. The formation of Fe_3O_4 in a low potential regime (< 100 mV) *vs.* gold reference electrode while iron oxyhydroxides such as goethite (α-FeOOH) and lepidocrocite (γ-FeOOH) are favoured for E > 100 mV. The magnetic properties of the films were found to be strongly dependent on the deposition potential.

The multi-layer structure of Fe_3O_4/α-FeOOH/Fe_3O_4 onto NiO/Ni substrates has been demonstrated *via* successive deposition. A TEM cross-section image shows α-FeOOH is coherently formed between two ferromagnetic layers. ADF-STEM micrographs

show that Fe_3O_4 has a columnar structure and has less composition variation compared to that grown onto a polycrystalline copper substrate.

Synchrotron techniques, *i.e.* x-ray absorption near edge structure (XANES) and x-ray magnetic circular dichroism (XMCD), were performed to examine the iron oxide film. Fe *K*-edge x-ray absorption spectra demonstrate that the films grown at low potential regime (< 100 mV) have a comparable valency state with the standard Fe_3O_4 sample. The identification of the iron oxide was further confirmed by using XMCD technique. The calculation of the asymmetry ratio suggests that the total magnetic moment increased with decreasing applied potential. In addition, vibrating sample magnetometer (VSM) data show that the magnetic response is somewhat slower for the iron oxide grown at higher potential regime.

A change of pH in the electrolyte does not change the lattice constant and film morphology or texture but does affect particle sizes in Fe_3O_4 thin films. This decrease with the pH is due to the reaction of $FeOH^+$ ions with molecular oxygen in electrolyte.

Contents

Acknowledgement 1
Abstract 2
Contents 4
List of Figures 6
List of Tables 10
Definitions/Abbreviations 11
1. Introduction 13
2. Literature review 18
2.1 Crystal structure 18
2.2 Electrical properties 20
2.3 Magnetic properties 22
2.4 Deposition of magnetite films 27
2.4.1 Growth of polycrystalline magnetite 27
2.4.2 Growth of single crystalline magnetite 32
2.5 Growth mechanism by electrodeposition 39
3. Experimental 45
3.1 Substrate preparation 45
3.2 Electrochemical apparatus setup 46
3.3 Characterization techniques 48
3.3.1 Atomic force microscope 48
3.3.2 Scanning electron microscope 50
3.3.3 X-ray diffraction 53
3.3.4 Transmission electron microscope 55
3.3.5 Vibrating sample mangetometer 57
3.3.6 Synchrotron x-ray diffraction 59
3.3.7 Synchrotron x-ray absorption techniques 61
4. Results and Discussion 66
4.1 Growth of nanocrystalline Fe_3O_4 on to polycrystalline copper substrates 66
4.2 Time-dependent growth of Fe_3O_4 onto gold/glass substrates 82
4.3 Growth of multilayered Fe-based oxides 86
4.4 Influence of buffer concentrations on structure, film morphology and magnetic properties 97
4.5 Influence of deposition potential on structure, film morphology and magnetic properties 101
5. Conclusions 122

6. Future work 125
Appendices 127
A-1: Nernst Equation 127
A-2: Derivation of Steady-State Current Density [69] 128
A-3: Calculation of crystallite site using Scherrer equation 131
A-4: The Rocking Curves of Ni {100}<001> Tape 131
A-5: X-ray diffraction patterns 132
A-5-1: Nickel, syn (JCPDS No. 04-0850) 132
A-5-2: Copper, syn (JCPDS No. 04-0836) 132
A-5-3: Gold, syn (JCPDS No. 04-0784) 133
A-5-4: Magnetite, syn (JCPDS No. 19-0629) 133
A-5-5: Hematite, syn (JCPDS No. 33-0664) 135
A-5-6: Maghemite-C, syn (JCPDS No. 39-1346) 136
A-5-7: Goethite, syn (JCPDS No. 29-0713) 138
A-5-8: Lepidocrocite, syn (JCPDS No. 44-1415) 139
References 141

List of Figures

Figure 1.1: Progress of areal density of magnetic hard disk drivers as a function of calendar year [3]. 13
Figure 1.2: Price of gigabyte of data on a hard disk drive as a function of calendar year [3]. 14
Figure 1.3: Basic devices structures of spin valve and magnetic tunnel junction. 15
Figure 2.1: Inverse spinel structure of Fe_3O_4. 19
Figure 2.2: Phase diagram of Fe-O system [16]. 20
Figure 2.3: Conductivity of single crystal Fe_3O_4 plotted as a function of reciprocal temperature [19]. 21
Figure 2.4: Orthorhombic deformation of the cubic structure of Fe_3O_4 at 115 K. (dash and solid lines represent before and after Verwey transition) [24] 22
Figure 2.5: Band diagrams for different types of half-metals [27]. 23
Figure 2.6: (a) Illustration of spin direction and (b) incomplete cancellation of spins showing ferromagnetic ordering in Fe_3O_4. 24
Figure 2.7: Magnetoresistance for various kinds of Fe_3O_4 at room temperature. (a) powder; (b) thin film; (c) single crystal [33]. 26
Figure 2.8: Schematic representation of the principle of ferrite-plating process [41]. 30
Figure 2.9: The potential-pH equilibrium of iron-water system at 25 ^oC [44]. 31
Figure 2.10: (a) The theoretical absorption for different Fe sites in the Fe_3O_4 lattice. (b) XAS and XMCD signals for two different iron oxide films [63]. 36
Figure 2.11: Schematic representation of charge transfer (a-b) and resulting potential difference (c-d) in an electrochemical reaction [66]. 39
Figure 2.12: Illustration of the quantum-mechanical tunnelling of a free electron through an energy barrier. (a) in vacuum; (b) in metal-electrolyte interface. (The red and blue dots denote a free electron and charged ions, respectively.) [66]..... 42
Figure 2.13: Schematic representation of the electrode surface during the deposition process [68]. 43
Figure 3.1: Schematic representation of a three-electrode cell apparatus. 47
Figure 3.2: Description of instrumental principle of an AFM. 49
Figure 3.3: Force curve. (green, red and blue solid lines represent repulsion force, attraction force and balanced force respectively) 50
Figure 3.4: Schematic representation of a Molecular Imaging PicoSPM. 50
Figure 3.5: Schematic representation of a SEM instrumental principle. 51
Figure 3.6: Different signal sources when a beam of electrons bombard sample surface. 52
Figure 3.7: Principle of x-ray diffraction. 53

Figure 3.8: Schematic representation of Bragg's law. 54
Figure 3.9: Bragg-Brentano geometry in X-ray Diffraction. 55
Figure 3.10: Schematic illustration of components in a typical TEM. 56
Figure 3.11: Schematic representation of vibrating sample magnetometer (VSM) [80]. 58
Figure 3.12: A typical hysteresis loop for a ferromagnetic material. 59
Figure 3.13: SPEAR machine at the SSRL [82]. 59
Figure 3.14: Schematic representation of x-ray scattering diffraction 60
Figure 3.15: Origin of EXAFS in condensed matters. (Solid and dash line indicate outgoing and scattering waves, respectively.) [85] 62
Figure 3.16: Schematic representation of a typical EXAFS spectrum. 62
Figure 3.17: Working principle of MCD. 64
Figure 3.18: (a) Beamline 11A of synchrotron radiation source at NSRRC; (b) Dragon spherical grating monochromator. 65
Figure 4.1: (a) Potential versus deposition time at different growth temperatures (i = 0.05 mA·cm^{-2}); (b) cyclic voltammograms at temperature of 90 ºC with a scan rate of 5 mV·s^{-1}. The arrow indicates potential theoretically calculated from Nernst equation (Appendix A-1). 68
Figure 4.2: (a) XRD patterns of films deposited at various different temperatures (i= 0.05 mA·cm^{-2}. The symbols "◯", "+" and "v" represent Fe_3O_4, α-FeOOH and Cu, respectively); (b) HRTEM micrograph of Fe_3O_4/Cu cross-section showing a smooth coherent interface and clear lattice planes (inset) in Fe_3O_4. Note that the strong background in the XRD data is due to substrate (Cu) florescence and is not related to the film itself. 69
Figure 4.3: FEGSEM micrographs of electrodeposited films at (a) 90 ^{o}C, (b) 75 ^{o}C, (c) 60 ^{o}C and (d) 95 ºC, showing clear changes in deposit morphology. 3(d) shows the development of pinhole type defects at the higher deposition temperature 71
Figure 4.4: AFM images show surface roughness. (a) $t_{deposition}$ = 30 min (rms roughness = 38 nm); (b) $t_{deposition}$ = 50 min (rms roughness = 30 nm). 72
Figure 4.5: FEGSEM image of Fe_3O_4 thin film grown at 0.05 mA·cm^{-2} for 30 min showing surface anomalies. 73
Figure 4.6: M-H loop of electrodeposited Fe_3O_4 thin film recorded at 290 K. 74
Figure 4.7: Composition variation (Fe:O ratio) of ferrite films with deposition time as determined by EDS analysis. 75
Figure 4.8: XRD patterns of films deposited at various applied current density. The symbols "◯" and "v" represent Fe_3O_4 and Cu, respectively. 76
Figure 4.9: FEGSEM micrographs of Fe_3O_4 prepared at 90^{o}C with (a) 0.005 mA·cm^{-2} and (b) 0.5 mA·cm^{-2} for 30 min. 77

Figure 4.10: Synchrotron x-ray scattering of Fe_3O_4/Cu substrate. (a) i = 0.005 mA·cm^{-2}; (b) i = 0.05 mA·cm^{-2}; (c) i = 0.5 mA·cm^{-2}. 79
Figure 4.11: STEM image of Pt/Fe_3O_4/Cu cross-section. (a) bright-field (BF) image; (b) annular dark-field (ADF) image. 81
Figure 4.12: Crystallography, topography and morphology of gold/glass substrates. (a) XRD; (b) AFM; (c) FEGSEM 83
Figure 4.13: Time-dependent growth of Fe_3O_4 onto gold/glass substrates at 80 ^oC under a constant potential of 25 mV. (a) 10 s; (b) 30 s; (c) 60 s; (d) 300 s; (e) 600 s; (f) 1800 s. 85
Figure 4.14: (a) SEM image of the RABiTS Ni Tape, (b) (111) pole figure of Ni{100}<001>. 87
Figure 4.15: AFM images of the Ni{100}<001> substrate. (a) before (rms roughness = 19 nm) and (b) after etching (rms roughness = 357 nm). 88
Figure 4.16: Bragg-Brentano scan of Fe_3O_4 thin film (~145 nm in thickness) deposited on air-formed nickel oxide on Ni{100}<001> substrate. 89
Figure 4.17: AFM images of Fe_3O_4 thin film show the detailed surface topography (a) before (rms roughness = 354 nm); (b) after (rms roughness = 132 nm). 89
Figure 4.18: (a) FEGSEM micrograph of Fe_3O_4 thin film reveals film morphology; (b) magnetite cubic structure with different facets. 90
Figure 4.19: (a) HRTEM image shows thickness of air-formed NiO is about 2 nm; (b) bright-field image; (c) annular dark-field (ADF) STEM image. The circle indicates the cluster has a loose structure in comparison with Fe_3O_4 film. 92
Figure 4.20: (a) A schematic illustration of Fe-oxide based spin manipulating device; (b) TEM micrographs of Fe_3O_4/α-FeOOH/Fe_3O_4 cross-section, showing two Fe_3O_4 layers separated by α-FeOOH; (c) loose α-FeOOH interlayer found grown on Fe_3O_4. (red dashed line represents the interface between Fe_3O_4 and α-FeOOH) 95
Figure 4.21: (a) Synchrotron x-ray scattering spectrum under an accelerating voltage of 7001.5 eV. The symbols “o”, ”+”and ”v” represent Fe_3O_4, -FeOOH and Ni. (b) a plot of FWHM *vs.* sin for Fe_3O_4 showing there is not apparent anti-phase boundary present. The average crystal size is 35 nm. 96
Figure 4.22: pH measurement for electrolytes containing 0.01M $(NH_4)_2Fe(SO_4)_2{\cdot}6H_2O$ at different concentrations of CH_3COOK. 97
Figure 4.23: X-ray diffraction patterns of Fe_3O_4 films grown at different concentrations of CH_3COOK at 25 mV *vs.* Au electrode. 98
Figure 4.24: Average particle size and lattice constant of Fe_3O_4 grown at different concentrations of CH_3COOK. 99
Figure 4.25: FEGSEM micrographs of Fe_3O_4 films grown at different concentrations of CH_3COOK: (a) 0.05 M; (b) 0.075 M; (c) 0.1 M; (d) 0.25 M; (e) 0.5 M. 100

Figure 4.26: XRD patterns of iron oxide thin films on copper foils at various potential *vs.* Au reference electrode. (The symbols "*", "□", "Δ", and "○" represent Cu, Fe_3O_4, α-FeOOH and γ-FeOOH, respectively. The symbol "+" indicates that the sample is annealed at 400 ^oC under vacuum for 5 mins) 103
Figure 4.27: Plot of lattice constant as function of θ for Fe-oxide films deposited at different applied *E*, Extrapolation to 90^o provides accurate calculation of a_0. (The symbol "+" indicates that the sample is annealed at 400 ^oC under vacuum) 104
Figure 4.28: Average particle size and strain of Fe_3O_4 grown at different applied potentials calculated *via* Williamson-Hall approach. (open symbols at 50 mV indicate that the sample was annealed) 104
Figure 4.29: FEGSEM micrographs of iron oxide thin films on copper foils at various potential *vs.* Au reference electrode. (a) 400 mV; (b) 200 mV; (c) 100 mV; (d) 50 mV; (e) 25 mV; (f) 10 mV; (g) 5 mV; (h) -5 mV 107
Figure 4.30: FEGSEM micrographs of iron oxide thin films on Cu/Si substrates. (a) 400 mV; (b) 200 mV; (c) 100 mV; (d) 50 mV: (e) 25 mV; (f) 10 mV. 108
Figure 4.31: (a) Normalized Fe *K*-edge x-ray absorption spectra of the standard samples; (b) details of pre-edge features in (a). 111
Figure 4.32: (a) Fe *K*-edge x-ray absorption spectra of the iron oxides compared with the standard samples; (b) details of pre-edge features in (a). 112
Figure 4.33: X-ray absorption spectrum of Fe_3O_4 thin film (a) without and (b) with an applied magnetic field of 1 T under a drain current mode operation. 116
Figure 4.34: Fe $L_{2,3}$-edge MCD spectra of Fe_3O_4 grown at various potentials *vs.* Au reference electrode. 117
Figure 4.35: Schematic representation of Fe-oxide grown on to the copper substrate at 100 mV *vs.* Au reference electrode. 118
Figure 4.36: (a) Taking an example (100 mV case) showing the indications of the coercivity (H_c), remanent (M_r) and saturation magnetization (M_s). (b) Magnetic hysteresis loops of iron oxide films grown at various potentials *vs.* Au reference electrode recorded with respect to applied filed in-plane at 300 K. 120
Figure 4.37: Temperature dependence of magnetic hysteresis loops of the iron oxide films grown at 50 mV *vs.* Au reference electrode measured with applied field in-plane. 121

List of Tables

Table 1.1: The composition and dimensions of the spin-valve memory [11]. 16
Table 2.1: Material properties of the iron oxides [18]. 19
Table 2.2: Comparison of morphology and magnetic properties for Fe_3O_4 prepared at different deposition techniques. 38
Table 3.1: The cleaning procedure for Ni substrates. 45
Table 3.2: The standard RCA clean procedure [72]. 46
Table 3.3: Deposition parameters investigated in this present work. 47
Table 4.1: Lattice constants extracted using the three main diffraction peaks in Fe_3O_4 (Unit: nm; the symbol "*" represents an overlap peak) 79
Table 4.2: EDS analysis of electrodeposited Fe_3O_4 (all results in atomic %) 91
Table 4.3: Comparison of relative intensity between standard Fe_3O_4 (JCPSD No. 19-0629) and electrodeposited Fe_3O_4 film grown at different concentrations of CH_3COOK. ("*" and "-" represent the overlap and no-detectable peak, respectively) 98
Table 4.4: Calculation of MCD asymmetry ratio from Fe L_2-edge from XAS spectra (The Symbol "*" denotes the sample has been annealed before measurement) 117

Definitions/Abbreviations

AFC	Antiferromagnetically coupled
AFM	Atomic force microscopy
c.c.p.	Cubic close-packed
CGR	Compounded growth rate
CPP	Current-perpendicular-to-plane
CFSE	Crystal field stabilization energy
EDS	Energy dispersive x-ray spectroscopy
EMF	Electromotive force
EXAFS	Extended x-ray absorption fine structure
FC	Field-cooled
FEGSEM	Field-emission-gun scanning electron microscopy
FIB	Focused ion beam
FWHM	Full width at half maximum
GMR	Giant magnetoresistance
HDD	Hard disk drive
HRTEM	High resolution transmission electron microscope
JCPDS	Joint Committee on Powder Diffraction Standards
MBE	Molecular beam epitaxy
MR	Magnetoresistance
MRAM	Magnetoresistance random access memory
MTJ	Magnetic tunnel junction
NHE	Normal hydrogen electrode
PNR	Polarized neutron reflectivity
PLD	Pulsed laser deposition
PR	Perpendicular recording
PSD	Position-sensitive detector
PSD	Pseudo-single-domain
RABiTS	Single-phase rolling-assisted biaxially textured substrate
rf	Radio-Frequency
rms	Root-mean-square
SD	Single-domain
SEM	Scanning electron microscopy
SNR	Signal to noise ratio
SSP	Soft solution process

STM	Scanning tunneling microscopy
STEM	Scanning Tunneling electron microscopy
TEM	Transmission electron microscopy
TGA	Thermo-gravimetric analysis
VSM	Vibrating sample magnetometer
WDS	Wavelength dispersive x-ray spectroscopy
XANES	X-ray absorption near edge structure
XAS	X-ray absorption spectroscopy
XMCD	X-ray magnetic circular dichroism
XPS	X-ray photoelectron spectroscopy
XRD	X-ray diffraction
ZFC	Zero-field-cooled
1D	One dimension

1. Introduction

The giant magnetoresistance (GMR) effect has recently attracted much interest because of its applications in spin manipulating devices such as magnetic recording, galvanic isolator and non-volatile memories [1, 2]. In terms of magnetic data storage, the storage density of hard disk drives has dramatically increased by about eight orders of magnitude since the fist hard-disk drive appeared in 1950's owing to the rapid development of device technology (Figure 1.1). Yet the cost of making devices has exponentially dropped at the same time [3]. As can be seen in Figure 1.2, nowadays it is much cheaper to store information on a hard drive than the same size information on paper.

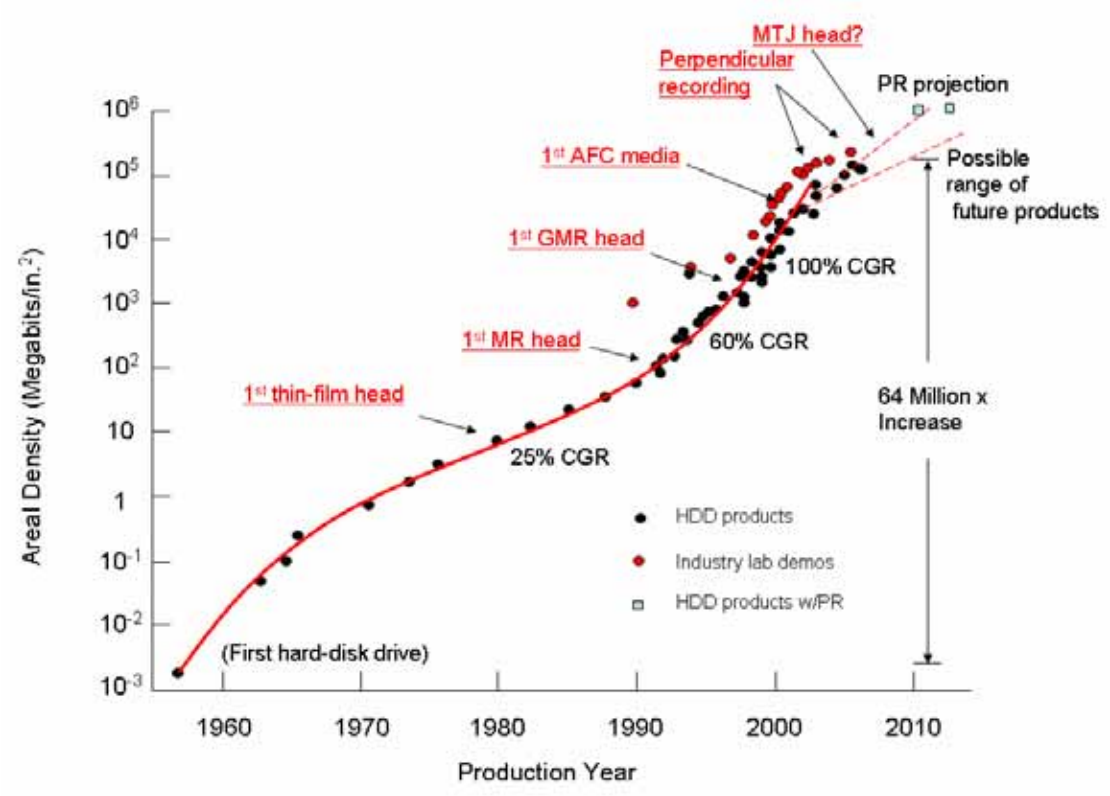


Figure 1.1: Progress of areal density of magnetic hard disk drivers as a function of calendar year [3].

To approach higher storage density and lower cost for magnetic storage devices, the design architecture and the selection of magnetic media become important key factors.

Recently the design of longitudinal recording has been gradually replaced by the perpendicular one, where the magnetization of the bits lies in the plane of magnetic film whereas the magnetization is normal to the plane of film. It is generally believed that perpendicular architecture allows the manufacture of high-density magnetic devices with a higher signal to noise ratio (SNR) [4]. Various materials including some transition metals (Fe, Co and Ni) and their alloys have been using for fabricating magnetic media or read heads. However, the intrinsic properties of the magnetic materials such as magnetic moment and saturation magnetization can be changed or diminished due to the presence of defects or impurities introduced during the integrated process. This will lead to a reduction in device performance. Therefore, the most difficult task to achieve high areal density is to tackle this problem.

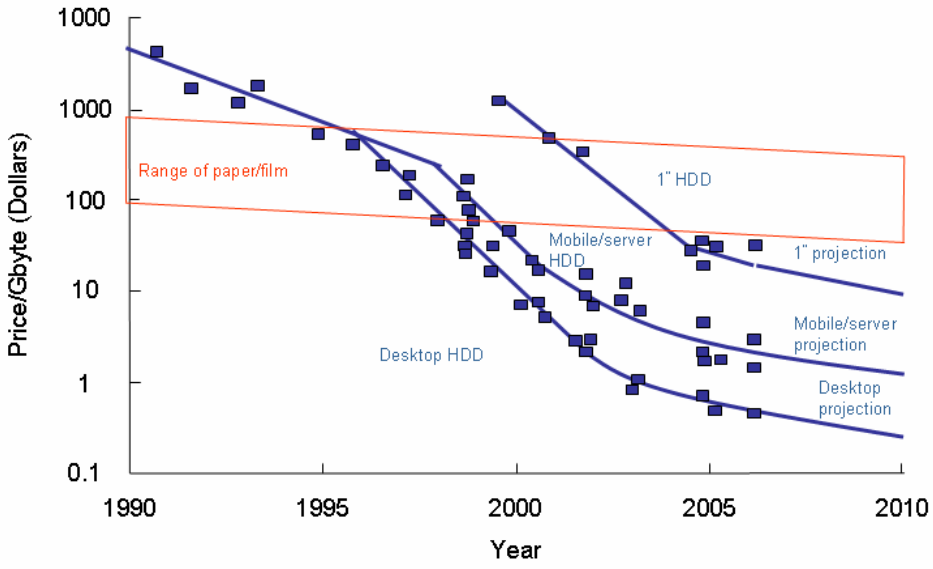


Figure 1.2: Price of gigabyte of data on a hard disk drive as a function of calendar year [3].

Two basic device structures, spin-valve and magnetic tunnel junction (Figure 1.3), are suggested for novel logic and memory application. Both of these devices have a sandwich structure, which consists of two ferromagnetic layers and one interlayer of either conductive or insulating material. The device operation is to utilise the transport of polarized electrons arising from imbalance of density of states for spin-up and spin-down electrons at the Fermi level. Consequently, junction magnetoresistance is produced.

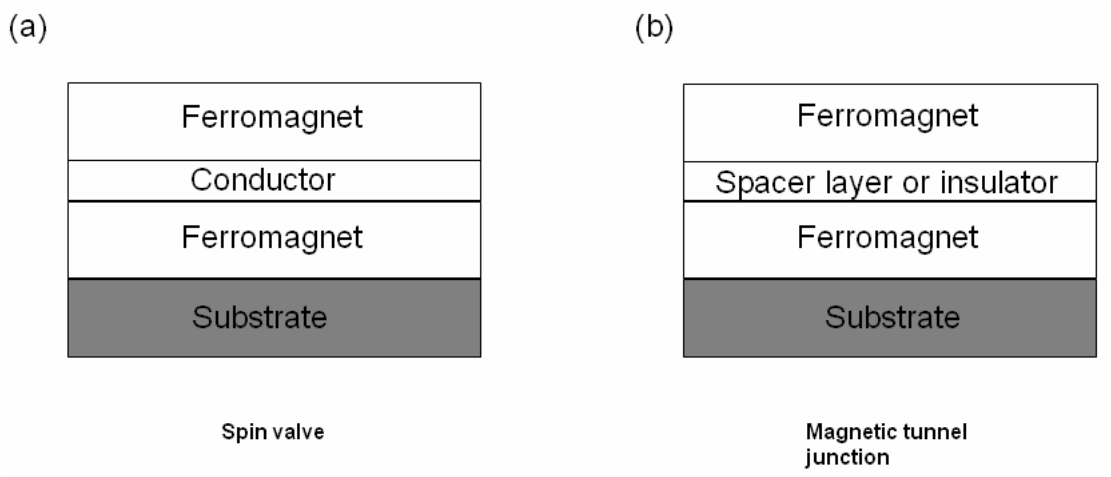


Figure 1.3: Basic devices structures of spin valve and magnetic tunnel junction.

Ferromagnetic materials have been studied for applications of electron-manipulating electron devices for decades. The spin tunneling current was first observed in a superconducting-ferromagnetic-metal structure by Tedrow *et al.* in 1973 [5]. Similar work was carried out by Julliere [6] showing spin-polarized tunneling in a sandwich structure (ferromagnet/insulator/ferromagnet) in which conduction electrons in a ferromagnetic metal were partly spin-polarized and tunnelled across the insulator which minimizes magnetic coupling between two ferromagnetic materials. Baibich *et al.* [7] discovered giant magnetoresistance in (001) Fe/ (001) Cr superlattices and suggested that this giant magnetoresistance was due to spin-dependent tunneling from Fe layers to Cr layers.

Many devices have been devised after the discovery of giant magnetoresistance. The spin valve consists of a soft ferromagnetic layer (free layer), a conducting spacer (usually copper) and a hard ferromagnetic layer (pinned layer) formed on artificial or natural anti-ferromagnetic substrates [8]. The resistance of the spin valve is determined by the orientation of spin between free layer and pinned layer. That means, current flows from the free layer to conductor as the spin directions are the same between the free and pinned layers. On the contrary, there is no current flow allowed if spin directions are different. Some studies have found that the magnetoresistance, corresponding to sensitivity, substantially increases by depositing the thin Co "nano-layers" on a copper spacer to enhance interface scattering [9, 10].

Magnetoresistance random access memories (MRAMs) are non-volatile memories

which use magnetic hysteresis and magnetoresistance to store and read data, respectively. The core structure of a contemporary MRAM is similar to the spin valve described previously. The concept of spin-valve memory originated from Irie *et al.* [11], using spin-valve multilayers composed of soft and semi-hard magnetic layers separated with non-magnetic layers. The detailed composition and dimensions proposed by Irie *et al.* are summarized in Table 1.1.

Spin-valve element	Composition	Thickness (nm)	Width (μm)
Free layer	$Ni_{80}Fe_{10}Co_{10}$	3.0	40
Pinned layer	$Co_{75}Pt_{25}$	7.4	40
Spacer	Cu	2.3	40
Sense line shunts	Au	300	> 40
Word line	Au	200	80

Table 1.1: The composition and dimensions of the spin-valve memory [11].

Motivation

In order to make spintronic devices more efficient, materials with high spin polarization are needed. Elemental ferromagnets and their alloys do not have 100% spin polarization because the density of states for spin-up and spin-down electrons is nearly equivalent. One of the leading candidates for spin transport devices is Fe_3O_4 because of its high spin polarization and high Curie temperature (860 K). With spin polarization of 100%, it becomes a half-metallic material and it is easy to fabricate electronic devices with a digital on-off function. Moreover, its high Curie temperature would enable spintronic devices to operate at or above room temperature.

There are a variety of deposition techniques to grow thin films of Fe_3O_4. Most of them are carried out under vacuum and with high processing temperatures (> 350 ^{o}C). There is no doubt that thin films grown in such conditions have advantages. For instance, the growth of thin films can be precisely controlled to reduce contaminations. However, vacuum equipment and high processing temperatures are most costly. Soft solution processing (SSP) is an alternative. By using the electrochemical routes, morphology and chemical composition of thin films can be controlled at a relatively

low processing temperature (< 200 ^{o}C) by adjusting processing conditions compared to deposition methods carried out under vacuum [12]. This minimises any inter-diffusion between layers in device structures.

Aims

The aim of this work was to study Fe_3O_4 electrochemically grown on to diamagnetic substrates to assess the feasibility of such a route for spintronic applications. Since the processing window to obtain a pure single phase of Fe_3O_4 is very narrow, it is important to be able to control the system carefully and understand the effect of small potential variations on the material properties. Specifically the aim was to determine the effect of processing conditions on the film structure and chemistry, and hence understand differences in magnetic behaviour of the material. The expected outcome of the work will be to provide a complete description of the material, facilitated by the use of a suite of advanced characterization methods to elucidate the film structure, chemistry, morphology and magnetic properties. This will provide guidance for further developments towards device processing.

The thesis was divided into chapters in order to explore magnetite. Chapter 2 details the crystal structure, electrical and magnetic properties of magnetite. The preparation *via* a variety of deposition techniques will be thoroughly discussed. Chapter 3 is the experimental section including substrate preparation, apparatus set-up and working principles of the characterization instruments used in this work. Chapter 4 examines the influence of various processing parameters such as anodic current density, applied potential, deposition temperature, solution chemistry as well as the choice of substrates. Results of phase identification, film morphology and magnetic properties of the deposited iron oxides films will be presented. Chapter 5 is the summary and discussion of the work in this thesis. Finally, Chapter 6 discusses possible future developments leading on from this work.

2. Literature review

2.1 Crystal structure

Magnetite (Fe_3O_4) has an inverse spinel structure (space group *Fd3m*) with a lattice constant of 0.8391(7) nm, where all tetrahedral (A) sites are occupied by half of Fe^{3+} ions, whereas octahedral (B) sites are occupied by equal numbers of Fe^{2+} and Fe^{3+} ions in a cubic close-packed (c.c.p.) assembly of O^{2-} ions [13, 14]. The atomic arrangement in Fe_3O_4 is a result of Fe^{2+} having six 3*d* electrons at octahedral sites with a higher crystal field stabilization energy (CFSE) of 11.9 kcal·mol^{-1} than tetrahedral sites about 7.9 kcal·mol^{-1}. In contrast, there is no site preference for Fe^{3+} which has zero CFSE at both A and B sites [15]. The inverse spinel structure of Fe_3O_4 is depicted in Figure 2.1. In a unit cell of Fe_3O_4, Only 8 of the 64 possible tetrahedral sites are occupied and 16 of the 32 possible octahedral sites are occupied. Therefore, there are one A site and two B sites in each formula unit. Different derivatives of Fe-oxides can be obtained depending on the Fe oxidation states. The phase diagram of Fe-O as shown in Figure 2.2 describes the equilibrium states of various iron oxides at certain temperature and oxygen compositions [16]. Structurally FeO and γ-Fe_2O_3 are similar to Fe_3O_4. All of them contain 32 c.c.p. oxygen atoms in a unit cell of edge approximately 0.85 nm and are easily convertible to each other. That is, Fe_3O_4 can be oxidized into γ-Fe_2O_3, which is reduced back to Fe_3O_4 by heating under vacuum [17]. Generally, iron oxides are common compounds present on earth such as ores, rocks and waters. The formation of iron oxides is mainly caused by aerobic weathering of magmatic rocks [18]. According to Table 2.1, Fe_3O_4 is the most stable phase in terms of thermodynamics (formation energy). Nevertheless, the phase window to prepare single phase Fe_3O_4 by artificial methods is narrow.

Mineral name	***Wüstite (FeO)***	***Magnetite (Fe_3O_4)***	***Maghemite (γ-Fe_2O_3)***	***Hematite (α-Fe_2O_3)***	***Goethite (α-FeOOH)***	***Lepidocrocite (γ-FeOOH)***
Crystal structure	Cubic	Cubic	Cubic/ tetragonal	Rhombohedral hexagonal	Orthorhombic	orthorhombic
Cell dimension (nm)	a = 0.4302-0.4275	a = 0.8396	a = 0.83474	a = 0.50356(1) c = 1.37489(7)	a = 0.9956 b = 0.30215 c = 0.4608	a = 0.307 b = 1.253 c = 0.388
Formula units, per unit cell, Z	4	8	8	6	4	4
Density (g·cm^{-3})	5.9-5.99	5.18	4.87	5.26	4.26	4.09
Colour	Black	Black	Reddish-brown	Red	Yell-brown	Orange
Type of magnetism	A	F*	F	Weakly A or F	A	A
Néel (Curie) temperature (K)	203-211	850	820-986	956	400	77
Standard free energy of formation ΔG_f^0 (kJ·mol^{-1})	-251	-1012.6	-711.1	-742.7	-488.6	-477.7

(Symbols "A", " F" and "F*" denote antiferromagnetic, ferromagnetic and ferrimagnetic, respectively.)

Table 2.1: Material properties of the iron oxides [18].

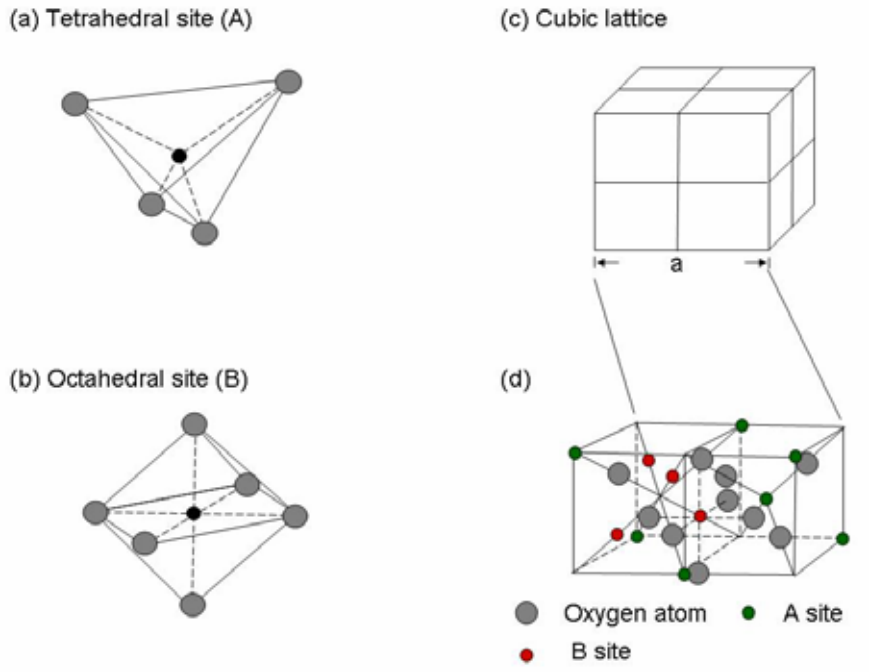


Figure 2.1: Inverse spinel structure of Fe_3O_4.

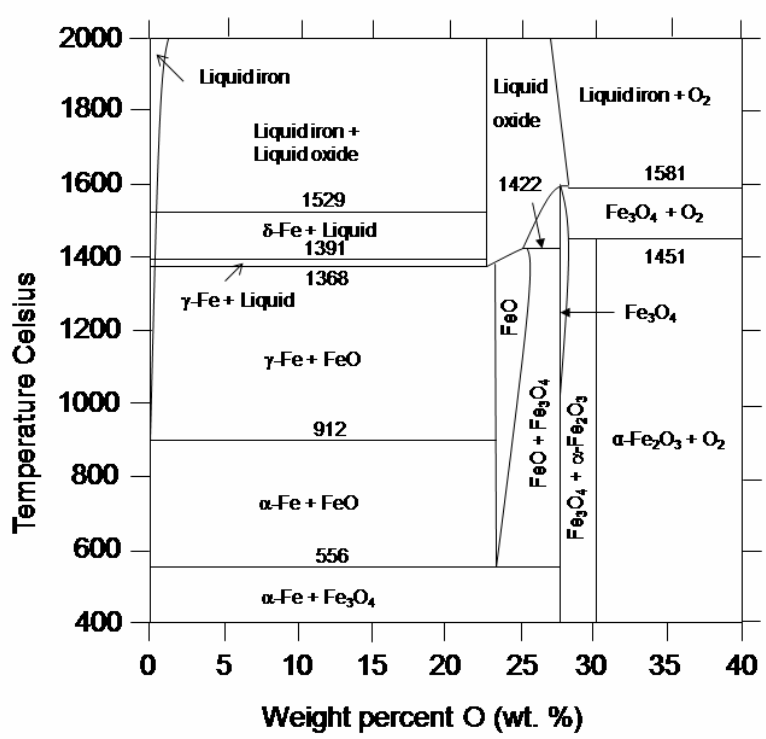


Figure 2.2: Phase diagram of Fe-O system [16].

2.2 Electrical properties

Fe_3O_4 behaves like a semiconductor, with a band gap of 0.1 eV [18]. The electronic conductivity is around 200 $ohm^{-1} \cdot cm^{-1}$ at room temperature and reaches a maximum at near 355 K, above which Fe_3O_4 shows a metallic behaviour (Figure 2.3) [19]. Above Curie temperature (T_c), the new rise on electrical conductivity is possibly due to a higher energy transfer process between cations and O^{2-} ions. The unusual electrical property can be accounted for the continuous charge-hopping process between Fe^{2+} and Fe^{3+} ions in the octahedral sites, by which electrons can be thermally excited in the 16-fold position [20]. As a result, none of the tetrahedral Fe^{3+} ions take part in the conduction process.

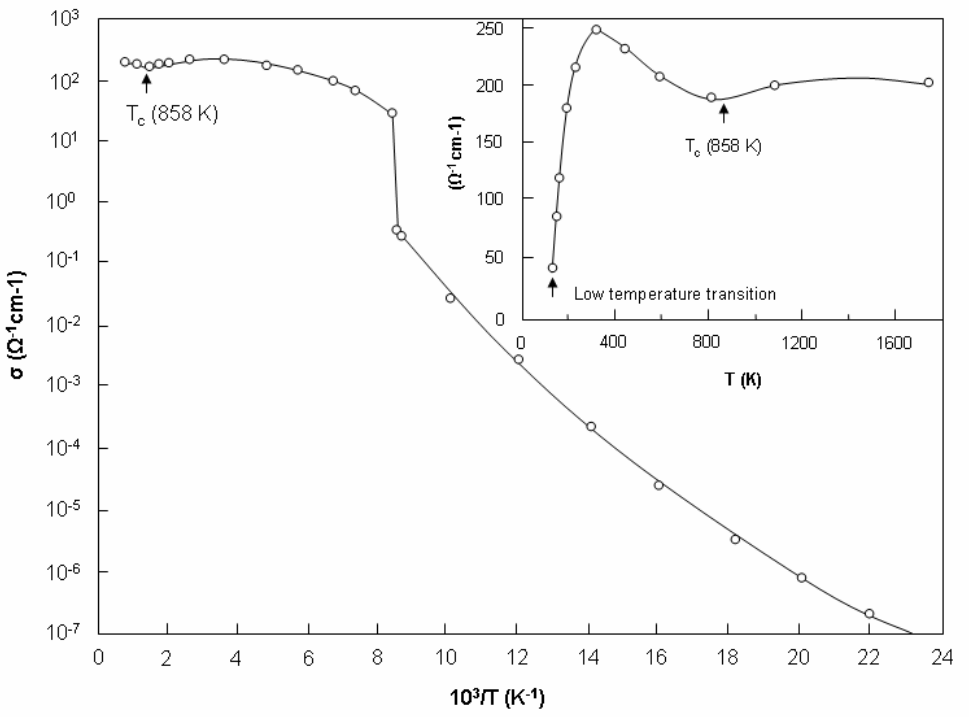


Figure 2.3: Conductivity of single crystal Fe_3O_4 plotted as a function of reciprocal temperature [19].

In the case of Fe_3O_4, the electrical resistivity tends to increase with decreasing temperature. Verwey [21] found that the value of electric resistance had a slight increase as temperature dropped down from 300 K to 120 K. However, an abrupt increase of the resistance occurred at approximately 117 K by a factor of about 100. This is the so-called Verwey transition, below which Fe_3O_4 becomes paramagnetic and the crystal structure changes from cubic to monoclinic, and ordering of the Fe^{2+} and Fe^{3+} occurs [22, 23]. According to the strain gauge measurements for the natural single crystal of magnetite examined by Bickford [24], the c axis of orthorhombic structure is 0.0302% smaller in dimension relative to the cubic crystal at 130 K. The face diagonal $\overline{QS}$ becomes 0.0696% smaller and the face diagonal $\overline{PR}$ becomes 0.0594% larger (Fig 2.4). Additionally, x-ray diffraction measurement showed the lattice distortion became larger with decreasing temperature [25].

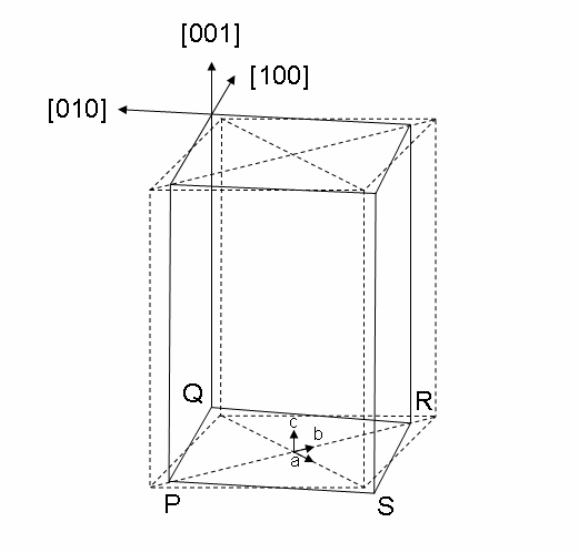


Figure 2.4: Orthorhombic deformation of the cubic structure of Fe_3O_4 at 115 K. (dash and solid lines represent before and after Verwey transition) [24]

2.3 Magnetic properties

Magnetism is the phenomenon by which materials exhibit an attractive or repulsive force on other materials. The magnetic behaviour is usually represented by the magnetic field strength (*H*) and magnetic induction (*B*). The magnetic field strength is the intensity of the externally applied magnetic field; whereas the magnetic induction implies the magnitude of the internal field strength within a substance subjected to an *H* field. The units of *H* and *B* in the c.g.s. system are Oersted and Gauss, respectively. Both are field vectors with a specific magnitude and direction. The magnetization (*M*) is another field quantity to describe the magnetism. *M* reveals that the total magnetic moment per unit volume that exists in a substance, and is proportional to the applied field. There are several types of magnetism: ferromagnetism, ferrimagnetism and antiferromagnetism. Ferromagnetism is the permanent magnetization in which the parallel alignment of neighbouring magnetic moments is present in a substance. Generally, it can be found in transition metals such as Fe, Co and Ni. Ferrimagnetism results from antiparallel spin coupling and incomplete magnetic moment cancellation. For antiferromagnetic materials, there is no net magnetic moment present because of the complete cancellation of magnetic moments within the material.

Fe_3O_4 is ferrimagnetic with the highest known Curie temperature (about 860 K) and its conduction electrons have a 100% spin polarisation at the Fermi level. Such magnetic material is regarded as a half-metallic material in which the band structures for spin-up and spin-down electrons are asymmetric [26]. Various half-metals have been examined both experimentally and theoretically, and can be categorized into four types shown below. (Figure 2.5) The subscript A or B depends on whether the direction of conduction electrons is spin-up or spin-down, respectively. Fe_3O_4 belongs to a type II_B half-metal whose Fermi level sits at the mostly unfilled band, with only minority spin in the t_{2g} state of $3d^{\downarrow}$ band present around it, as the majority spin band is fully occupied [27].

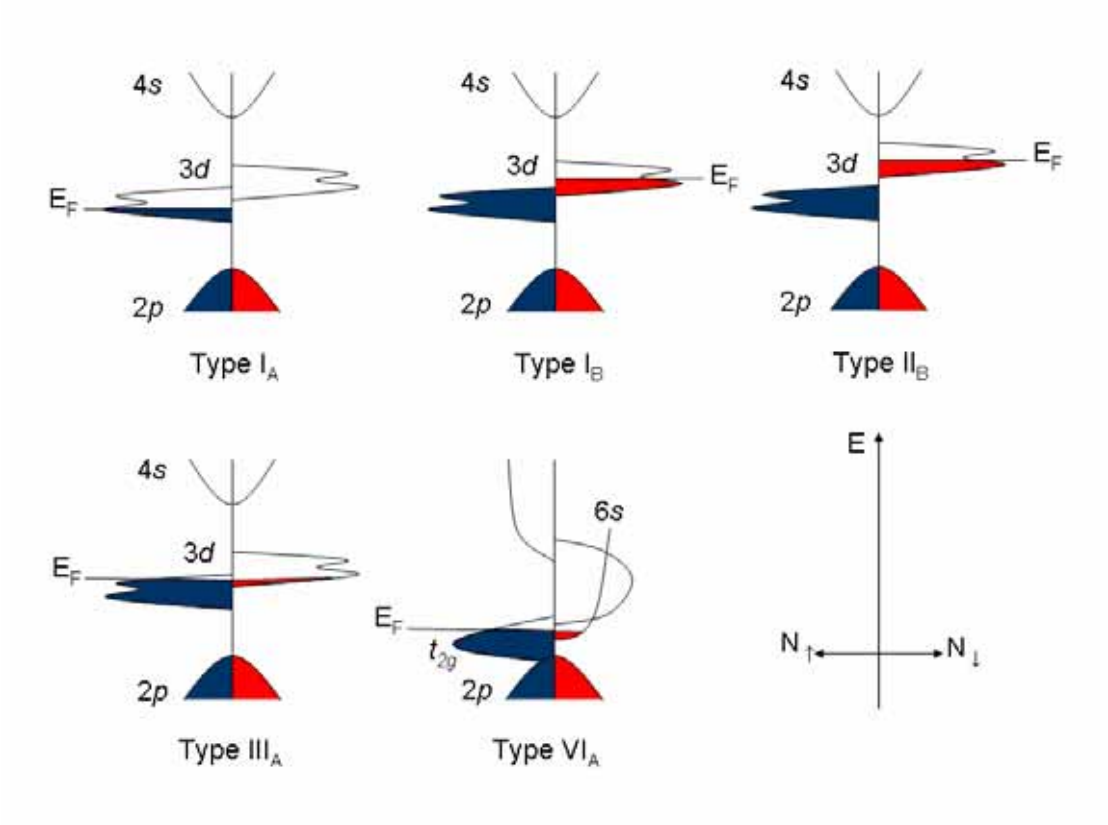
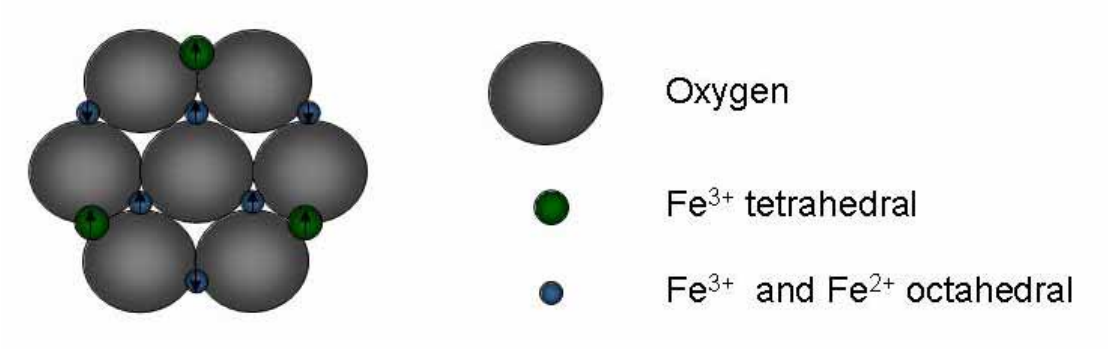


Figure 2.5: Band diagrams for different types of half-metals [27].

Figure 2.6 illustrates the spin directions of two and three valence Fe ions in Fe_3O_4. As can be seen, the spins of Fe^{3+} ions in tetrahedral sites (A) and Fe^{3+} ions in octahedral sites (B) cancel each other. As a consequence the net magnetization is only due to the Fe^{2+} ions in the octahedral sites, contributing a magnetic moment of 4 μ_B per formula unit. The measured value is 4.07 μ_B for the bulk magnetite. The

discrepancy is due to incomplete quenching of the orbital moment.

(a)



(b)

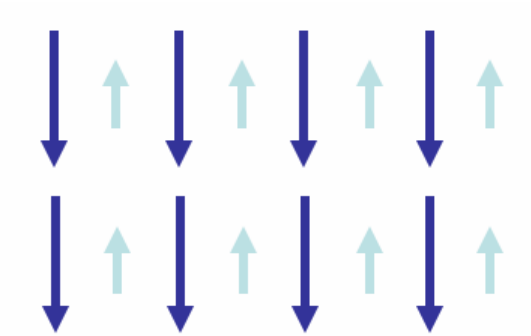


Figure 2.6: (a) Illustration of spin direction and (b) incomplete cancellation of spins showing ferromagnetic ordering in Fe_3O_4.

Spin polarisation is an important parameter to quantify the predominant spin electrons. It can be defined as

$$P = \frac{n\uparrow - n\downarrow}{n\uparrow + n\downarrow}$$

where $n\uparrow$ and $n\downarrow$ represent the spin-up and spin-down electron density, respectively. Generally, the value decreases with increasing temperature and drops to zero at the Curie temperature.

Tedrow *et al.* [5] measured spin polarisation for various ferromagnetic thin films including Fe (+44%), Co (+34%), Ni (+11%) and Gd (+4.3%). The positive observed values can be associated with the predominance of majority spin direction. It is worth

noting that the values obtained are largest with thin ferromagnetic films grown at room temperature. Experimental results showed the spin polarization changed as the films are less crystalline. Zhang *et al.* [28] theoretically predicted the band structure of Fe_3O_4 and found that only spin-down electrons are present and these electrons have Fe (B) character. They also suggested that minority spins were metallic, whereas majority spins were semi-conducting. The measurement of spin polarisation for Fe_3O_4 was carried out by Alcarado *et al.* [29]. A negative value of electron spin polarisation, around -40%, was observed. Higher spin polarisation was observed with a value of $-(80 \pm 5)\%$ at room temperature by means of spin-resolved photoelectron spectroscopy [30]. Note that the sign of spin polarisation is negative. This is a direct evidence of spin down electrons (minority spins) from Fe^{2+} at octahedral sites (B) present at the Fermi level. Nevertheless, the observed value of spin polarisation is less than the 100% predicted by Zhang *et al.*. This is possibly due to intrinsic restriction of the photoelectrical measurement method in which only a few layers of atoms on surface can be excited.

Apart from spin polarization mentioned previously, magnetoresistance (MR) has to be taken into account with the intention of making practical spin-manipulating devices.

The equation to calculate MR is

$$MR = \frac{R(0) - R(H)}{R(0)}$$

where R(0) and R(H) are the resistances in a zero-field and an applied field H, respectively. The magnitude of MR ratio is a function of magnetic field and temperature.

The origin of magnetoresistance can be explained by the change of relative orientations among ferromagnetic particles separated by grain boundaries [31] or interparticle contacts [32]. For magnetite, negative magnetoresistance has been observed in compressed powder and polycrystalline film regardless of the direction of

the applied field. However, there is no detectable magnetoresistance in the single crystal (Figure 2.7). In the compressed powder, the average contact resistance is determined upon particle size. It can be roughly estimated as ρ/d, where ρ and d are electrical resistance and particle size, respectively [33]. In the polycrystalline film, the total resistance is the sum of intrinsic resistance and grain-boundary resistance. The resistance contribution from grain boundaries is related to the probability of electron transport across grain boundary is proportional to $\cos^2 \theta/2$. (θ is the angle of magnetization of two adjacent grains) [34]

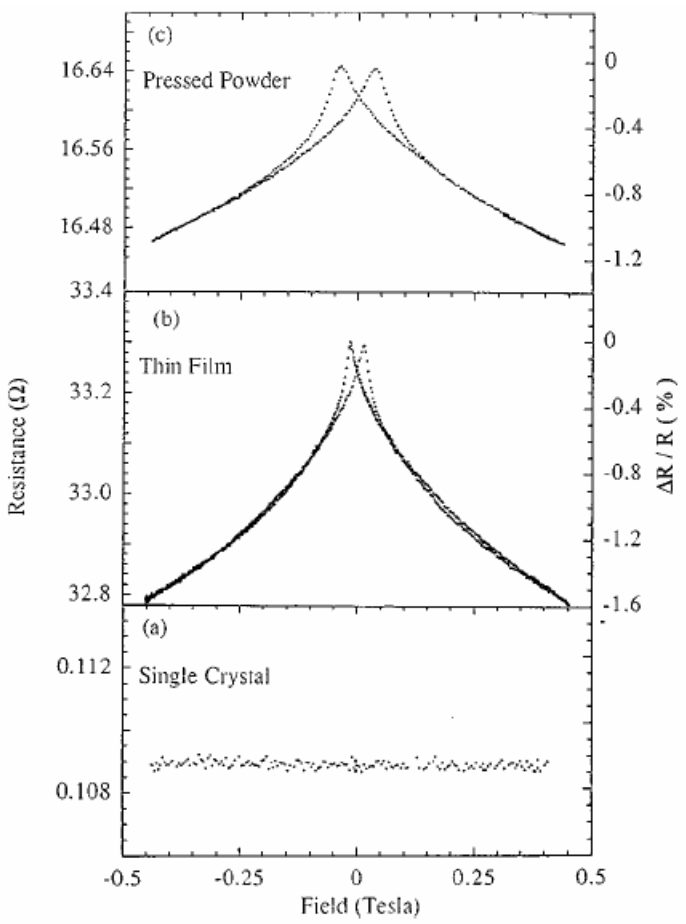


Figure 2.7: Magnetoresistance for various kinds of Fe_3O_4 at room temperature. (a) powder; (b) thin film; (c) single crystal [33].

2.4 Deposition of magnetite films

Thin films of Fe_3O_4 can be grown by several deposition techniques, such as sputtering, molecular beam epitaxy (MBE) and pulsed laser deposition (PLD) and so on. In general, these deposition processes can be divided into several sequential sub-steps: (1) In the beginning of deposition, the arriving atoms or molecules are adsorbed on the surface of the substrate by either physisorption or chemisorption; (2) These atoms or molecules can diffuse onto the surface and (3) form the bonds of the film material *via* a physical/ chemical reaction. (4) Consequentially, a process of so-called nucleation takes place. The nucleation process will depend on the magnitude of surface energy of atoms deposited on the substrate, and decide what kind of growth model it is. (5) With increasing time, the film becomes thicker and develops a structure, *e.g.* amorphous or crystalline, as well as epitaxial relationships. (6) At final step, the diffusion process occurs between film and substrate materials [35]. All of these steps are applicable to most thin film deposition techniques.

2.4.1 Growth of polycrystalline magnetite

Reactive Evaporation

The simplest way to grow polycrystalline thin films of magnetite is the evaporation and subsequent oxidation of metallic iron under an oxygen atmosphere. Furubayashi [36] grew polycrystalline magnetite onto substrates at room temperature by changing oxygen pressure during evaporation. He found that the deposited films contain different phases, such as α-Fe, FeO and Fe_3O_4. The optimal oxygen pressure to form single phase magnetite is $5x10^{-6}$ torr where the magnetoresistance (MR) ratio has a maximum value of around -5.5% in a magnetic field of 60 kOe. Experimental results from x-ray diffraction and Mössbauer spectroscopy reveal that both the formation of FeO inclusions in the lower oxygen pressure regime and the structure disorder in the higher oxygen pressure regime would lead to the decrease of MR ratio. In addition non-saturating behaviour has been observed at high magnetic field (~60 kOe), whereas 10 kOe is enough to reach saturation for the bulk Fe_3O_4. This non-saturating phenomenon is thought to be the result of the noncollinear spin structure on the

surface or grain boundaries.

Sputtering

Fe_3O_4 films were grown onto Si(100) substrates by using reactive rf sputtering [37]. The target was Fe, doped with a small amount of osmium (~0.75 at.%) in order to obtain higher coercivity of the samples. The x-ray diffraction data show that the lattice parameter of Fe_3O_4 grown at the substrate temperature of 230 ^oC is 0.8390 nm, which is slightly smaller than that of bulk materials (0.8396 nm), whereas the magnitude is noticeably increased to 0.8420 nm as the substrate temperature is reduced to below 125 ^oC. The magnetic moment of the film with a thickness of 100 nm is about 410 emu/cm^3 and is observed with a higher saturation field of 60 kOe. The increase of oxygen flow rate during deposition leads to a smaller average grain size and reduction of the magnetic moment, possibly resulting from transition from ferromagnetic to superparamagnetic. At low deposition temperature the saturation magnetization decreases owing to overpoluation of Fe^{3+} ions at A sites. Liu *et al.* [38, 39] used reactive sputtering to grow polycrystalline Fe_3O_4 from an Fe target under argon and oxygen ambience. The different thicknesses of Fe_3O_4 films obtained at room temperature were examined. XPS analyses indicated that there were only two absorption peaks at 709 eV (Fe $2p^{1/2}$) and 723 eV (Fe $2p^{3/2}$), meaning only a single phase of Fe_3O_4 is present. According to the XRD results, some peaks disappeared as the film thickness were reduced. This can be attributed to the reduction of grain size and change in texture. The electric resistivity is mainly dominated by grain boundaries in the film and can be described as a relation of $\log \rho \sim T^{-1/2}$, where ρ and T represent the resistivity and temperature, respectively. As a result, it implies that the tunnelling conductance acts across the interface of adjacent grains. They also observed that the saturation magnetization was diminished with decreasing film thickness. The magnetic measurements revealed that more anti-ferromagnetic interaction coupling at the grain boundaries occurs as the film thickness or grain size decreases. Moreover, the MR, for the films thicker than 200 nm, measured at room temperature was around -7.4% at 46 kOe and decreased to -1.1% for the 10 nm film. The origin of the MR decrease is due to surface spin-flip scattering and surface defects as the film thickness decreases.

Sol Gel

The Sol Gel method has been widely used to grow ceramic oxide materials because of its simplicity and cheapness. Chang *et al*. [40] prepared thin films of Fe_3O_4 onto quartz substrates *via* a sol-gel method, in which the sol consisted of iron salts and polydentate ligands. Xerogel films were prepared by coating thin layer of sols under vacuum drying at 40 ^oC for 1 hour, following by sintering to obtain the final product, Fe_3O_4. X-ray diffraction and thermo-gravimetric analysis (TGA) showed that the iron oxide film only contains Fe_3O_4, not γ-Fe_2O_3. The surface of the thin film of Fe_3O_4 was very uniform and the grain size was around 200~300 nm. Also, demagnetization behaviour was observed for thinner films (less than 120 nm) where the saturation magnetization decreased with increasing applied magnetic field. Additionally, the magnitude of the demagnetization increased with decreasing film thickness.

Electrodeposition

Like Sol Gel process, ferrite-plating is another soft solution process, which was described by Abe *et al.* in 1983 [41]. The principle of the ferrite-plating process is shown schematically and described in Figure 2.8. In the ferrite-plating process the solution is composed of ferrous (Fe^{2+}) and other metal ions (M^{n+}), if necessary. These metal ions are hydrolyzed to $FeOH^+$ and $MOH^{(n-1)+}$, respectively. When the substrate with OH^- groups is immersed into the solution, $FeOH^+$ and $MOH^{(n-1)+}$ can be adsorbed to form bonds on the surface. With an oxidizing-reagent such as $NaNO_2$, air or anodic current, some of Fe^{2+} ions are oxidized to Fe^{3+} ions. Consequently, the layer of ferrite without a preferred orientation is formed by means of successive absorption of iron oxyhydroxide on the substrate. The reaction can be expressed as below:

$$xFeOH^{2+} + yFeOH^+ + zMOH^{(n-1)+} + OH^- \rightarrow (Fe^{3+}, Fe^{2+}, M^{n+})_3O_4 + 4H^+ \qquad (x+y+z=3)$$

If the aqueous solution only contains Fe^{2+} ions, the reaction equation above can be written as:

$$3Fe^{2+} + 4H_2O \rightarrow Fe_3O_4 + 8H^+ + 2e^-$$

Since the new surface has OH^- groups, the deposition will continue as long as the metal ions and oxidizing reagent are present. This deposition process can be carried out at low temperature (< 100 ^oC) and there is no restriction on the substrate material.

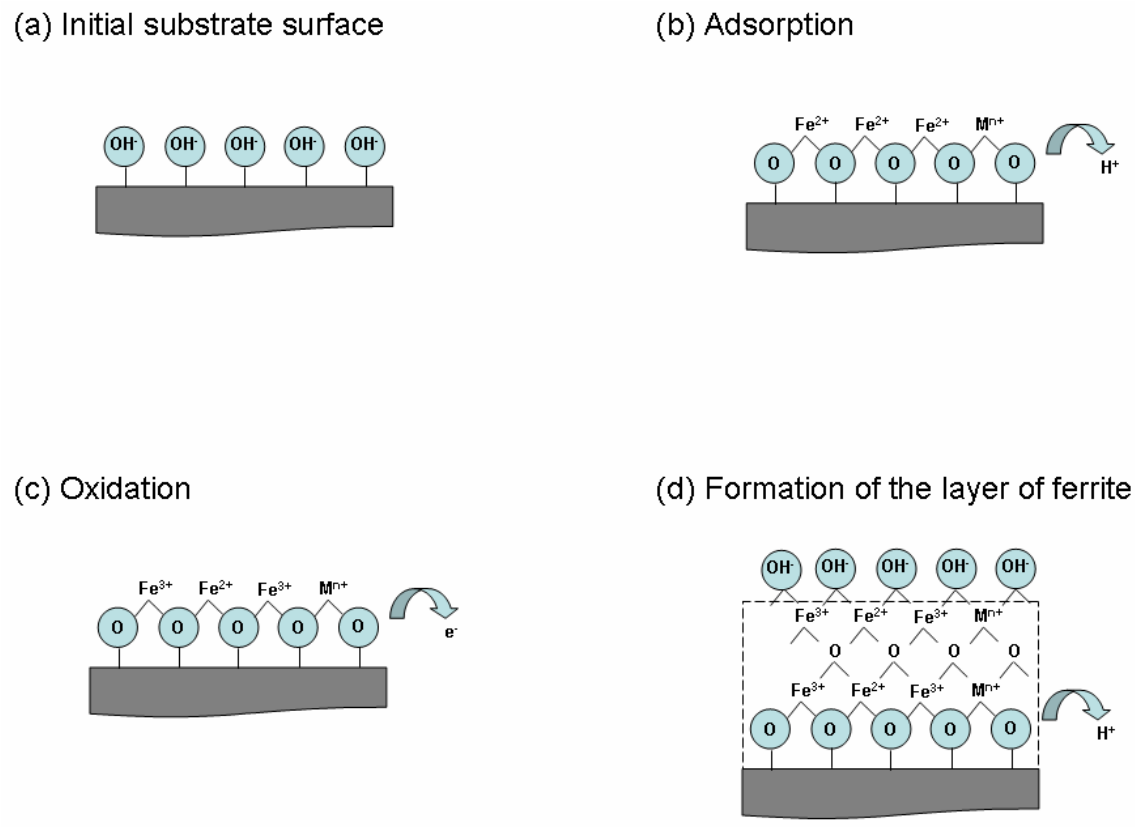


Figure 2.8: Schematic representation of the principle of ferrite-plating process [41].

The adhesion between deposited film and substrate material plays a key role in determining film quality. The substrate with O_2 or N_2 plasma treatment has OH^- and OOH^- groups on the surface to increase wettability. However, it is not suitable for metal such as stainless steel because OH^- or OOH^- group can not form on the metal surface [42]. A detailed study was carried out by Nishimura *et al.* [43], using the electro-ferrite plating technique to grow magnetite at 24-80 ^oC. The electrolyte was composed of $FeCl_2$ and NH_3 as pH adjuster. They observed that the deposition rate of Fe_3O_4 increased with increasing concentration of NH_3. This value reached a maximum before a decrease with further increasing concentration of NH_3. This reduction on deposition rate was due to the precipitation of $Fe(OH)_2$. In the other words, the Fe^{2+}/Fe_3O_4 equilibrium boundary at potential-pH equilibrium diagram [44] shifts to lower pH values at increasing temperature. Magnetic measurement showed

the electrodeposited Fe_3O_4 films have an identical value of saturation magnetization as the bulk material. In addition, the SEM micrographs revealed that the Fe_3O_4 film is the roughest and has the smallest thickness at lowest deposition rate.

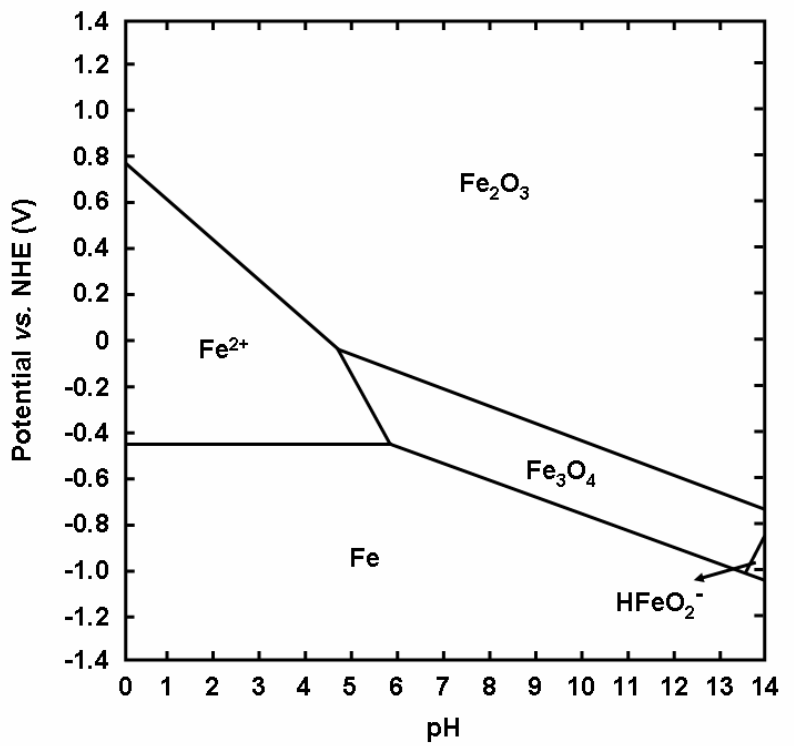


Figure 2.9: The potential-pH equilibrium of iron-water system at 25 ^oC [44].

Carlier *et al.* [45] has grown different forms of Fe_3O_4 including nanocrystalline film and nanocylinder on gold substrates *via* electrodeposition. The deposited films or cylinders showed neither preferred orientation nor magnetic anisotropy. Such results were consistent with that observed by Abe *et al.* [41]. For both types of nanostructures, coercive field and saturation magnetization increase with decreasing temperature, and higher saturation field (H_s = 10 kOe and 30 kOe for parallel and perpendicular field respectively) is observed in comparison with that of the bulk material (H_s = 360 Oe ~ 2 kOe). Furthermore, XRD results showed the lattice parameter of deposited films was slightly lower than that of bulk Fe_3O_4. This may be due to the strain or size effect in deposited films.

2.4.2 Growth of single crystalline magnetite

As mentioned previously, the polycrystalline thin films of Fe_3O_4 do not exhibit magnetic anisotropy. These films are therefore not suitable for high-performance spintronic devices in which a large magnetoresistance ratio is desired. Therefore, the growth of epitaxial single crystal Fe_3O_4 films becomes important. A particular area of concern is the formation of anti-phase boundaries due to small lattice mismatch between the deposited films and substrates [46]. It is an inevitable outcome during film preparation. The anomalous magnetic behaviour was observed in epitaxial single crystal Fe_3O_4 and was independent of film thickness and deposition techniques. It is a volume effect rather than surface influence [47, 48]. Antiphase boundaries present in the single crystalline Fe_3O_4 films can be annealed out by heating at an ultra-low oxygen environment, in which the antiphase domain coarsens with increasing time through a diffusive mechanism [49]. Several substrates whose lattice constants are close to that of Fe_3O_4 are chosen to grow epitaxial Fe_3O_4 films. Candidate substrates can be Au, Cu, MgO and NiO *etc*. All of them have a small lattice mismatch when depositing a layer of Fe_3O_4 onto it.

Iron Oxidation

Dependent on oxidation state of Fe, there are three common forms of iron oxides present during oxidation. These oxides: $Fe_{1-x}O$, α-Fe_2O_3 and Fe_3O_4, have distinct magnetic properties. Epitaxial $Fe_3O_4(111)$, using Fe oxidation onto single crystalline Cu(001) in an oxygen pressure of 10^{-6} mbar, was obtained by Kurtz *et al*. [50]. Two kinds of oxides, $Fe_{1-x}O$ and Fe_3O_4, were found in the oxidized film. For thin iron films below several monolayers the $Fe_{1-x}O$ formed during oxidation process. Fe_3O_4 only appeared as thicker Fe was deposited onto the copper substrate, where $Fe_3O_4(111)$ has a tensile mismatch of 0.7% and 0.32% on lateral. STM images revealed that strip-like iron oxides with a micron-long order are present on copper substrates and account for the large cohesive energy of the oxide lattice (11.6 eV per formula unit for spinel). The detailed growth mechanism was studied to oxidize iron films onto Pt(111) substrates [51]. The growth mechanism was described by the Stranski-Krastanov model. In each oxidation step, Fe_3O_4 nuclei increase in size by an Oswald ripening

mechanism where the surface energy among the nuclei is taken into account. Since the lateral growth rate of islands with $\{\bar{1}11\}$ and $\{2\bar{1}1\}$ planes on FeO(111) film is faster than the vertical one, smooth and flat Fe_3O_4(111) film can be obtained at the oxygen pressure of 10^{-6} mbar. By further increasing the oxygen pressure to 10^{-1} mbar, Fe_3O_4(111) were transformed into α-Fe_2O_3(0001) with a similar surface morphology. In addition, Mössbauer spectroscopy revealed that occupancy of tetrahedral (A) and octahedral (B) sites is identical as the values reported for the bulk material but the ratio of B_1:B_2 is higher (3:1 in bulk magnetite). Accordingly, the average magnetic moment is 2.8 ± 0.3 μ_B measured by polarized neutron reflectivity (PNR) for a thin Fe_3O_4 film of 53 ± 6 Å. This is probably due to finite film thickness, associated with a reduction of magnetic ordering temperature [52, 53].

Sputtering

Ultra-thin epitaxial Fe_3O_4 films (< 50 nm) grown onto MgO(100) using sputtering has successfully been demonstrated by Soeya *et al.* [54]. An Fe_3O_4 target was used to grow epitaxial films under an argon atmosphere. XRD measurements showed films grown under these conditions (≤ 573 K) contained small amount of antiferromagnetic α-Fe_2O_3, resulting from the partial oxidation of Fe_3O_4. The saturation magnetization at an applied magnetic field of 10 kOe is ~ 438 emu/cm^3. The relatively low saturation field is a result of exchange coupling between Fe_3O_4 and α-Fe_2O_3, which makes out-of-plane moments turn into in-plane ones. Additionally, saturation magnetization increases with increase deposition temperature. In order to reduce the geometrical effect, a low-resistive TiN (a = 0.424 nm) buffer layer formed onto MgO (a = 0.421 nm) substrate can be used to increase the MR ratio without changing the film structure [55]. Similar work was performed to grow epitaxial Fe_3O_4(111) film onto Cu/Si(001) substrates at room temperature [56]. The Verwey transition is about 121 K, indicating the stoichiometric Fe_3O_4 was obtained, and the saturation magnetization is 291 emu/cm^3 at a maximum applied magnetic field of 10 kOe. The TMR device with a sandwich structure composed of Fe_3O_4(111) and Al_2O_3 showed a low TMR value of < 10%. It is suggested that the selection of the interlayer barrier could be a key issue to fully exploit the half-metallic Fe_3O_4. The integrity of multilayered Fe_3O_4 devices was carried out by Takahashi *et al.* [57] from the Hitachi Corporation. The

current-perpendicular-to-plane giant magnetoresistive (CPP-GMR) device with Fe_3O_4 were fabricated on the Au(111) film deposited on MgO(001). With 20 nm thickness of Fe_3O_4, the MR ratio was 0.04%, which is four times larger than that of the NiFe-type CPP-GMR devices.

Laser Ablation

Laser ablation is another approach to produce epitaxial Fe_3O_4 thin films. The targets can be Fe, α-Fe_2O_3 or Fe_3O_4 depending on process condition such as substrate temperature as well as oxygen pressure. MgO is a common buffer layer grown onto substrates to obtain epitaxial Fe_3O_4. Kennedy *et al.* [58] deposited Fe_3O_4 thin films onto substrates with and without a MgO buffer layer by laser ablation of the Fe target under oxygen environment. The optimal growth condition of Fe_3O_4 was found at a substrate temperature of 450 ^oC and oxygen pressure of 10^{-4} Torr. Since the lattice parameter of Fe_3O_4 is 0.8396 nm, which is almost exactly twice of that of MgO, the growth can be epitaxial. However, the magnetic measurement revealed that the magnetization was diminished as a function of MgO layer thickness. Multilayered hetero-structures of $Fe_3O_4/SrTiO_3/La_{0.7}Sr_{0.3}MnO_3$ were grown on $LaAlO_3$(001) using pulsed laser deposition by using an α-Fe_2O_3 sintered target [59]. The oxygen pressure needed to be carefully adjusted due to the sharp phase boundary between α-Fe_2O_3 and Fe_3O_4. In this case the magnetic measurement showed MR ratios could be positive or negative depending on the measurement temperature. Above 200 K, a negative MR ratio was observed and resulted from the insulating reduction in $SrTiO_3$ with increasing temperature. Besides, no obvious relationship between MR and hysteresis behaviour was observed. This could be associated with the difference of spin-states in the two ferromagnetic bilayers. Detailed epitaxial growth of Fe_3O_4 *via* pulsed laser deposition has been studied by Sena *et al.* [60]. Fe_3O_4 thin films obtained from ablation of the bulk magnetite target contained a small amount of haematite. This was a consequence of the composition change of bulk target led by laser heating during the ablation process. The Verwey temperature of epitaxial Fe_3O_4 dropped off with decreasing thin film thickness. This can be attributed to the interfacial strain in the epitaxial films where the lattice distortion affects the epitaxial growth, especially in thinner films.

Molecular Beam Epitaxy

Recently molecular beam epitaxy (MBE) has become the most common way to grow epitaxial Fe_3O_4 thin films because of its already wide-spread use in the semiconductor industry. As mentioned above, a buffer layer is necessary to grow epitaxial thin films. However, the inter-diffusion of cations always takes place under a high processing temperature (> 350 ^oC). Some studies have revealed that substantial Mg segregation occurs when MgO is used as a buffer layer to carry out epitaxial growth during post-deposition process. The close lattice parameters between epitaxial Fe_3O_4 thin films and substrate materials MgO could be the reason to induce inter-diffusion [61]. Accordingly, the onset of Mg segregation to form on the surface is about 670 K. Similar consequences have been found in cubic monoxides such NiO and CaO. A tri-layer film (Fe_3O_4/NiO/Fe_3O_4) has been proposed to study the degree of inter-diffusion by Shaw *et al.* [62]. Experimental results showed that NiO thin films can substantially reduce the inter-diffusion between ferromagnetic Fe_3O_4 layers, even less than 10 nm. Stoichiometric and non-stoichiometric $Fe_3O_4(111)$ thin films grown on $Al_2O_3(0001)$ substrates from a Knudsen cell were studied by the synchrotron technique, x-ray magnetic circular dichroism (XMCD) [63]. Theoretical absorptions for different site occupancies of Fe were calculated (Figure 2.10a). The sum of these corresponding contributions induces a resulting spectrum of Fe_3O_4, where the ratio of $Fe_{Oh}^{2+} : Fe_{Td}^{3+} : Fe_{Oh}^{3+}$ is 1:1:1. Practically, two kinds of iron oxide films, $Fe_{3-\delta}O_4$ and Fe_3O_4, showed somewhat different absorption spectrum and XMCD signals. Compared with the theoretical calculation, non-stoichiometric iron oxides showed a relative reduction in Fe^{2+}, meaning that a net transfer of Fe^{3+} ions from tetrahedral to octahedral sites. For stoichiometric and non-stoichiometric iron oxides film the low MR values about 1% at room temperature were observed. The MR behaviour in the single crystalline Fe_3O_4 films can be attributed to presence of antiphase boundaries. Moreover, the films after post-annealing treatment at 900 K were found to remain the same MR ratio as the domain size is expected to be increased.

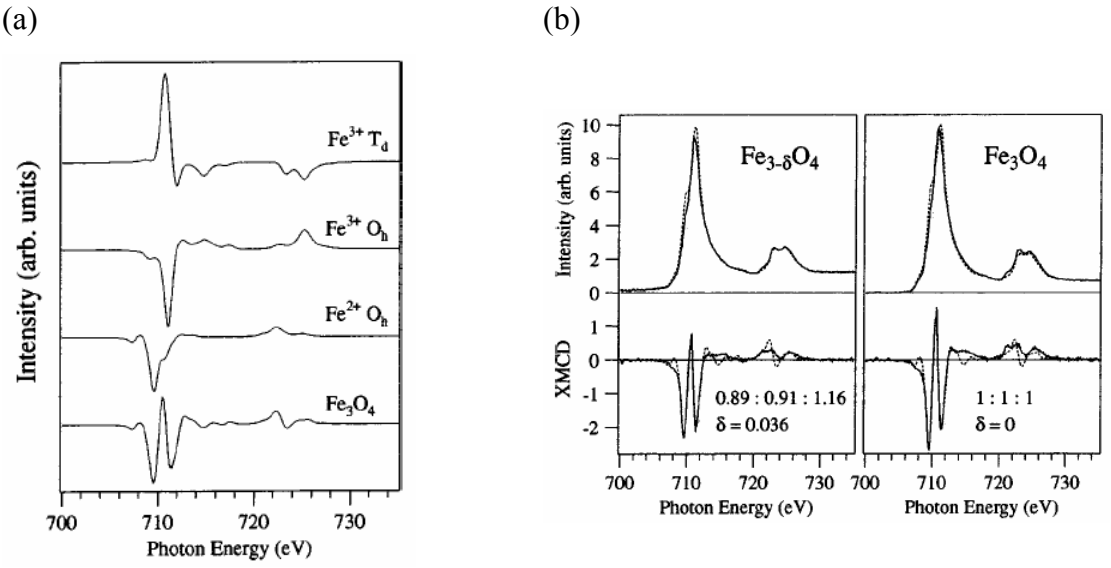


Figure 2.10: (a) The theoretical absorption for different Fe sites in the Fe_3O_4 lattice. (b) XAS and XMCD signals for two different iron oxide films [63].

Electrodeposition

In comparison with deposition techniques such as iron oxidation and MBE, epitaxial Fe_3O_4 growth *via* electrodeposition can be carried out at relatively lower temperature below 90 ^oC. Currently, only a few articles have been published to discuss epitaxial Fe_3O_4 growth, though the films preparation is based on the principle on Abe's ferrite plating as described previously.

The first work to grow epitaxial Fe_3O_4 thin films was carried out by Switzer's group. Nikiforov *et al.* [64] has grown epitaxial magnetite films on single crystal Au(111) substrates. Since gold has a lattice parameter a = 0.40786 nm, the epitaxial magnetite can grow on it with a small lattice mismatch of about 3%. In this work the electrolyte was composed of $(NH_4)_2Fe(SO_4)_2 \cdot 6H_2O$ as a source of cations and CH_3COOK as a pH buffer solution. The epitaxial Fe_3O_4 thin films were grown either by applying a constant potential (-0.45 to -0.3 V *vs.* Ag/AgCl) or a constant current (0.05 $mA \cdot cm^{-2}$), and exhibited the identical crystallographic direction with substrates both on out-of-plane and in-plane orientations. The other low-index gold substrates used to grow epitaxial magnetite films were performed by Sorenson *et al.* [65]. They found that epitaxial Fe_3O_4 films with [110] direction grew onto Au(110) substrates, whereas

thin films with three different orientations, [100], [111] and [511] were observed on Au(100) substrates. The spin polarization of epitaxial Fe_3O_4(111) is -40% at room temperature without any surface treatment.

Table 2.2 below provides a summary of the various deposition techniques that have been used and the characteristics of the magnetite films prepared.

Deposition method	*Source*	*Substrate*	*Growth temperature (^oC)*	*Crystal structure*	*Saturation field, H_s (kOe)*	*Saturation magnetization, M_s (emu/cm^3)*	*MR ratio (%)*	*Reference*
Reactive evaporation	Fe	Glass, Kapton	R.T.	P	> 60	~ 298	-5.4	[36]
Sputtering	Fe	Si(100)	230	P	> 60	410	-	[37]
	Fe	Glass, Kapton	R.T.	P	> 50	280	-7.4	[38, 39]
	Fe_3O_4	MgO(100)	300	S	10	~ 438	-	[54]
	FeO_x (x=0.75)	TiN(110)	300	S			> 10	[55]
	Fe	Cu(001)	R.T.	S	-	291	-	[56]
	Fe_3O_4	Au(111)	250	S	-	~ 400	-0.04	[57]
Sol gel	iron(II) lactate + iron(III) nitrate)	quartz	450	P	> 10	135	-	[40]
Electrodeposition	$FeCl_2$	Cu, PET, Stainless steel	40~80	P	-	-	-	[41]
	$FeCl_2$	ITO	24~80	P	-	480	-	[43]
	$(NH_4)_2Fe(SO_4)_2 \cdot 6H_2O$	Au	80	P	~ 10	-	-	[45]
	$(NH_4)_2Fe(SO_4)_2 \cdot 6H_2O$	Au(100), (110), (111)	90	S	-	-	-	[64, 65]
Iron Oxidation	Fe	Cu(001)	562	S	-	-	-	[50]
	Fe	Pt(111)	597	S	-	-	-	[51]
	Fe	Pt(111)	567	S	-	~ 320		[52, 53]
Laser ablation	Fe	Si(100), GaAs(100)	450	S	14	650~800	-	[58]
	α-Fe_2O_3	$LaAlO_3$(001)	570	S	-	-	~ -7	[59]
	Fe, Fe_3O_4	MgO(100), Al_2O_3(0001)	-	S	-	-	-	[60]
Molecular beam epitaxy	Fe	MgO(001	297	S	-	-	-	[61]
	Fe	MgO(100)	300	S	55	465	-	[62]
	Fe	Al_2O_3(0001)	627	S	-	-	~ -1	[63]

(R.T.: room temperature; P: polycrystalline; S; single crystalline)

Table 2.2: Comparison of morphology and magnetic properties for Fe_3O_4 prepared at different deposition techniques.

2.5 Growth mechanism by electrodeposition

Electrode Kinetics

Electrochemistry is the study and application of the phenomenon of the transfer of electric charges between two phases, *i.e.* a metal and a solution with ions. In an electrochemical cell, if particles in the electrolyte accept electrons from the electrode; this is called reduction, whereas if particles donate electrons to the electrode; this is called oxidation. Consequently, a potential difference is built up across the interphase (Figure 2.11).

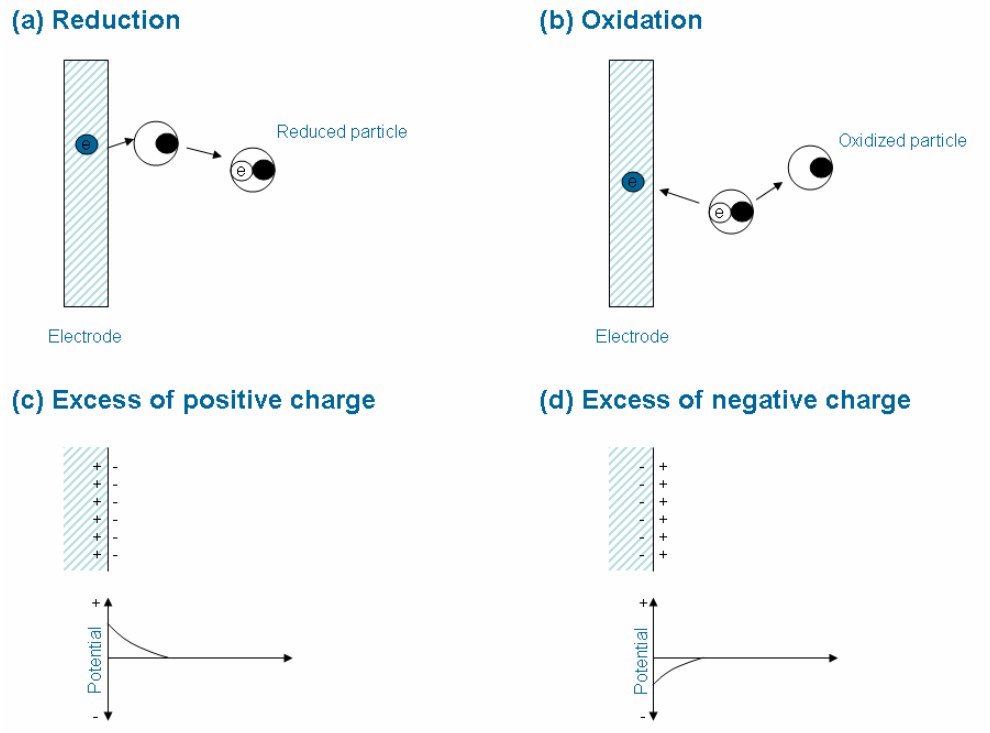


Figure 2.11: Schematic representation of charge transfer (a-b) and resulting potential difference (c-d) in an electrochemical reaction [66].

When two phases are brought into contact, there is a double layer at the interface, in which one is the charges on the electrode surface; the other is the layer of charges in electrolyte. The magnitude of the layer can be given by the Debye length as below.

$$\lambda = \left(\frac{\varepsilon RT}{F^2 \sum_i z_i^2 c_{i\infty}} \right)^{1/2}$$

where λ is the Debye length; ε is the permittivity, F/cm; R is the universal gas constant, 8.314 J/mol·K; T is the absolute temperature, K; F is the Faraday constant, equal to 96500 C; z_i is the charge number of species i; $c_{i\infty}$ is the average concentration of species i. Typically, the Debye length is the order of 1 nm [67]. Consequently, the electric field strength is extremely high even for a small potential difference within the double layer.

Transport of ions in the electrolyte can be mainly divided into three mechanisms. First of all, the diffusion process in which the driving force is the concentration gradient because the electrode receives or give up electrons to charged ions from the electrolyte. The diffusion rate can be expressed by the equation:

$$i_{diff} = -DF(\frac{dc}{dx})$$

where i_{diff} is the diffusion rate of ions to the electrode with a unit of C m^{-2} s^{-1}. D is the diffusion coefficient; dc/dx is the concentration gradient between the electrode and electrolyte.

The value of dc/dx would increase with increasing the current density. However, there is a limiting maximum value. To simplify the diffusion process the concentration gradient can be described as a linear relationship, and diffusion occurs across a Nernst diffusion layer with a thickness of δ. Having made these presumptions, the maximum value would happen at $c_{electrode}$= 0. It can be expressed by the equation below.

$$\frac{dc}{dx} = \frac{c_{bulk} - c_{electrode}}{\delta} = \frac{c_{bulk}}{\delta}$$

where c_{bulk} and $c_{electrode}$ represent concentrations at bulk solution and electrode surface, respectively. Thus, the limiting current (i_L) with the highest value existing in the

electrolyte can be estimated.

The electric field is another transport mode of ions. As the electric field is present in the solution, it can accelerate the movement of ions including cations and anions to electrodes. Finally, one must consider convection. There are two kinds of convection: force convection and natural convection. The force convection happens as stirring in a solution to move ions towards the electrode surface, whereas, the nature convection is due to the depletion of ions near the electrode surface during the electrochemical reaction.

The kinetics of electronic charge transfer for the electrochemical situation has been thoroughly reviewed by Bockris *et al*. [66]. In classical mechanics the occupied probability of electrons in a metal can be expressed by the Fermi-Dirac distribution function.

$$F(E) = \frac{1}{\exp[(E - E_F)/kT] + 1}$$

where *F(E)* is the probability; E_F is the Fermi energy; E is the energy level in a material; k is the Boltzmann constant and T is the absolute temperature.

Based on the equation shown above, the calculated current density for the electrochemical case is infinitesimal ($< 10^{-16}$ A·m^{-2}). However, in reality the value is the order of 10 A·m^{-2}. Accordingly, the classical mechanics is not suitable to describe the transfer of electrons from a metal in solution to neighbouring ions and *vice versa* because an electron with a smaller energy than Fermi energy can not escape from a metal surface. However, quantum-mechanical tunnelling can elucidate the transfer of electrons through an energy barrier. It describes the particles or electrons by a wave-function. Figure 2.12 is the picture showing the quantum-mechanical tunnelling of an electron in a vacuum and a metal-electrolyte interface. In quantum mechanics an electron ($x < 0$) travelling in a vacuum with an energy smaller than Fermi energy (E_F) still has some possibility to tunnel to other side ($x > L$) of a material. In the case of the electrochemical situation, an electron should have energy at E_F. At an energy level below the E_F, there is no empty state. In other words, electrons with energy level

below E_F have no mobility to react with a given species in the electrolyte. The tunnelling occurs only if an electron is available, meaning its energy level is around E_F. Additionally, there is no energy change during the process of electron transfer.

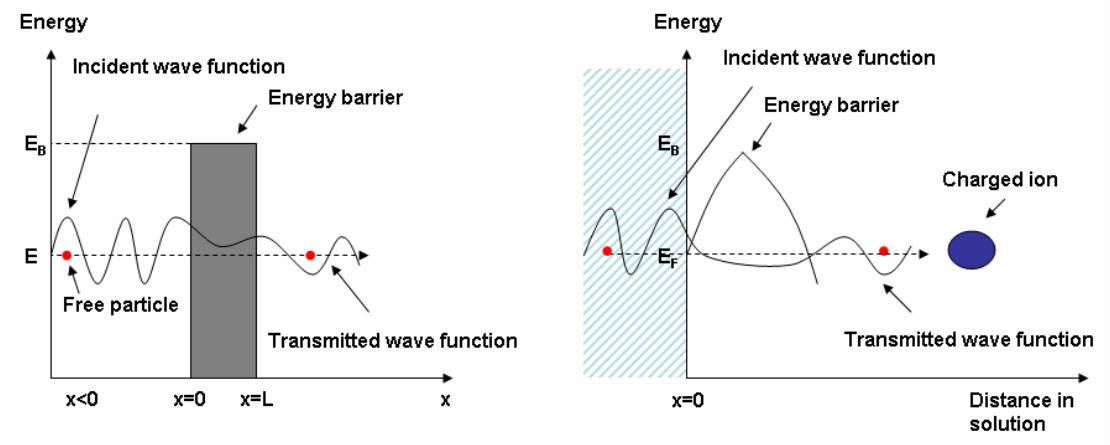


Figure 2.12: Illustration of the quantum-mechanical tunnelling of a free electron through an energy barrier. (a) in vacuum; (b) in metal-electrolyte interface. (The red and blue dots denote a free electron and charged ions, respectively.) [66]

Theory of Electrodeposition

Though the mechanism of ferrite plating has been proposed by Abe *et al.* [41] in 1983, it is worth further developing an understanding of the kinetics of film growth *via* electrochemical deposition. Mehl *et al.* [68] studied the growth of silver using galvanostatic experiments. They showed that the growth rate was controlled by surface diffusion of adions in the low current regime, whereas the transfer of ions became rate-determining at high current regime.

A detailed description of the surface diffusion where ions adsorbed onto the surface of electrode initially and gradually moved with the concentration gradient was carried out by Despic *et al.* [69]. In their study an infinitesimal area of the electrode surface was considered as shown in Figure 2.13. The relationship between the current density and adion concentration in the x-direction can be expressed as below.

$$\left({i_{a,x}}/{zF}\, dxdy \right) = \left({i_{c,x}}/{zF} \right) dxdy + D\left({\partial^2 c_{ad,x}}/{\partial x^2} \right) dxdy$$

where $i_{a,x}$ and $i_{c,x}$ are anodic and cathodic current density, respectively and $C_{ad,x}$ is adion concentration. Solution to the equation can be found by introducing boundary conditions (see Appendix A-2), it can be rewritten as

$$y = \left[(1+\beta) zF \Big/ 4.6RT \right] \eta_a + \log \frac{1+\exp\left[-2(i_0 / zFv_0)^{1/2} p \right]}{1-\exp\left[-2(i_0 / zFv_0)^{1/2} p \right]} - \frac{1}{2} \log(i_0 zFv_0)$$

where

$$y = \exp\left\{ \left[\left(zF \Big/ RT \right) \eta_a \right] - 1 \Big/ i \right\}$$

The similar relation can be obtained for the cathodic case. As the current density is very small, the equation shown above can be reduced and identical with the Butler-Volmer equation. In this case, the current densities are equivalent everywhere on the electrode surface.

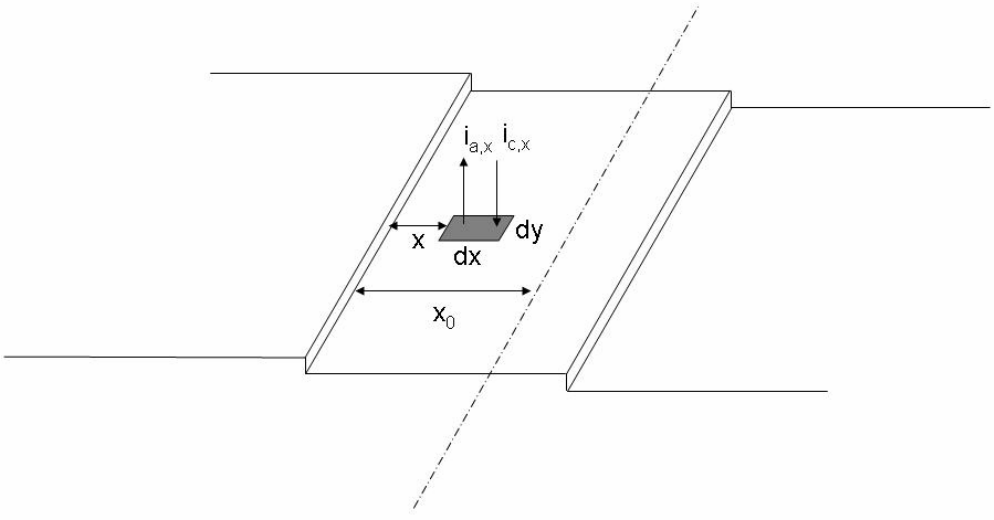


Figure 2.13: Schematic representation of the electrode surface during the deposition process [68].

Influence of Overpotential

The overpotential has been found to affect the crystallographic orientation of films grown onto both polycrystalline and single crystal substrates using electrodeposition.

In the case of f.c.c metal deposited onto polycrystalline substrates, the experimental results showed the changes in crystallographic directions from <111>, <100>, <110>,<113> to <210> subsequently with increasing overpotential [70]. Switzer *et al*. [71] observed the electrodeposited epitaxial films experienced a thermodynamic to kinetic transition with increasing electrode overpotential. Films grown with a small overpotential can be treated as thermodynamic. However, the growth becomes predominately by kinetic mechanism after a critical thickness is reached. The growth transient is affected by the pH value of electrolyte and can be found from the current-time plot experimentally.

3. Experimental

3.1 Substrate preparation

Copper foils

Polycrystalline copper substrates with a purity of 99.995% and 0.125 mm in thickness were purchased from Advent Research Materials Ltd (Oxford, UK). The copper substrates were mechanically polished at 3, 1 and 0.25 μm successively. After polishing, all substrates were ultrasonically cleaned in acetone and subsequently rinsed with deionised water.

Nickel tapes

Single-phase rolling-assisted biaxially textured substrates (RABiTS) of single phase Ni{100}<001> 100 μm in thickness were crystallised for 1 hour at 900 ºC. The cleaning procedure of the nickel substrates was summarized in Table 3.1 below.

Step	Description
1	Clean residual particles and degrease with acetone
2	Dip in 5% HF for 60~90 s to remove native oxide
3	Rinse with de-ionized water and blow dry in N_2

Table 3.1: The cleaning procedure for Ni substrates.

Cu (50 nm)/Si (001) substrates

Si(001) substrates were cleaned by a standard RCA (Radio Corporation of America) clean procedure (Table 3.2) [72]. After finishing, a thin layer of copper (purity: > 99.999%) about 50 nm thick was deposited onto the silicon substrate using a sputtering technique.

Step	Bath composition	Purpose
1	H_2O: H_2O_2: NH_4OH (5:1:1) at 80 ºC	Removal of organic contamination
2	H_2O: HF (50:1)	Removal of native oxide
3	H_2O: H_2O_2:HCl (6:1:1) at 80 ºC	Removal of ions and heavy metal

Table 3.2: The standard RCA clean procedure [72].

Au (50 nm)/Glass substrates

Glass substrates were cleaned sequentially with OptiClear detergent (National Diagnostics), acetone, methanol, and deionised water. In each cleaning step, the glass substrates were placed in an ultrasonic bath for 15 minutes. When the cleaning procedure was completed, the substrates were blow-dried with clean nitrogen. A 50 nm layer of gold thin was vaporized onto glass substrates. Prior to electrodeposition, the Au/glass substrates were dipped in 5 % HF solution to remove native oxide.

3.2 Electrochemical apparatus setup

The growth of iron oxide thin films employed a conventional three-electrode cell apparatus depicted in Figure 3.1 under either galvanostatic or potentiostatic operation. Two kinds of potentiostats were used in this study: EG&G Princeton Applied Research model 263A (Oak Ridge, Tennessee USA) and ACM GillAC potentiostat (Cumbria, U.K.), linked to a computer for both software-based potentiostat control and data recording. A lid was placed to cover the Pyrex beaker to avoid evaporation of electrolyte during the processes of argon purging and deposition. The bath temperature was controlled by a hot plate equipped with magnetic stirrer.

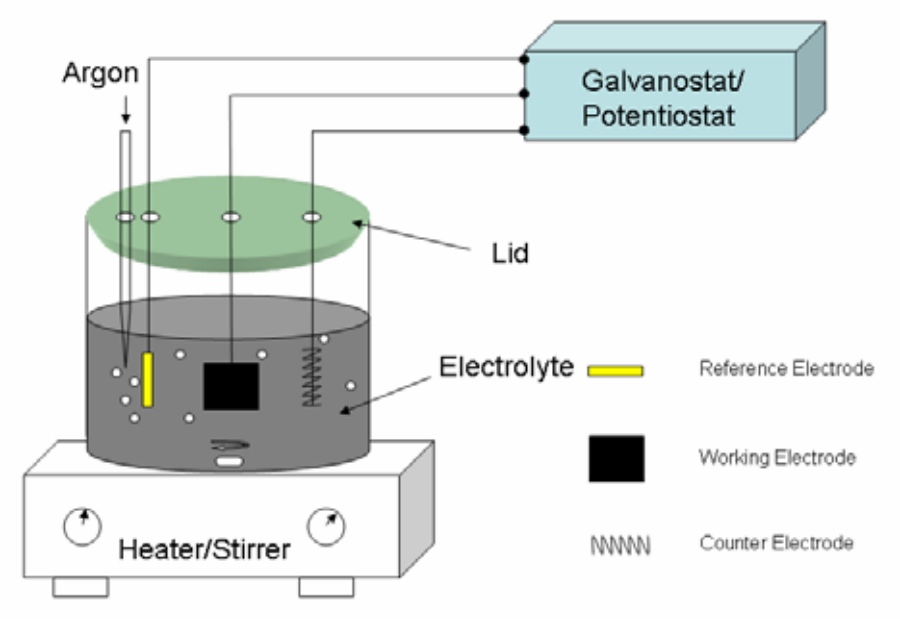


Figure 3.1: Schematic representation of a three-electrode cell apparatus.

Different experimental parameters have been used to study electrodeposited Fe-oxide thin films. Table 3.3 shows the details of parameters and their corresponding sections in this document.

Parameters	Description	No. of Section
Temperature (*T*)	60 ^{o}C; 75 ^{o}C; 90 ^{o}C	4.1
Current density (*i*)	0.005 mA·cm^{-2};0.05 mA·cm^{-2}; 0.5 mA·cm^{-2}	4.1
Potential (*E*)	10~400 mV (for Cu/Si substrates) -5~400 mV (for Cu foils)	4.4
Buffer concentration	Concentration of CH_3COOK: 0.05M~0.5M	4.5
Substrate	Cu NiO/Ni Cu/Si Au/Glass	4.1; 4.4 4.3 4.3 4.2; 4.5

Table 3.3: Deposition parameters investigated in this present work.

3.3 Characterization techniques

3.3.1 Atomic force microscope

The atomic force microscope (AFM) is a useful tool to examine surface topography with nearly atomic resolution. The first AFM was designed and built by Binning and his coworkers in 1986 [73]. The instrumental principle of AFM is very similar to that of the scanning tunnelling microscope (STM), which is to measure the interaction between scanning probe and sample surface. (Figure 3.2) In AFM the forces are measured as approached to local currents in STM. In the operation of AFM, the sharp probe glued or attached on to a cantilever is brought to the sample surface at some distance, and interaction force can be measured along x and y directions from the cantilever deflections according to Hook's law, $\Delta z = \Delta F/c$, where Δz is the deflection, ΔF is the acting force and c is the spring constant. The magnitude of the interaction force is dependent upon distance. (Figure 3.3) At a distance of ~ nm, the dominant force is the repulsive van der Waals interaction, which is strong enough to move a cantilever in an AFM while over long-range interactions (~ 10 to 50 nm) that prevailed are electric or magnetic forces [74]. The signals of the cantilever deflections are received by position-sensitive detector (PSD), usually a four-segment photo-diode, where the small displacement of the cantilever can be amplified to 300 to 1000 times and easily measured even if as small as 0.01 nm, then converted into electric current through a feedback-loop system. Thus, surface topography can be recorded. Due to the small interaction force (10^{-6} ~10^{-10} N), cantilever deflections less than 0.1 nm can be precisely measured as the spring constant of commercial cantilevers is in the range of 10^{-2}~10^{2} N·m^{-1}. Alternatively, the vibrational characteristics of the cantilever can substitute for deflection response which has a small signal-to-noise ratio. The measured resonant frequency is dependent on the dimensions and the material properties of the cantilever. The topographic image can be based on the frequency or the phase of oscillation.

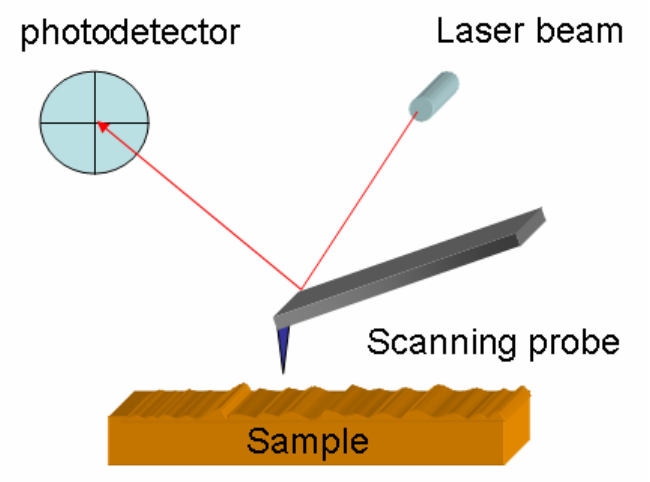


Figure 3.2: Description of instrumental principle of an AFM.

There are three main types of scanning modes in the AFM operation: contact mode, non-contact mode and tapping mode. In the contact mode operation, the scanning probe is touching the sample surface. It is applicable to samples with harder surfaces. In the non contact mode of operation, there is some distance between the scanning probe and the sample surface, usually several nm. The signals of cantilever deflections come from a high-frequency (100 kHz to 1MHz) oscillator attached with the scanning probe. Tapping mode is the method between contact and non contact modes of operation. In the tapping mode operation the scanning probe vibrates at a high frequency in the z direction and only touches the sample surface at each vibration period. The resolution is almost no different to that of contact mode operation, but possible sample damage is minimized.

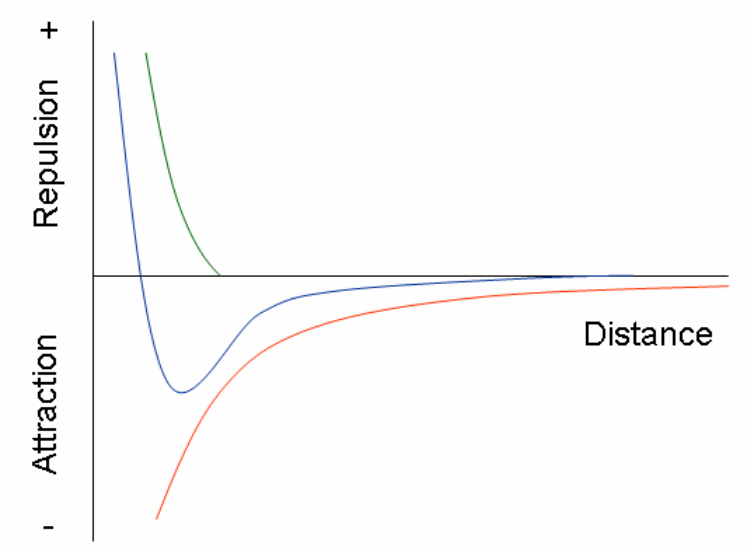


Figure 3.3: Force curve. (green, red and blue solid lines represent repulsion force, attraction force and balanced force respectively)

The AFM used in this study is a Molecular Imaging PicoSPM as shown in Figure 3.4. It mainly consists of a scanner head, four-segment photo-detector, sample holder and motor actuator. The scanner head is top-down design allowing easy access to the sample surface.



Figure 3.4: Schematic representation of a Molecular Imaging PicoSPM.

3.3.2 Scanning electron microscope

The scanning electron microscope (SEM) is mainly used to examine the surface morphology of a substance. The original idea was come out by Zworykin *et al.* [75]

and became first commercial instrument in 1965. The principle of SEM can be schematically described in Figure 3.5. The electron gun produces a beam of electrons which are accelerated to a high energy state about 0.2~40 eV. Accelerating electrons pass through electron lenses to reduce the diameter of electron beam, and then are incident on the specimen.

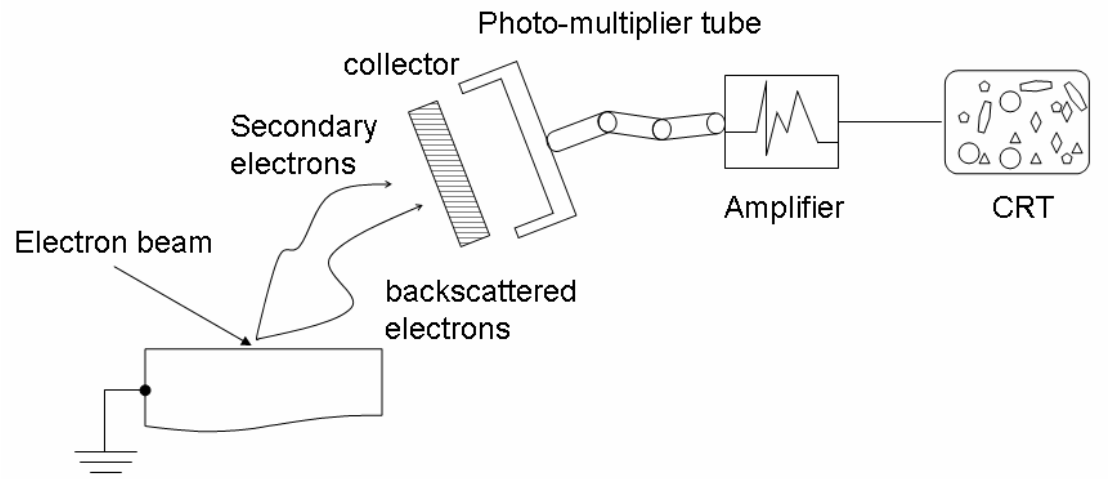


Figure 3.5: Schematic representation of a SEM instrumental principle.

Due to the interaction of focused electron beam with the specimen, various kinds of signals will be generated *via* different mechanisms as shown in Figure 3.6. Of these signals are secondary electron (inelastic scattering) and backscattered electron (elastic scattering). These two signals can be collected by an electron detector to produce images.

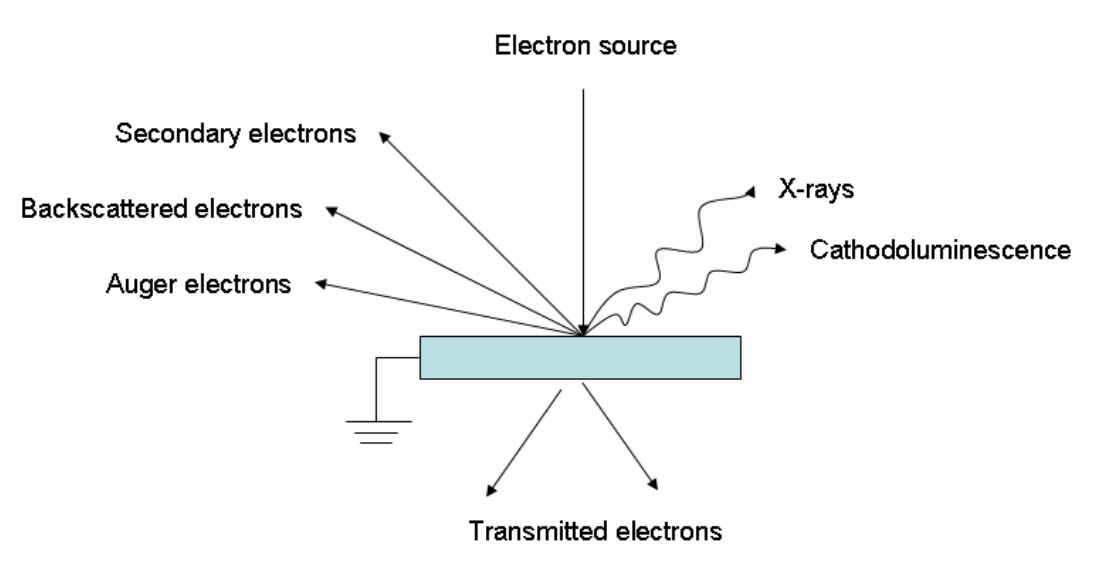


Figure 3.6: Different signal sources when a beam of electrons bombard sample surface.

Traditionally, the electron source is produced through thermal emission of the cathode material in an electron gun. However, this type of electron source has low brightness, evaporation of the cathode material and thermal drift during operation. Alternatively, field emission is another way to produce electrons without these disadvantages, where the electrons can tunnel through energy barrier without thermal assistance to overcome the work function of cathode material [76].

The SEM can be equipped with an energy-dispersive x-ray spectrometer (EDX), which uses a solid-state x-ray detector, usually Si(Li) with a dimension of a few millimetres thick and a ~centimetre in diameter, to collect x-ray photons excited from the specimen [77]. Compared with a wavelength dispersive spectrometer (WDS), it has advantages of faster analysis speed, higher received signals and wide scan range. In X-ray microanalysis, each x-ray photon causes the ejection of a photoelectron and creates an electron-hole pair in the solid-state detector. Consequently, the charge pulse is produced and converted by charge-voltage converter. The number of electron-hole pair ($N_{e\text{-}h}$) is given by

$$N_{e-h} = E_{total} / 3.81$$

where E_{total} is the x-ray energy and the average energy for the formation of

electron-hole pair is 3.81 eV in Si(Li) detector (~3 eV for Ge(Li) detector). This will allow us to do qualitative or quantitative chemical analysis. In order to avoid lithium diffusion, liquid nitrogen is used to keep the detector at low temperature.

3.3.3 X-ray diffraction

X-ray diffraction (XRD) is a non-destructive technique that reveals the crystallography of an unknown material using monochromatic x-rays. (Figure 3.7) In a typical laboratory system the x-rays are produced by a Cu source. A beam of accelerating electrons from a hot cathode bombards a metal target and ejects an inner shell (1*s*) electron out. In the meantime, an electron from the outer shell (2*p* or 3*p*) immediately drops down to occupy the vacant position (1*s*) and produces the characteristic x-ray. For a copper target, x-ray emissions commonly contains a continuous white radiation and two characteristic x-rays, K_α (λ = 0.15418 nm) and K_β (λ = 0.13922 nm) leading from $2p \rightarrow 1s$ and $3p \rightarrow 1s$ transitions, respectively. In reality, the K_α transition occurs more intense and frequently than K_β, and is a doublet which consists of $K_{\alpha 1}$ and $K_{\alpha 2}$. This is because of the slight difference between two possible spin electron states of 2*p* electrons. In order to obtain monochromatic K_α x-rays for the diffraction experiment, the suitable filter can be used to absorb unneeded white radiation and K_β. For instance, a nickel foil is commonly used for radiation of a copper target [78].

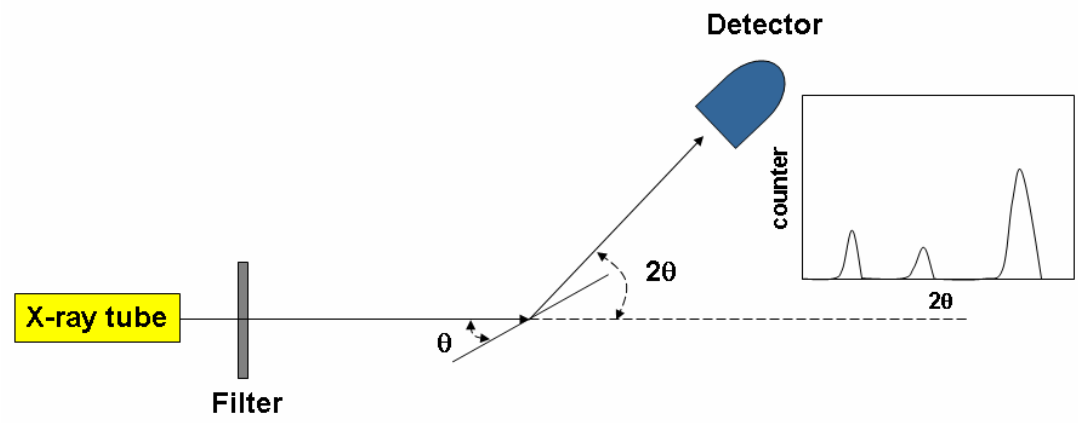


Figure 3.7: Principle of x-ray diffraction.

X-ray diffractions works on the principle described by Bragg's law, $n\lambda = 2d \sin\theta$, where λ is the x-ray wavelength, d is the lattice spacing and θ is the Bragg angle. As described in Figure 3.8, the x-ray beams (1 and 2) are incident on adjacent lattice planes (A and B) and diffracted beams (1́ and 2́) are reflected. The only condition to make these two reflected beams in-phase is that, extra travel distance of incident beam 2 should be equal to a whole number of wavelengths. In a real circumstance, a crystal contains thousands of planes. Reflected beams can become constructive only if they satisfy Bragg's law.

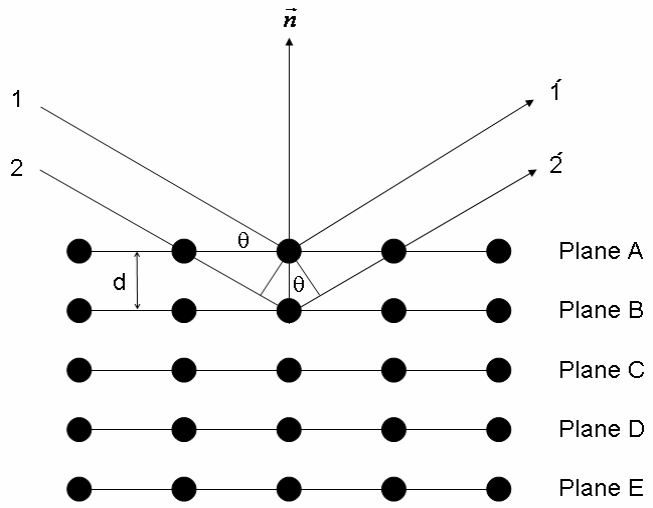


Figure 3.8: Schematic representation of Bragg's law.

An X-ray diffractometer with a Bragg-Brentano geometrical design (Figure 3.9) was used to examine the phase of iron oxides in this work. It is a common design because of its simplicity and efficiency. Nevertheless, in this design a beam of x-rays is not parallel coming into the specimen, resulting in the peak broadening in the XRD spectrum. For precious phase identification including the estimation of lattice constant and particle size, these will be done by employing synchrotron x-ray diffraction technique.

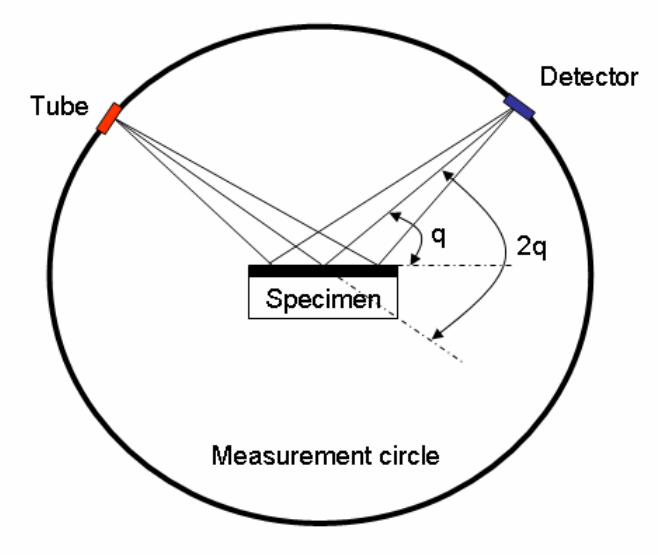


Figure 3.9: Bragg-Brentano geometry in X-ray Diffraction.

3.3.4 Transmission electron microscope

In this work the transmission electron microscope (TEM) was used for high resolution lattice imaging. A beam of electrons is transmitted through a very thin specimen (~ 100 nm) and produces either an image or a diffraction pattern dependent on the signal taken. Figure 3.10 illustrates the main components for a typical TEM instrument. The gun provides a source of electrons, and usually can be fall into two categories: thermionic emission or field emission. Tungsten and lanthanum hexaboride (LaB_6) are two common materials used for thermionic emission because of their higher melting temperature and low work function, respectively.

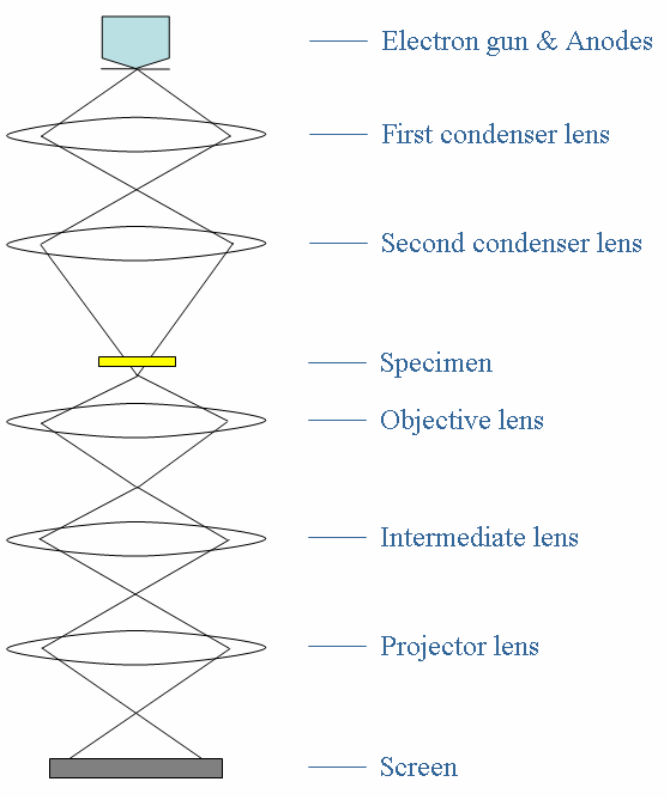


Figure 3.10: Schematic illustration of components in a typical TEM.

The physical behaviour of thermonic emission can be described by Richardson's Law shown below.

$$J = AT^2 e^{-\frac{\Phi}{kT}}$$

where J is the emitted current density; A is the Richardson's constant (unit: $A/m^2\ K^2$); T is the absolute temperature; Φ is the work function and k is the Boltzmann's constant (8.6×10^{-5} eV/K). In contrast, the mechanism of field emission is much simpler. The calculated electric field (E) is equal to V/r, meaning that electric field increases considerably as a certain voltage (V) is applied to a point of radius (r). To get field emission to work two anodes are needed. In field-emission guns (FEG's) electrons emitted from a sharp tip are extracted by the first anode positively charged by several kV with respect to the tip, followed by second anode accelerating the electrons to 100 kV or more.

Magnetic electron lenses are commonly used in TEMs because they are not affected

by high voltage breakdown. There are several kinds of magnetic lenses in the TEM: condenser lens, objective lens, intermediate lens and projector lens. Each lens plays a different role. Condenser lenses are utilized to illuminate the specimen with a parallel electron beam. The beam size is typically about a few tens of micrometers, usually smaller in the case of field-emission-gun source. In the process of illumination, the first condenser lens generates a demagnified image of the gun crossover. The second condenser lens controls the convergent angle of a beam leaving the condenser system, and then produces a focused parallel beam on the specimen.

The objective lens is the most important part of the TEMs. It is usually a strong lens, and generates the images and diffraction patterns as a beam of electron are scattered by the specimen. Either images or diffraction can be magnified by intermediate or projector lenses prior to developing on the viewing screen.

The resolution in TEMs can be described by the Rayleigh criterion shown below.

$$\delta = \frac{0.61\lambda}{n \sin \beta}$$

where δ is the minimum resolved distance; λ is the wavelength corresponding to the electron beam energy; n is the refractive index and β is the maximum aperture collection angle. According to equation above, the higher the accelerating voltage (E) of the microscope, the smaller resolved distance it is as λ is roughly equal to $1.22/E^{1/2}$. However, the theoretical value is not normally reached in TEMs due to lens aberration such as spherical aberration, chromatic aberration and astigmatism [79].

3.3.5 Vibrating sample mangetometer

The vibrating sample magnetometer (VSM) was originally developed by Foner [80]. It is suitable for use in low temperature and higher magnetic field studies. The working principle of VSM is based on the Faraday's law of induction in which an *e.m.f.* (electromotive force) is induced by a time-varying magnetic flux (Figure 3.11). When a magnetic sample is vibrated sinusoidally with a small fixed amplitude (A) in a

magnetic field, the induced voltage (E) can be given by [81]

$$E=\sigma GA2\pi f \cos(2\pi f t)$$

where σ is the magnetic moment of the sample, G is a factor dependent upon the detection coil geometry, f is the vibration frequency and t is time.

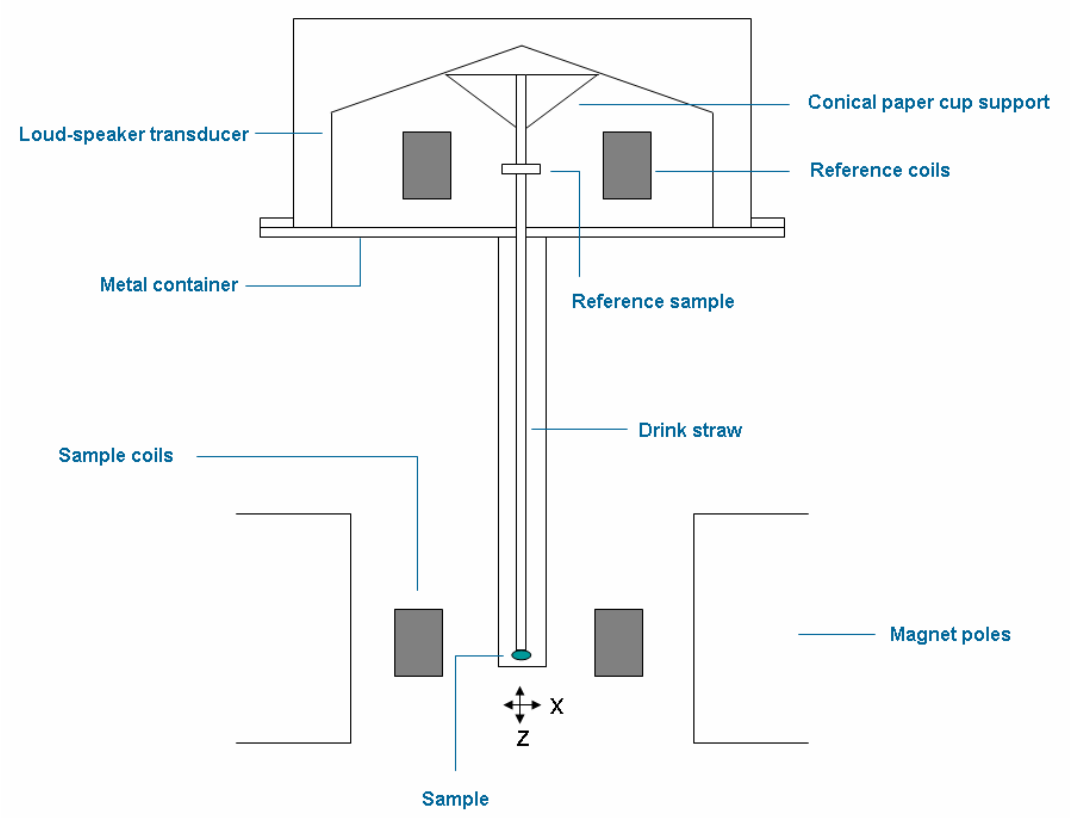


Figure 3.11: Schematic representation of vibrating sample magnetometer (VSM) [80].

The magnetization hysteresis recorded by a VSM can provide detailed information about magnetization behaviour for a given material. (Figure 3.12) Several important magnetic properties can be obtained from a M-H loop. The saturation magnetization (M_s) is the maximum absolute value of measured M. The remanence (M_r) is defined as the magnetization retained in the material after removing the applied field. The coercivity (H_c) is the field above which a permanent magnetic moment can be sustained. The squareness ($S_r \equiv M_r/M_s$) is an indication of the ability of a ferromagnetic material to retain magnetization after applied field is switched off.

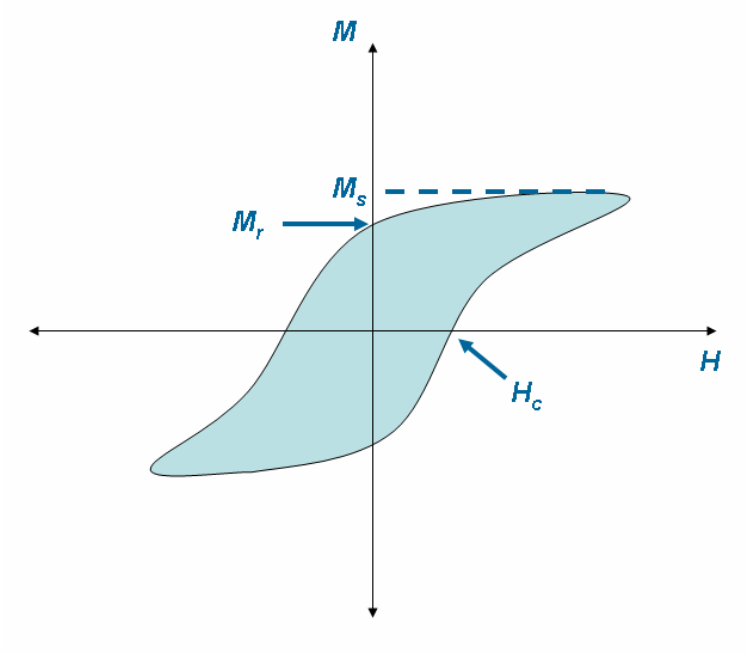


Figure 3.12: A typical hysteresis loop for a ferromagnetic material.

3.3.6 Synchrotron x-ray diffraction

The synchrotron x-ray diffraction was carried out at Stanford Synchrotron Radiation Laboratory (SSRL), USA. An electron beam is produced under a drain-current mode operation from the SPEAR (Stanford Positron Electron Accelerating Ring) machine where it was initially set for scientific use of particle physics and astrophysics (Figure 3.13). Since the radiation is very intense and reliable, it is a powerful tool for materials characterization and study of solid-state physics.

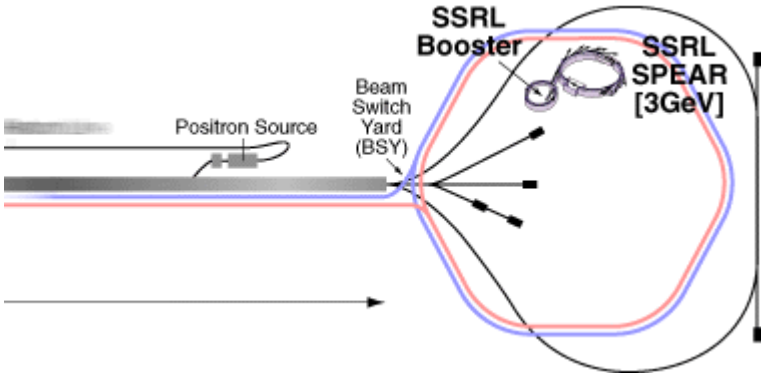


Figure 3.13: SPEAR machine at the SSRL [82].

In SPEAR, electrons and positrons travel circularly with opposite directions in the evacuated pipe. The dipole magnets are placed at a regular distance around the ring. As the charged particles circulate, synchrotron radiation is emitted by the particles themselves. This energy is restored at a storage ring and regenerated at SSRL with an energy of 3 GeV. Once the energy has been stored in storage ring, the intensity and direction of a beam of electrons can be controlled through a serial of focusing and bending magnets respectively. Additionally, the undulator is placed prior to use in each beamline station. The intensity can be increased by the undulator which consists of many small magnets causing the beam to undulate. As a result, the resultant beam is interfered and overlapped to produce a higher intensity of the beam. This highly intense beam passes through the bending magnets by deflecting the beam with a few degrees with respect to its moving path, then directed down to each beamline station. Additionally, each beamline station has its own set of optic and focusing parts. Thus, the beam at each station is optimized for different purposes.

The principle of synchrotron x-ray diffraction can be schematically represented in Figure 3.14. The constructive diffracted beam must satisfy Bragg's law. As can be seen, the scattering vector Q is the difference between the incident and diffracted beams, which is perpendicular to lattice planes. In terms of scattering vector Q, Bragg's law can be expressed by $d = 2\pi/Q$, where d is the lattice spacing and Q is the scattering vector.

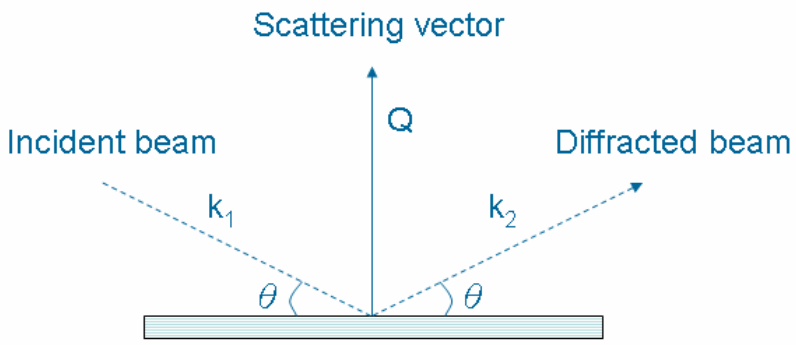


Figure 3.14: Schematic representation of x-ray scattering diffraction

Scattering Intensity is a function of the scattering vector Q or its magnitude. The length (magnitude) of scattering vector is defined as the following equation [83].

$$Q = \frac{4\pi}{\lambda}\sin\left(\frac{1}{2}(2\theta)\right)$$

The beamline 2-1 station at SSRL use a Huber diffractometer with 2-circle geometric design which controls the THETA rotation on the sample and 2THETA on the detector arm. The rotation is driven by a motor and controlled directly by the software so-call SUPER. Experiments can be carried out by setting starting angle, ending angle, counting time and scan interval. The focused beam ranging from 4000-15800 eV is used for diffraction scattering with a resolution ($\Delta E/E$) of about $5x10^{-4}$ and a spot size of 0.2 x 0.45 mm. The monochromator has a double-crystal geometry with Si(111), Si(220) or Si(400).

3.3.7 Synchrotron x-ray absorption techniques

Extended X-ray Absorption Fine Structure (EXAFS)

EXAFS has been known for several decades since Kronig attempted to explain the structural content using quantum mechanics [84]. However, a full understanding was not given until the work done by Stern in 1974 [85].

EXAFS spectroscopy is a technique to measure the x-ray absorption coefficient (μ) as a function of photon energy (*E*) above the threshold of an absorption edge in which the signal comes from the interference between outgoing (from ejected photoelectron) and incoming (from the neighbouring atom) waves. (Figure 3.15) Usually, EXAFS spectra consist of a pre-edge region and an EXAFS region. (Figure 3.16) The pre-edge region is associated with the energetics of virtual orbitals, the electron configuration, and site symmetry. The frequency of the EXAFS wave varies with the distance between the absorbing atom and the neighbouring atom. The inter-atomic distance can be estimated from the phase shift during the travelling of the photoelectron. In addition, the amplitude of the EXAFS signal corresponds to the number of neighbouring atoms surrounding the absorbing atom [86]. There is a small region, so-called x-ray absorption near-edge structure (XANES) among the EXAFS spectrum. The XANES region is suggested to cover from the edge threshold and the

point at which the wavelength of the excited electron is equivalent to the distance between the absorbing atom and its nearest neighbours, typically 50 eV above the edge [87]. The XANES spectrum contains information about the electronic structure, and its theoretical analysis involves solving the Schrödinger equation at the energy between the Fermi level (strong interaction) up to EXAFS limit (weak interaction).

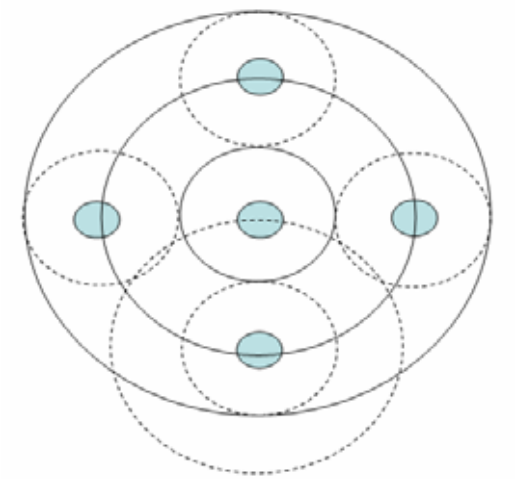


Figure 3.15: Origin of EXAFS in condensed matters. (Solid and dash line indicate outgoing and scattering waves, respectively.) [85]

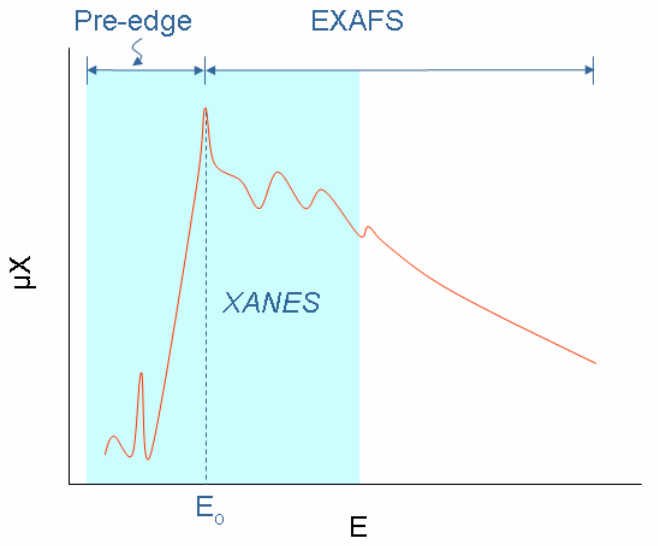


Figure 3.16: Schematic representation of a typical EXAFS spectrum.

Accordingly, an appropriate Fourier transform of the experimental EXAFS data can give information on the scattering matrix as a function of position. In addition, the availability of synchrotron radiation has greatly improved resolution to make EXAFS a powerful technique to understand structure and chemical environment for condensed

matter [88].

There are two main approaches to analyse EXAFS raw data: curve fitting and Fourier transform techniques. In both of these methods the raw data (μ and *E*) need to be converted to plot χ(*k*) *vs k* using the equations below.

$$k = \sqrt{\frac{2m}{\hbar^2}(E - E_0)}$$

where *k* is the wavevector; *E* and E_0 represent the incident photon energy and the threshold energy for the specific absorption edge; *ħ* is the Planck's constant.

$$\chi(E) = \frac{\mu(E) - \mu_0(E)}{\mu_0(E)}$$

where χ(*E*) is the modulation of the absorption rate; μ_0 and μ are the background and absorbing absorption coefficients, respectively.

EXAFS measurement was performed using the beamline 10-2 at SSRL. The beam was unfocused ranging from 4500 to 45000 eV with a spot size of 2.0 x 20.0 mm. The Si(220) crystal is used as a monochromator , and the signal is collected by Canberra 13 element fluorescence detector. The S/N ratio entirely depends on the particular experiment. In this work we mainly focus on pre-edge and XANES regions to identify the electrodeposited iron oxides and standard samples.

X-ray Magnetic Circular Dichroism (XMCD)

Soft X-ray magnetic circular dichroism (MCD) measurement can be employed to understand the local magnetization and spin behaviours in a material. The calculation of spin-dependent absorption was first suggested by Erskin *et al*. [89]. It provides an approach to investigate the magnetic structure of unoccupied band just above the Fermi energy. Additionally, Thole *et al*. [90] successfully predicted magnetic dichroism based upon the splitting of multiplet levels in an applied magnetic field.

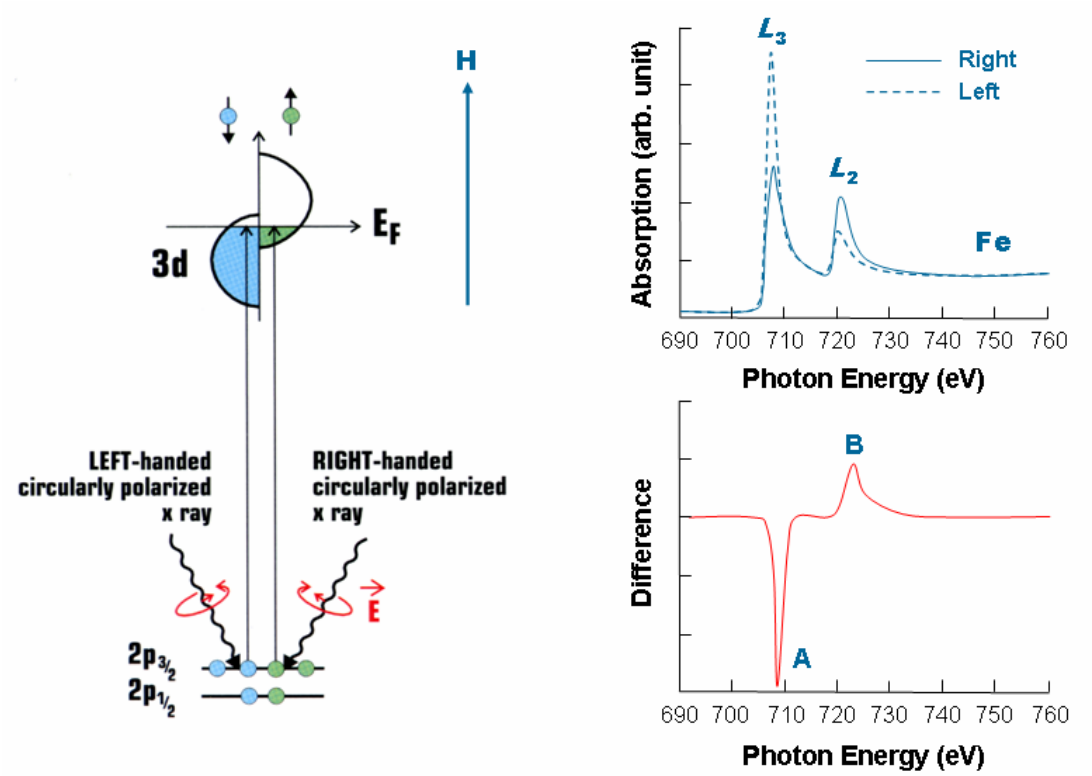


Figure 3.17: Working principle of MCD.

Although theories have been well-developed, the use of *L*-edge x-ray absorption spectroscopy is still limited because of the low energy (between 400-1000 eV). The problem was solved by using a new generation of spherical grating monochromators [91] in which the synchrotron radiation beam can be grated to single wavelength of light with a specific energy followed by energy scan on a specimen by changing the Bragg angle. During the measurement, the beam can be polarized by adjusting the magnetic field controlling the direction of the applied current. (Figure 3.17) The x-ray absorption denoted L_2 and L_3 are the electron transitions from $2p_{1/2}$ and $2p_{3/2}$ core-level to Fe 3*d* unoccupied states, respectively. The MCD signal is the difference between two polarized x-ray absorptions (*i.e.* Left and Right handed circularly polarized x-rays).

X-ray magnetic circular dichroism and x-ray absorption spectroscopic studies were performed at the National Synchrotron Radiation Research Center (NSRRC), Hsinchu, Taiwan. Figure 3.18 shows beamline 11A at National Synchrotron Radiation Research Center (NSRRC), Taiwan and its Dragon spherical monochromator. The photon energy resolution in the range of 695-735 eV is 0.4 eV and the degree of polarization

is 80%.

(a) (b)



Figure 3.18: (a) Beamline 11A of synchrotron radiation source at NSRRC; (b) Dragon spherical grating monochromator.

4. Results and Discussion

4.1 Growth of nanocrystalline Fe_3O_4 on to polycrystalline copper substrates

In this study copper was used as a conductive underlayer because of its good electrical and diamagnetic properties. The Fe_3O_4 preparation is based on the ferrite-plating method as reported by Abe *et al.* [41] and uses a conventional three-electrode cell apparatus under galvanostatic operation. The electrolyte, with an initial pH value of 6.5 consisted of 0.01 $mol \cdot l^{-1}$ ferrous ammonium sulphate ($(NH)_4\ Fe(SO_4)_2 \cdot 6H_2O$) and 0.04 $mol \cdot l^{-1}$ potassium acetate (CH_3COOK) [65]. The electrodeposition bath was kept at a constant temperature and purged with argon under vigorous stirring. For conduction, an insulated copper wire was attached on the back of the substrate and encapsulated with resin to protect the contact. A platinum wire and a gold slab were used as a counter and pseudo-reference electrode, respectively. A constant anodic current was applied using a 263A potentiostat/galvanostat from EG&G Princeton Applied Research. After the electrodeposition was complete, the as-deposited thin films were rinsed with de-ionized water and dried in a stream of nitrogen. No post-deposition treatment was performed for any of the Fe_3O_4 thin films.

X-ray diffraction was performed to identify the phases present using a Philips PW 1710 Diffractometer with Cu *K*α radiation filtered by Ni. Each XRD spectra was collected with a scan step size of 0.04^o and a scan step time of 30 s per point. Synchrotron x-ray scattering experiments were carried out using Beamline 2-1 at Stanford Synchrotron Research Laboratory (SSRL), USA. The energy of the excitation beam was 7001.5 eV. Surface topography was examined using a Molecular Imaging PicoSPM operating in contact mode. The images were obtained from a Si_3N_4 tip at a scan rate of 740 $nm \cdot s^{-1}$. A scanning Electron Microscope (JEOL JSM 5610 LV), and a field Emission Gun Scanning Electron microscope (LEO Gemini) equipped with energy dispersive x-ray spectroscopy (EDS) were used to examine microstructure and stoichiometric composition of Fe_3O_4 thin films. A STEM JEOL JEM 2010F Scanning Transmission Electron Microscope was used to study the interface between the Cu substrates and Fe_3O_4 thin films. The TEM cross-sections

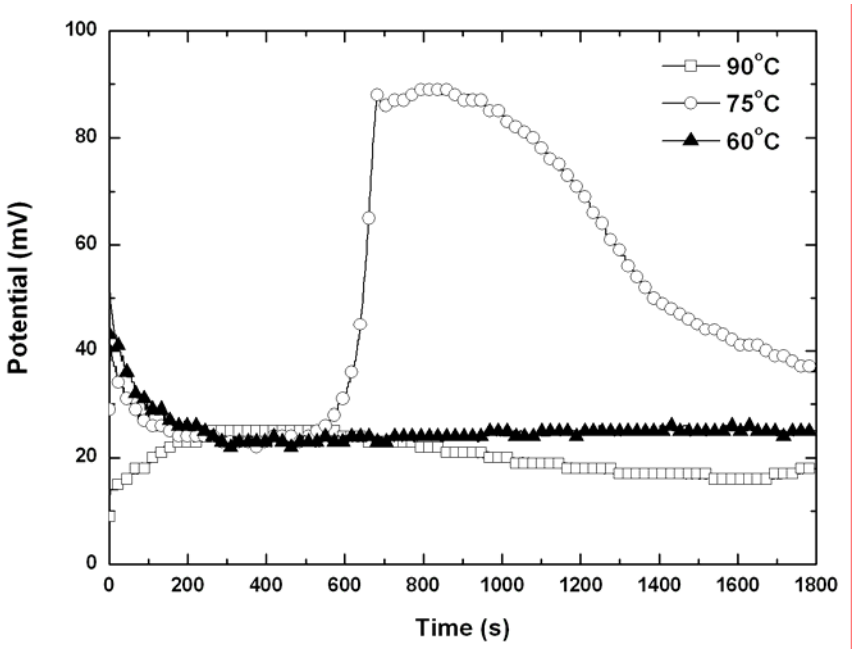
were prepared using a focused ion beam system (FIB). Hysteresis loops were recorded using an Oxford Instruments Vibrating Sample Magnetometer (VSM).

Different processing parameters such as growth temperature, deposition time and anodic current density have been varied in order to study their effect on film structure, morphology and homogeneity in detail.

Growth Temperature

Figure 4.1a shows the curves of potential versus deposition time at different temperatures for films grown at a constant current density of 0.05 $mA \cdot cm^{-2}$. There is a notable difference in the shape of the curve at a growth temperature of 75 ºC. Figure 4.2a shows the XRD patterns for the films growth at 60 ºC, 75 ºC and 90 ºC. At 60 ºC and 75 ºC there is a significant amount of α-FeOOH (goethite) formed, whereas at 90 ºC the film is pure Fe_3O_4. The Fe_3O_4 thin film has the strongest intensity at 35.4º, corresponding to (311) reflection (JCPDS No. 19-0629), which is expected to be the strongest reflection for a randomly oriented material; *i.e.* there is no preferred orientation relationship between the as-deposited film and substrate. The HRTEM micrograph of Fe_3O_4/Cu cross-section (Figure 4.2b) reveals very fine crystallinity with in the Fe_3O_4 thin film. Compared with the experimental results in Figure 4.1a, we can conclude that Fe_3O_4 can only be grown at a temperature higher than 75 ºC, below which the peak intensities for Fe_3O_4 are reduced gradually and several low-index plane peaks at 17.8 º, 21.3º and 26.3º, corresponding to (020), (110) and (120) of α-FeOOH (JCPDS No. 29-0713), start to appear.

(a)



(b)

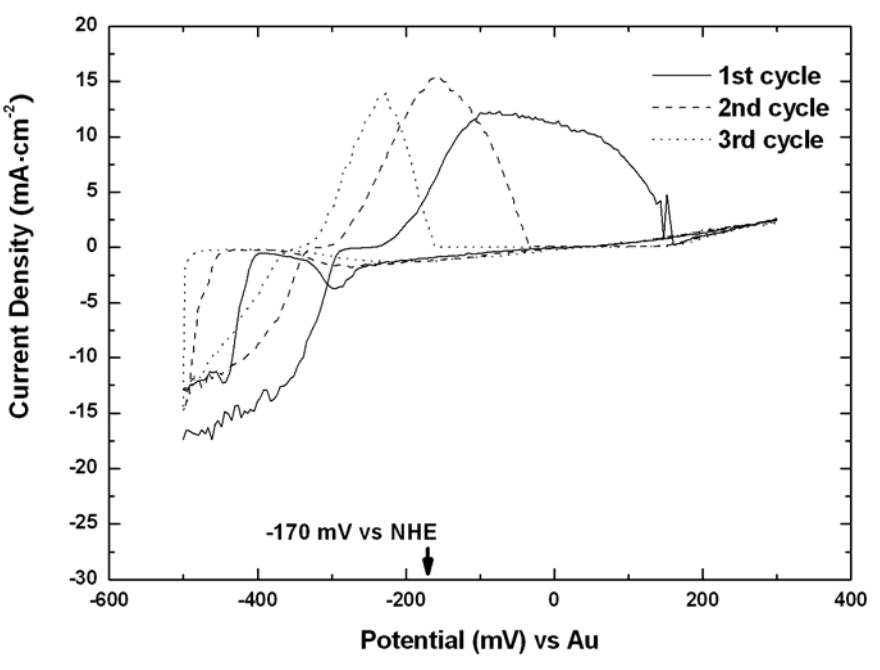
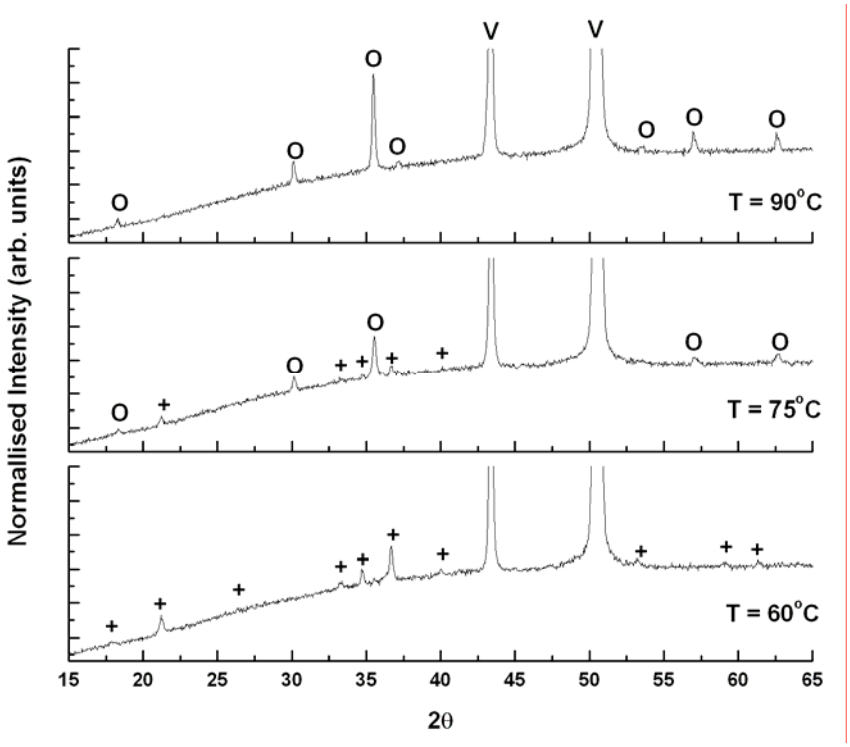


Figure 4.1: (a) Potential versus deposition time at different growth temperatures (i = 0.05 mA·cm^{-2}); (b) cyclic voltammograms at temperature of 90 ºC with a scan rate of 5 mV·s^{-1}. The arrow indicates potential theoretically calculated from Nernst equation (Appendix A-1).

(a)



(b)

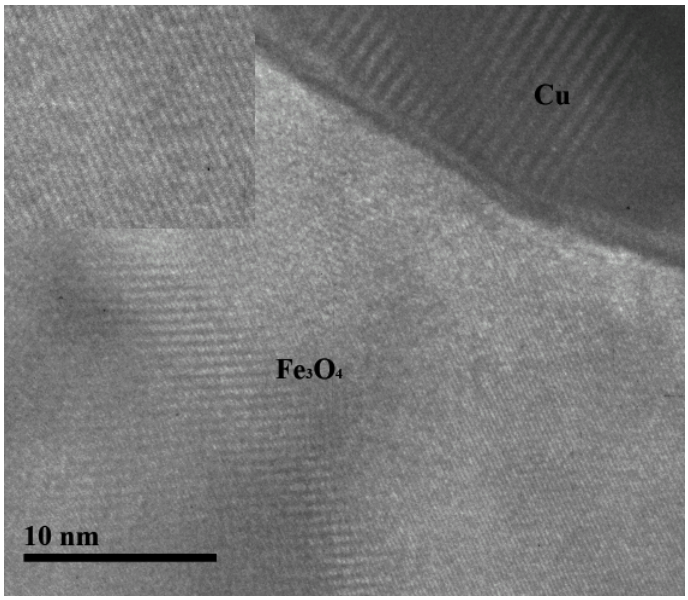


Figure 4.2: (a) XRD patterns of films deposited at various different temperatures (i= 0.05 mA·cm^{-2}. The symbols "○", "+" and "v" represent Fe_3O_4, α-FeOOH and Cu, respectively); (b) HRTEM micrograph of Fe_3O_4/Cu cross-section showing a smooth coherent interface and clear lattice planes (inset) in Fe_3O_4. Note that the strong background in the XRD data is due to substrate (Cu) florescence and is not related to the film itself.

Figure 4.3a, 4.3b and 4.3c reveal the microstructure of the electrodeposited films grown at 90 ^{o}C, 75 ^{o}C and 60 ^{o}C, respectively. At a lower temperature an acicular grain structure (Figure 4.3b and 4.3c) is observed and this corresponds to samples formed of α-FeOOH (based on XRD analysis). In the sample where we observe both Fe_3O_4 and α-FeOOH (Figure 4.3b) the surface roughness is found to increase and a potential during deposition show a large peak not present at other temperatures.

The formation of Fe-oxides and hydroxides under these conditions has been thoroughly reviewed by Misawa [92]. The transition to formation of α-FeOOH rather than Fe_3O_4 can be understood by considering the right-shift of Fe^{2+}/Fe_3O_4 boundary line (Figure 2.9) in the Pourbaix diagram with temperature. Fe_3O_4 growth is thermodynamically preferred at higher temperature in low pH value of electrolytes [93]. Based on the thermodynamic data we can determine that there are two main reactions taking place in our experiments.

T = 90 ^{o}C

$$3Fe^{2+} + 4H_2O = Fe_3O_4 + 8H^{+} + 2e^{-} \qquad (1)$$

T = 75 ^{o}C

$$3Fe^{2+} + 4H_2O = Fe_3O_4 + 8H^{+} + 2e^{-} \quad \text{(Before transition)}$$

$$Fe^{2+} + 2H_2O = \alpha\text{-FeOOH} + 3H^{+} + e^{-} \quad \text{(After transition)} \qquad (2)$$

T = 60 ^{o}C

$$Fe^{2+} + 2H_2O = \alpha\text{-FeOOH} + 3H^{+} + e^{-}$$

In the case of the oxide film grown at 75 ^{o}C, Fe_3O_4 is initially deposited on the copper substrate *via* reaction (1). However, the pH value decreases with increasing time due to the hydrolysis reaction (1). Fe^{2+} ions are predicted to oxidise to α-FeOOH (reaction (2)) in such acidic solution [92], and then deposit on top of the Fe_3O_4 film surface (Figure 4.3b).

Additionally, we observe that a few small pin holes, ranging from several hundred nm to μm appear on the Fe_3O_4 thin films when the growth temperature is greater than 90 ºC. Figure 4.3d shows a film deposited at 95 ºC and large pin holes are clearly seen;

these are consistent with the onset of gas evolution at the electrode surface at this solution temperature.

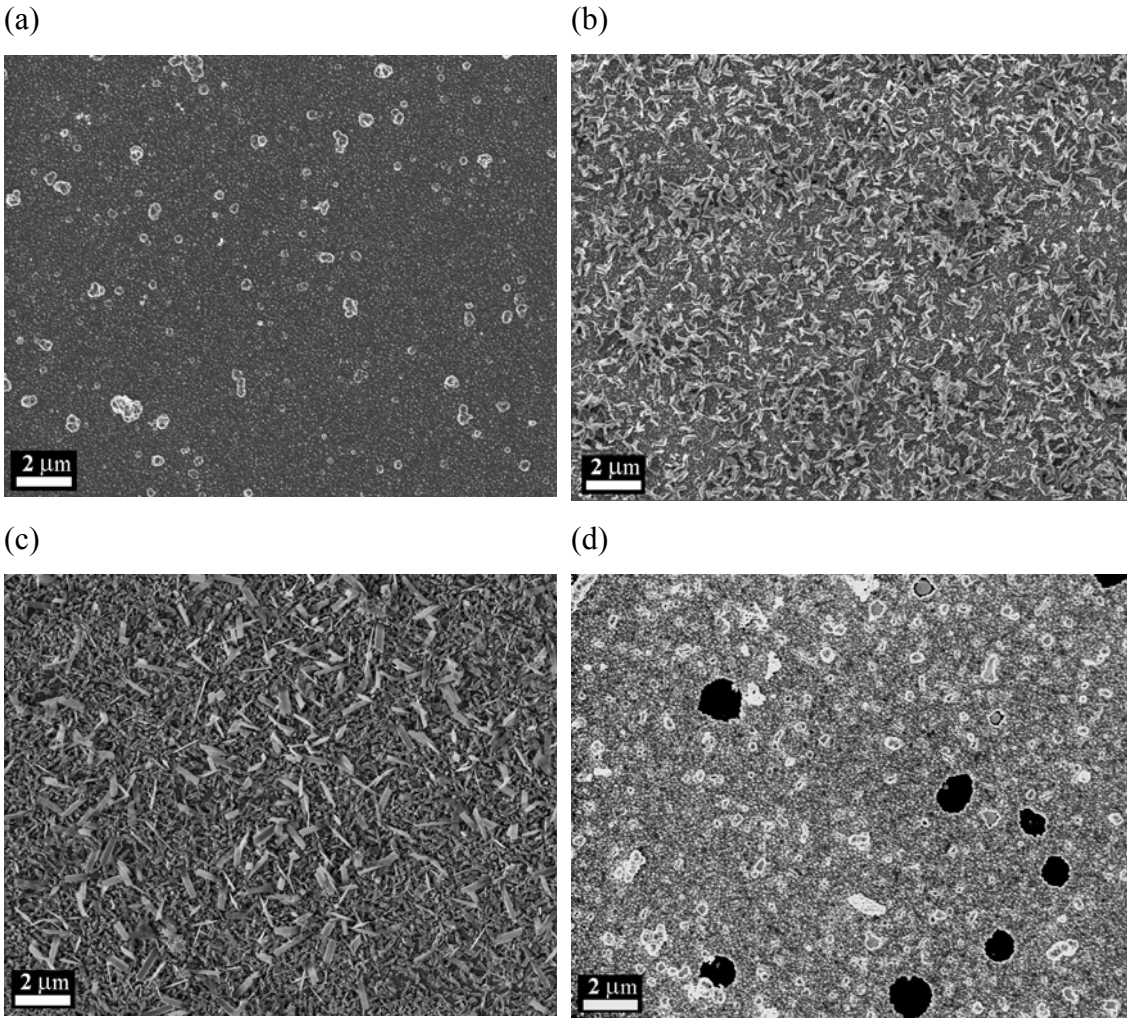


Figure 4.3: FEGSEM micrographs of electrodeposited films at (a) 90 ^{o}C, (b) 75 ^{o}C, (c) 60 ^{o}C and (d) 95 ^{o}C, showing clear changes in deposit morphology. 3(d) shows the development of pinhole type defects at the higher deposition temperature.

The AFM image (Figure 4.4a) reveals the surface topography of Fe_3O_4 grown at 90 ^oC for 30 min. The film surface is very smooth, apart from small clusters on the surface. The grain size under the growth condition is about 200 nm, in agreement with that of the Fe_3O_4 grown on polycrystalline gold substrates [45]. Using the XRD measurements the particle (crystallite) size was also calculated using Scherrer equation:

$$t = \frac{0.9\lambda}{B \cdot Cos\theta}$$

where t is particle size, λ is the wavelength of Cu K_α; B is FWHM (full width at half maximum) of the broadened diffraction line on the 2θ scale (radians).This calculation gives the average value of ~35 nm (see Appendix A-3), considerably small than FEGSEM and AFM data, indicating that the particles observed are in fact polycrystalline.

(a) (b)

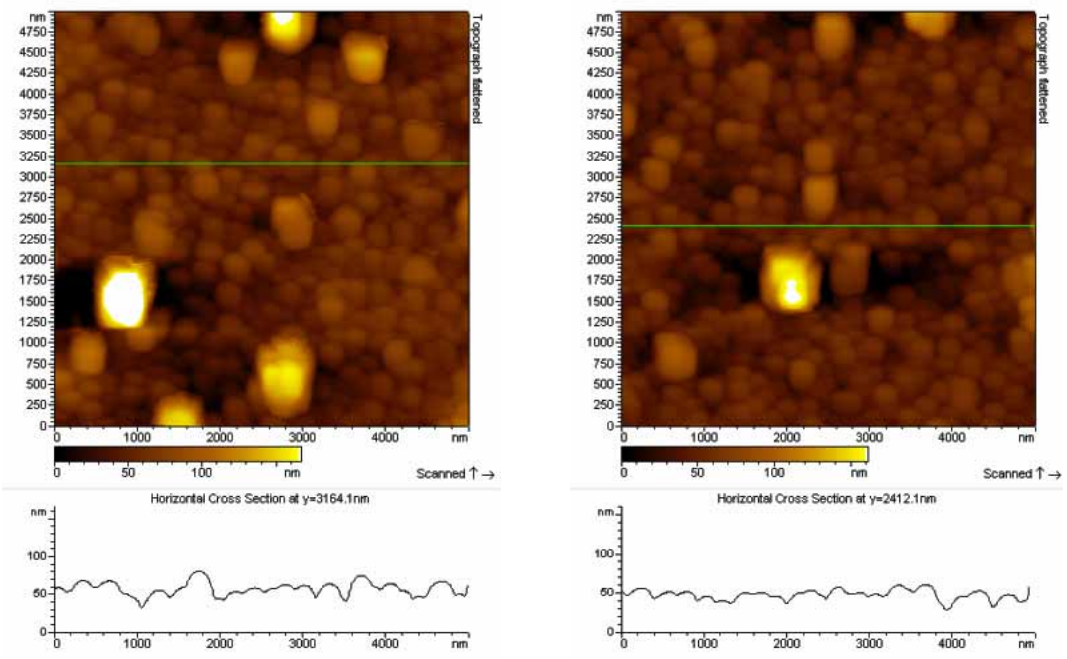


Figure 4.4: AFM images show surface roughness. (a) $t_{deposition}$ = 30 min (rms roughness = 38 nm); (b) $t_{deposition}$ = 50 min (rms roughness = 30 nm).

FEGSEM image (Figure 4.5) also indicates the presence of clusters formed on the surface of Fe_3O_4 thin films. The origin of these clusters is probably related to an anomalous growth mechanism as observed in other electrodeposition system [94]. However, we have not been able to determine the underlying substrate effects that give rise to their nucleation.

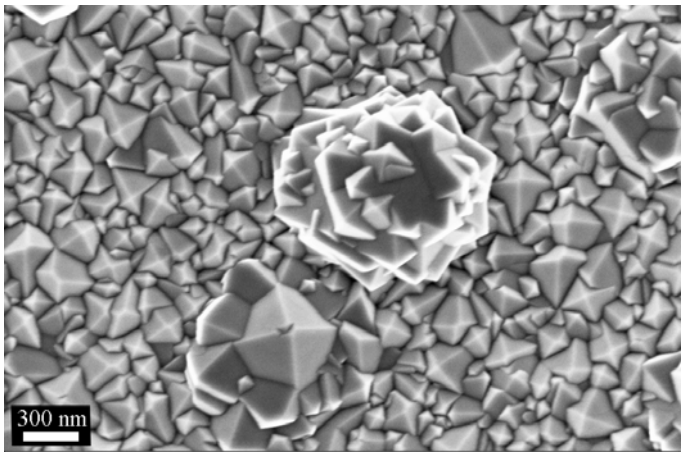


Figure 4.5: FEGSEM image of Fe_3O_4 thin film grown at 0.05 $mA \cdot cm^{-2}$ for 30 min showing surface anomalies.

Figure 4.6 is the M-H loop of electrodeposited Fe_3O_4 thin film grown at 90 ^oC at a constant current density of 0.05 $mA \cdot cm^{-2}$. The applied magnetic field is parallel with the film plane. As can be seen, the as-deposited Fe_3O_4 is very soft with a coercivity of 105 Oe. This value is slightly higher than that reported in the literature [45]. It could be due to a small of impurity such as three-valence of iron oxides or iron hydroxides present in the film. The magnetic moment is not fully saturated at 3 kOe, whereas the saturation field is about 310 Oe for bulk Fe_3O_4 material [95]. Similar results were observed for the film prepared using other deposition techniques [48, 96].

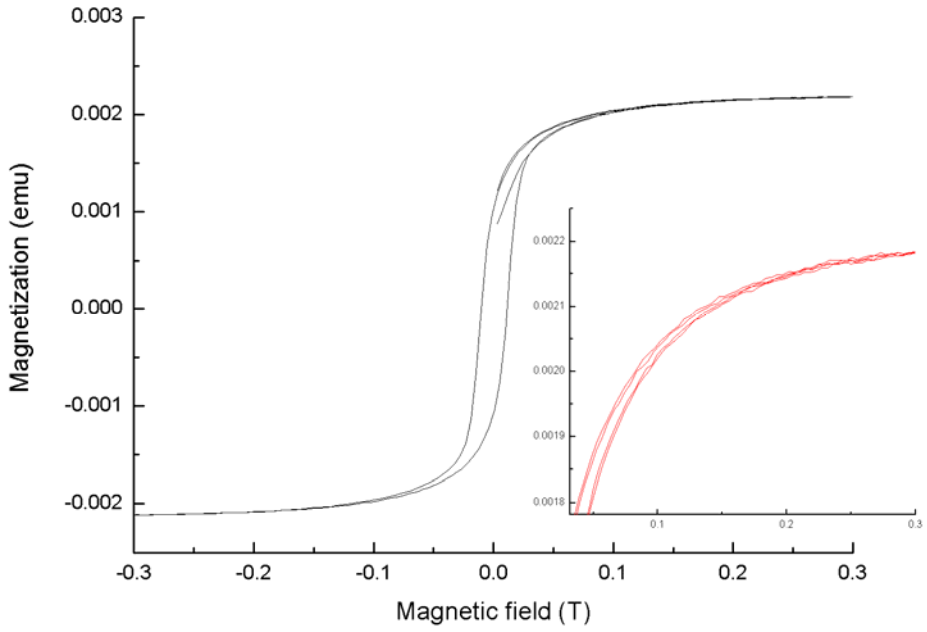


Figure 4.6: M-H loop of electrodeposited Fe_3O_4 thin film recorded at 290 K.

Deposition Time

At a constant current density of 0.05 mA·cm^{-2} at 90 ^{o}C the average deposition rates are around 0.092, 0.062 and 0.057 nm·s^{-1} for deposition times of 30, 40 and 50 min respectively (based on thickness measurement from FIB sections). This corresponds to 80%, 54% and 50% current efficiency for deposition, assuming that reaction (1) is the only one producing Fe_3O_4 in the system. The rate of increase in film thickness for Fe_3O_4 would be expected to remain constant if sufficient Fe^{2+} ions and the oxidising reagent (e^- or O_2/air) exist in electrolyte [41]. However, we found the deposition rate decreases as the deposition time increases. This can be associated with the depletion of Fe^{2+} ions from electrolyte [97]. The cyclic voltammogram (Figure 4.1b) indicates that the positions of the anodic peaks, corresponding to the oxidation of Fe^{2+} ions, ranging from -200 mV to 150 mV *vs.* Au [~-460 to -110 mV *vs.* NHE] at a scan rate of 5 mV·s^{-1} (the potential calculated from Nernst equation is indicated on the diagram). As the number of cycles increases, the anodic peak shifts to a lower potential regime. This is due to the incomplete reduction of the Fe^{3+} oxide. Indeed, there is no strong reduction peak observed in the present voltammetry, unlike that presented by Carlier *et al.* who observed two-stage reduction of anodically deposited oxides [45]. Note that the pH value change is small from 6.5 to 5.4, 5.6 and 5.5 for first, second and third cycle respectively. AFM images for different deposition times are shown in Figure 4.4.

Interestingly the film surface is considerably smoother than the copper substrate prior to electrodeposition. In the case of the Fe_3O_4 thin film grown for 50 minutes at 90 ^oC, the rms (root-mean-square) roughnesses are 95 nm and 30 nm over a scan size of 5 μm x 5 μm, for the substrate and film respectively. Moreover, the EDS analysis shows that there is no difference in chemical composition with deposition time (Figure 4.7). It is worth noting that the ratios of Fe to O are slightly lower than 0.75 in the stoichiometric bulk Fe_3O_4. This is possibly associated with limitation of sensitivity for the thin film materials (< 200 nm) with less photoelectrons excited from the film.

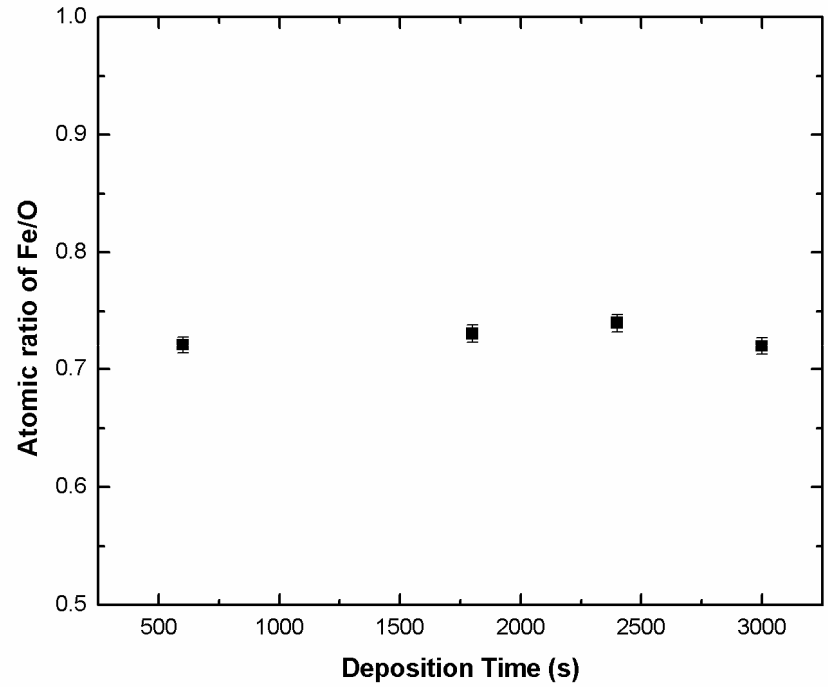


Figure 4.7: Composition variation (Fe:O ratio) of ferrite films with deposition time as determined by EDS analysis.

Current Density

The applied current density is found to play a crucial role, associated with the particle size and surface roughness of thin films in electrodeposition. According to the XRD spectra shown in Figure 4.8, there is only one single phase of Fe_3O_4 present in the as-deposited films for all the studied current densities. It seems that adjusting the applied current density does not change the crystallographic structure in this regime. Figure 4.9a and 4.9b show FEGSEM images of Fe_3O_4 grown at 0.005 and 0.5 $mA \cdot cm^{-2}$, respectively. The film surface grown at the lower current density has an

average grain size of 100 nm and is covered by considerable clusters and small voids. This could be because relatively small current density can not provide enough driving force to form a dense film structure. In contrast, the Fe_3O_4 thin film electrodeposited at the higher current density grows randomly and has a rougher surface compared to the films grown at low current density. Additionally, there is a large distribution of particle sizes, ranging from ~200 to ~700 nm. In comparison with Figure 4.3a, the sizes of clusters due to anomalous growth become bigger with increasing current density. These types of defects are known to be especially detrimental to electronic and magnetic properties [94]. EDS analysis indicates these loose clusters consist of Fe and O atoms only, although the exact phase has not yet been determined.

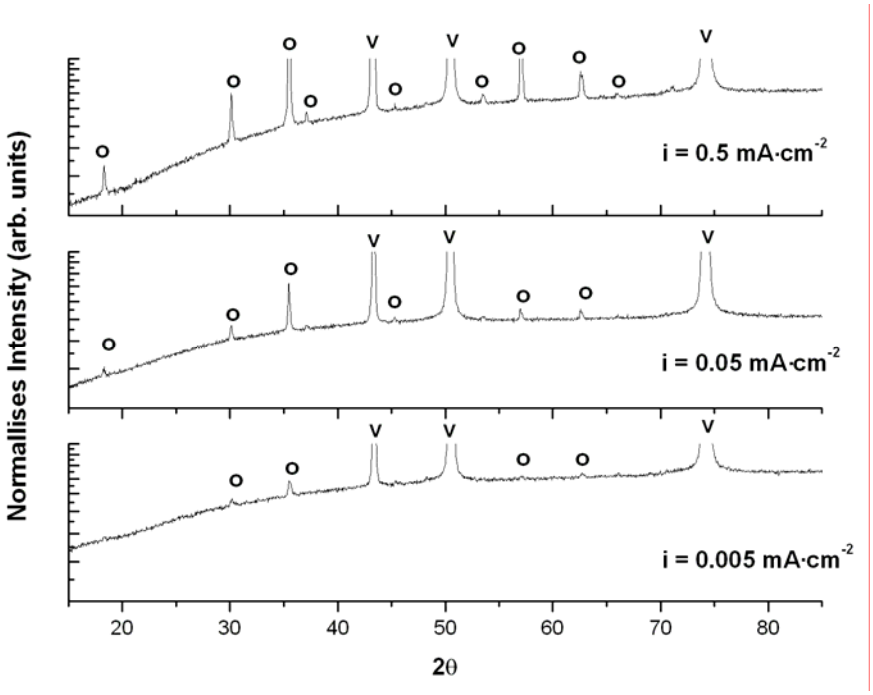
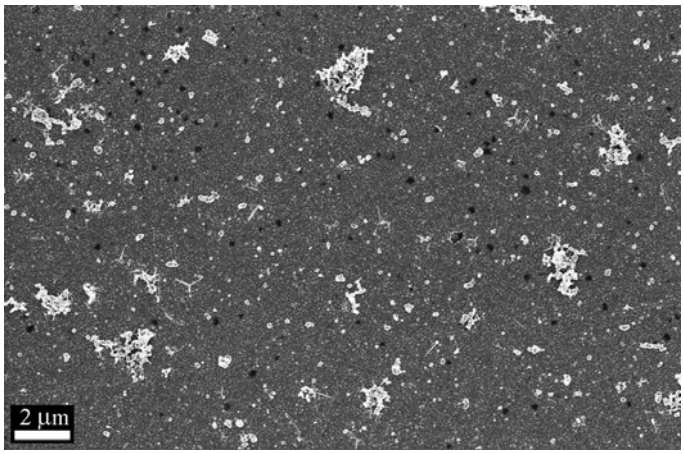


Figure 4.8: XRD patterns of films deposited at various applied current density. The symbols "○" and "v" represent Fe_3O_4 and Cu, respectively.

(a)



(b)

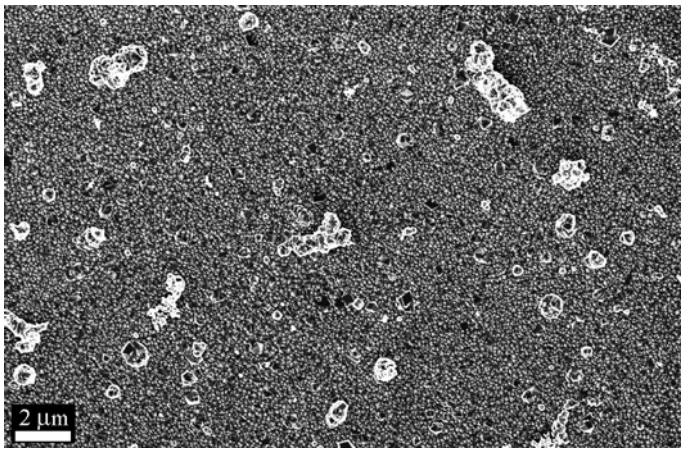


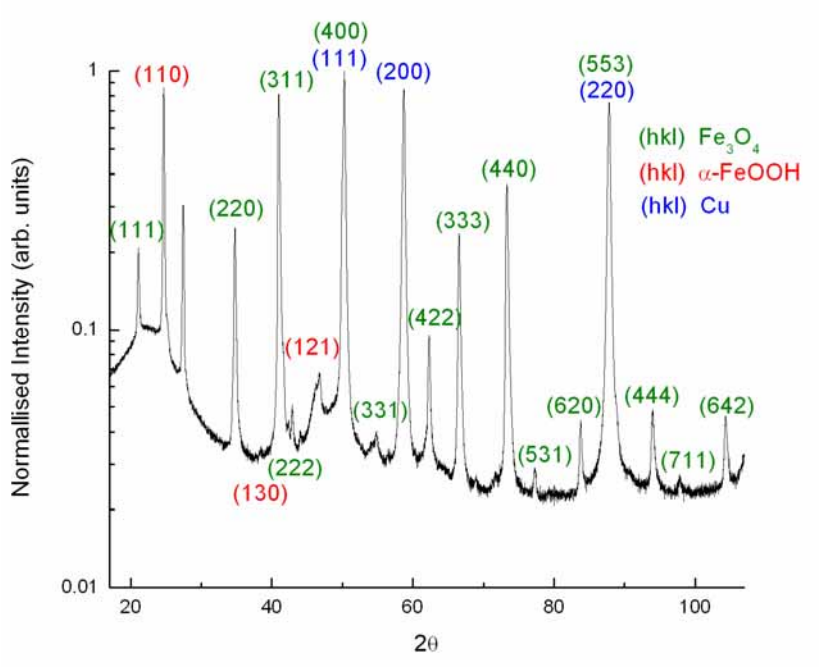
Figure 4.9: FEGSEM micrographs of Fe_3O_4 prepared at 90°C with (a) 0.005 mA·cm^{-2} and (b) 0.5 mA·cm^{-2} for 30 min.

Figure 4.10 shows the synchrotron x-ray scattering patterns of the iron oxide films electrodeposited at 0.005, 0.05 and 0.5 mA·cm^{-2} respectively (corresponding to the potentials of ~5 mV, ~25 mV and ~150 mV *vs*. Au reference electrode). The Fe_3O_4 film can be obtained at a current density of 0.005 mA·cm^{-2} (Figure 4.9a), although a few peaks appear at 24.69°, 38.37° and 46.53°, corresponding to (110), (130) and (121) of α-FeOOH. An unknown peak was also found at 27.43°. The formation of α-FeOOH is possibly caused by acidic electrolyte mentioned previously. At higher applied current density, *i.e.* 0.05 mA·cm^{-2} single phase of Fe_3O_4 seems to be preserved but more unidentified peaks appear. We find that none of the known iron oxide or hydroxide patterns match these peaks. As further increasing current density to 0.5 mA·cm^{-2}, more Fe^{2+} ions are oxidised. As a result, α-FeOOH forms and coexists with

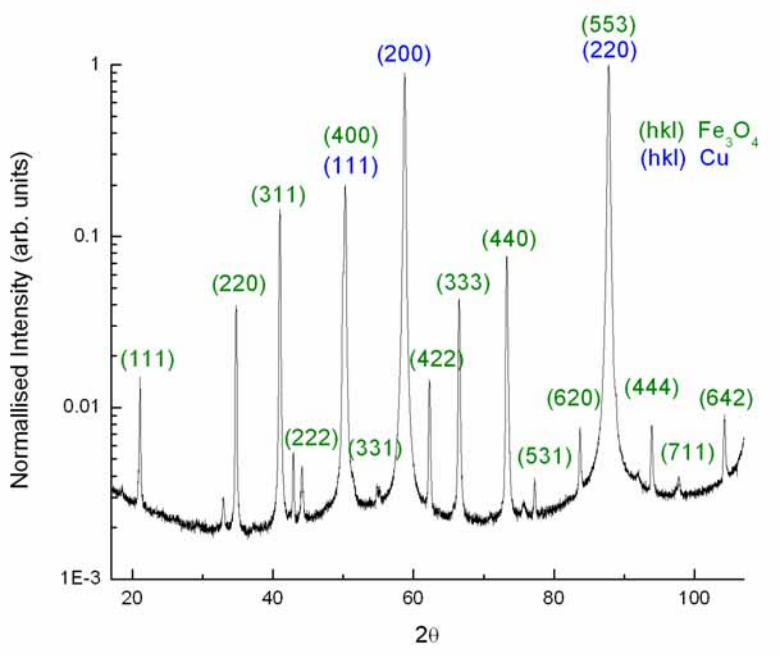
Fe_3O_4 (Figure 4.10c). The detailed growth mechanism of α-FeOOH is discussed in later sections.

Additionally, there seems to be a slight dependence of lattice parameter of Fe_3O_4 with applied current density. That is, the higher current density, the larger is the lattice constant of Fe_3O_4 as shown in Table 4.1.

(a)



(b)



(c)

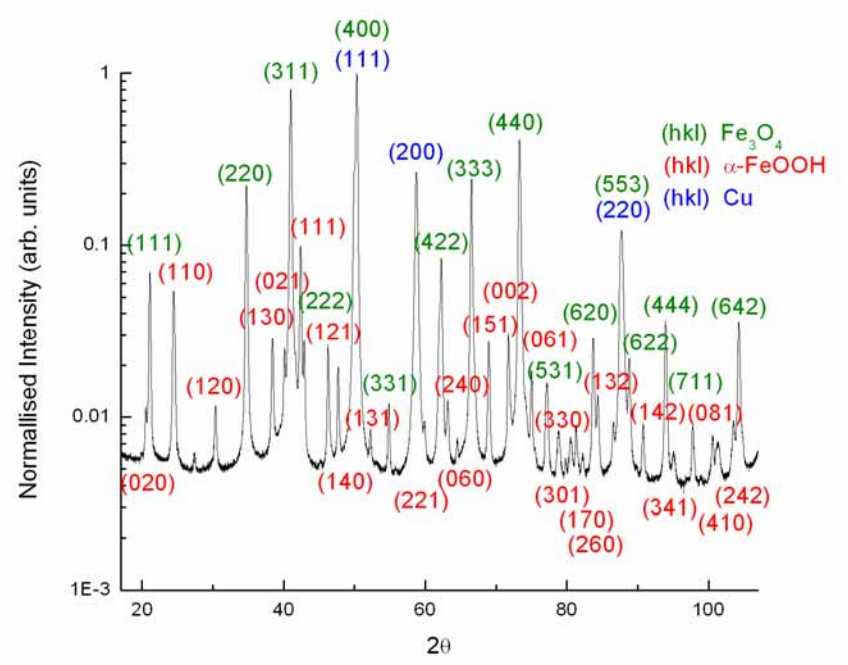


Figure 4.10: Synchrotron x-ray scattering of Fe_3O_4/Cu substrate. (a) i = 0.005 mA·cm^{-2}; (b) i = 0.05 mA·cm^{-2}; (c) i = 0.5 mA·cm^{-2}.

Plane	0.005 mA·cm^{-2}	0.05 mA·cm^{-2}	0.5 mA·cm^{-2}
(220)	0.8383	0.8389	0.8388
(311)	0.8383	0.8389	0.8386*
(440)	0.8387	0.8392	0.8390

Table 4.1: Lattice constants extracted using the three main diffraction peaks in Fe_3O_4 (Unit: nm; the symbol "*" represents an overlap peak)

Film Homogeneity

The film homogeneity is a crucial consideration to fabricate high-performance electron spin-manipulating devices. STEM images (Figure 4.11) show the columnar structure of Fe_3O_4 nucleated heterogeneously and grown on a polycrystalline copper substrate at 90 ^{o}C. The contrast in the ADF STEM image (Figure 4.11b) could be due to either composition difference or grain orientation. However, we find that Fe_3O_4 thin film grown on amorphous substrates shown no strong contrast under the same growth condition (see Figure 4.19c). Therefore, the film homogeneity seems to be affected by

grain structure or grain boundary regions of the substrate material.

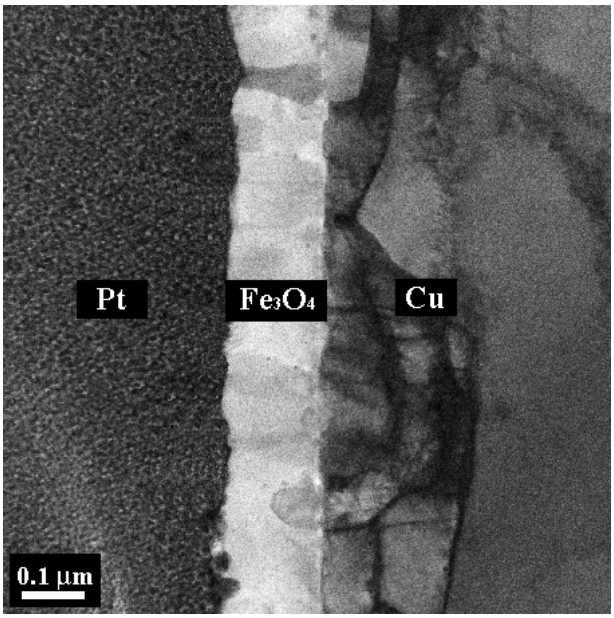
Summary of the Effect of Temperature and Applied Current Density

The film properties of electrodeposited Fe_3O_4 thin films are significantly affected by growth temperature and applied current density. Single phase Fe_3O_4 can only be obtained for a limited window ($T > 75\ ^oC$). A lower temperature is favourable for the growth of iron oxyhydroixde (α-FeOOH). This was explained by considering the thermodynamic phase stability as a function of temperature.

Larger grains of Fe_3O_4 were obtained when higher current densities were applied, and the film was found to be significantly rougher than those formed at lower current densities. This can be understood by considering the nucleation and growth rate of the magnetite films.

In addition, the growth of Fe_3O_4 films was found to be strongly affected by the grain boundaries in the substrate. This may have implications for device strutures using polycrystalline substrate materials.

(a)



(b)

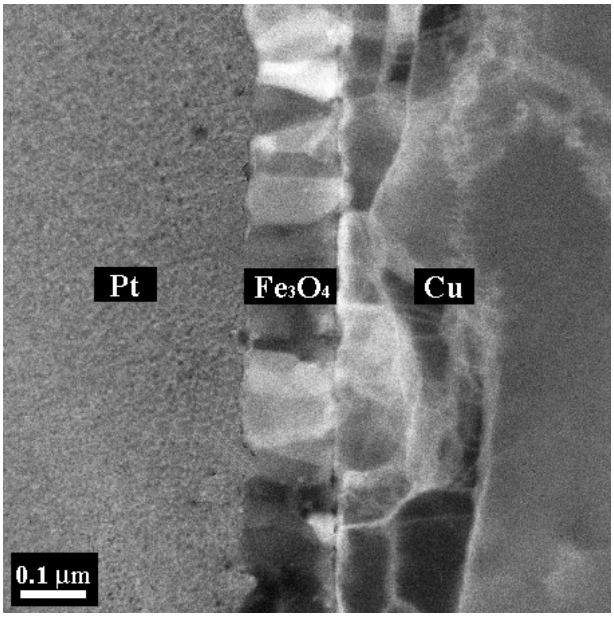
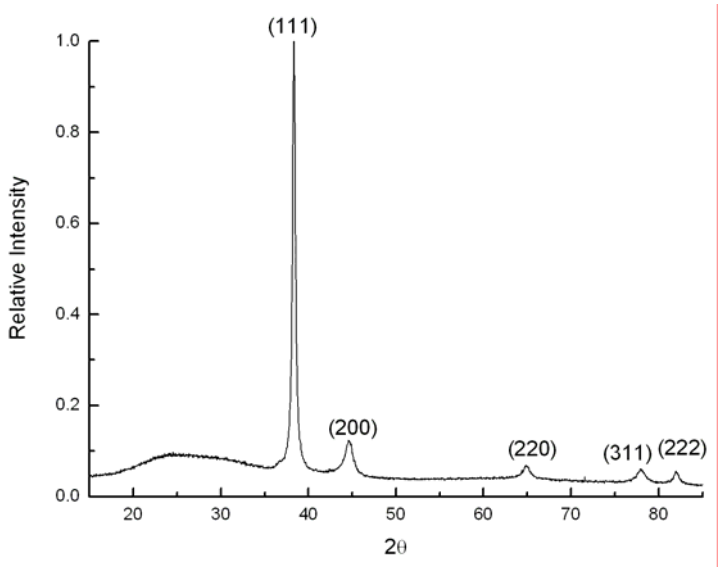


Figure 4.11: STEM image of Pt/Fe_3O_4/Cu cross-section. (a) bright-field (BF) image; (b) annular dark-field (ADF) image.

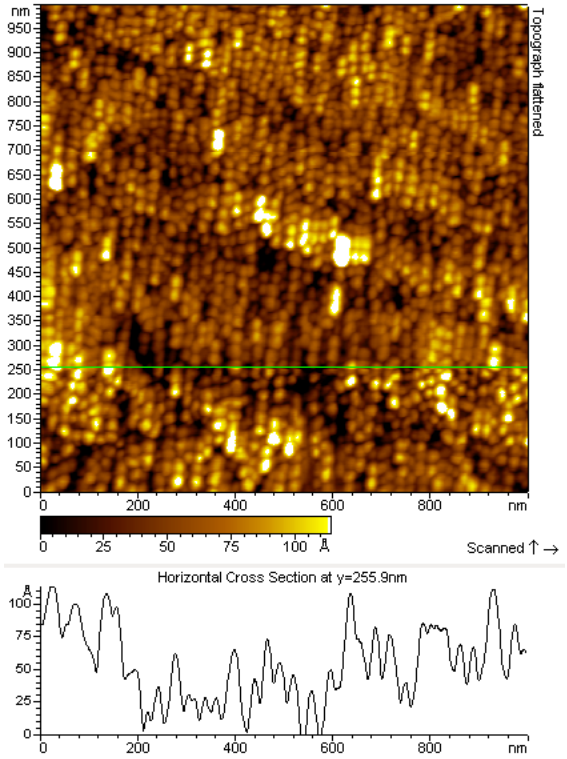
4.2 Time-dependent growth of Fe_3O_4 onto gold/glass substrates

In the previous section Fe_3O_4 thin films grown electrochemically onto copper foils under galvanostatic operation were examined. The film thickness increases with increasing deposition time. Here, the detailed growth mechanism of Fe oxides films will be further studied. Textured gold substrates were used as the working electrode and were prepared as described in Section 3.1. The metal thickness was about 50 nm with a crystallographically oriented (111) plane. Figure 4.12a shows the XRD spectrum of the substrate material: 50 nm Au on glass. The slightly high background signal in the XRD spectrum is due to amorphous glass and the intensity of the (111) is indicative of showing texture in the film. According to AFM data, the surface is very smooth with an rms roughness of 10 nm and grain size is about 30 to 40 nm, (Figure 4.12b) consistent with SEM observation. (Figure 4.12c)

(a)



(b)



(c)

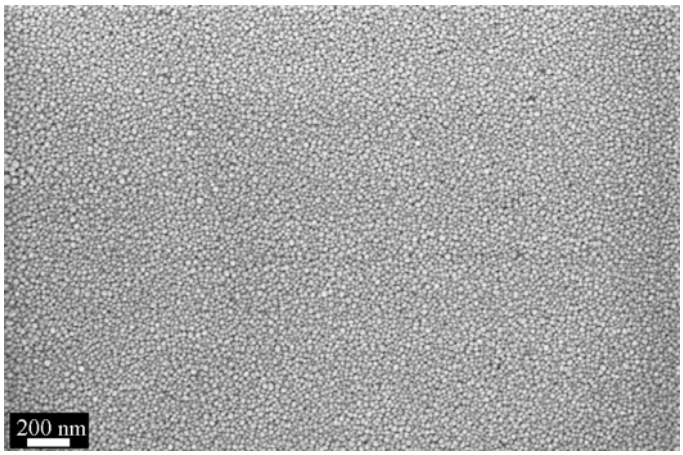


Figure 4.12: Crystallography, topography and morphology of gold/glass substrates. (a) XRD; (b) AFM; (c) FEGSEM.

To study the growth mechanism, Fe_3O_4 thin films were grown electrochemically onto gold/glass substrates. The substrate was dipped in 5% HF to remove any surface contamination from gold. The electrolyte consists of 0.01 M $(NH_4)_2Fe(SO_4)_2{\cdot}6H_2O$ and 0.05 M CH_3COOK. The bath temperature was maintained at 80 ^oC. Under these conditions, Fe_3O_4 can be obtained by applying a constant potential of 25 mV (as

described in Section 4.1). Time-dependent growth was observed using field-emission type SEM (Figure 4.13) for films deposited for a range of times. The electrodeposition was carried out for 10 to 1800 s.

As can be seen, even at the shortest deposition time of 10 s, nucleation of Fe_3O_4 is observed on the gold. (Figure 4.13a) Increasing the time up to 30 s, the Fe_3O_4 grains become larger; however, the grains exhibit an irregular shape. At a deposition time of 60 s, the grains start coarsening/coalescence. The average grain size is now about 100 nm. It is worth noticing that the SEM micrograph shows that the surface of the gold/glass substrate is still not fully covered by Fe_3O_4 particles. The homogeneous growth of Fe_3O_4 is observed up to 300 s deposition. Morphologically, the grain shape changes to have a sharp cubic microstructure. Few larger grains are observed on the film surface, associated with grain coalescence. The microstructure of Fe_3O_4 starts to change at a deposition time of 600 s (Figure 4.13e). The grain shape becomes octahedral or rhombic. This is because the {111} and {110} are the most stable surfaces [98] and so the growth is not preferred to other higher energy surfaces. The grains keep growing up to a deposition time of 1800 s, with a characteristic of polycrystalline Fe_3O_4 shown in Figure 4.13f.

According to growth mechanisms proposed by Abe *et al.* [41], the formation of Fe_3O_4 can be described as layer-by-layer growth. In this study, SEM micrographs reveal the nucleation and growth of Fe_3O_4 *particles* leading to a coherent film. At the beginning of deposition, the nucleation process takes place on the gold/glass substrate following the mechanism described in [41]. Having made a presumption that the gold surface is homogenously terminated by OH^- ions, Fe^{2+} ions can attached onto these ions, and then partial oxidation occurs on application of the anodic potential. However, it seems the nucleation process has favourable sites, possibly provided by existing Fe_3O_4 particles in the electrolyte or by inhomogeneously nucleating at more active on the substrate, meaning the nucleation process is heterogeneous. During the stage of growth, coalescence and Oswald ripening occur, in which two adjacent grains coarsen in order to decrease the interfacial energy between them [99]. With absorption of $FeOH^+$ ions, the grains coarsen to increase their size only if Fe^{2+} ions are present by the diffusion or reaction kinetics but a critical size is applicable in terms of thermodynamics at the nucleation state.

In this study, the growth mechanism of electrodeposited iron oxides films was carefully investigated by a means of time-dependent growth. The SEM micrographs indicated that a heterogeneous nucleation takes place on the surface of gold/glass substrate. During the deposition the coalescence and Oswald ripening occur, and grains become larger. It takes up to 300 s to ensure complete coverage of Fe_3O_4 on the substrate surface.

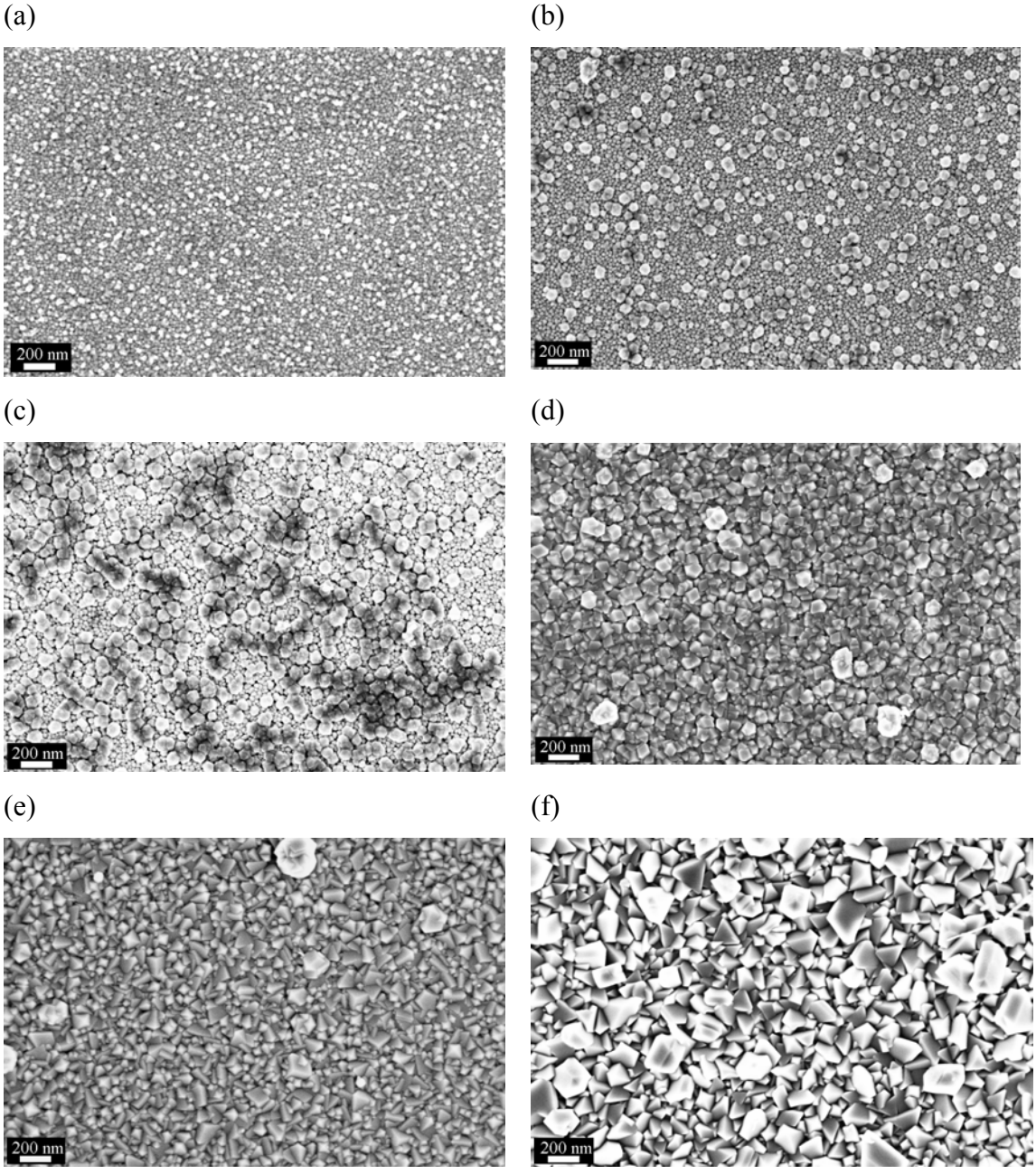


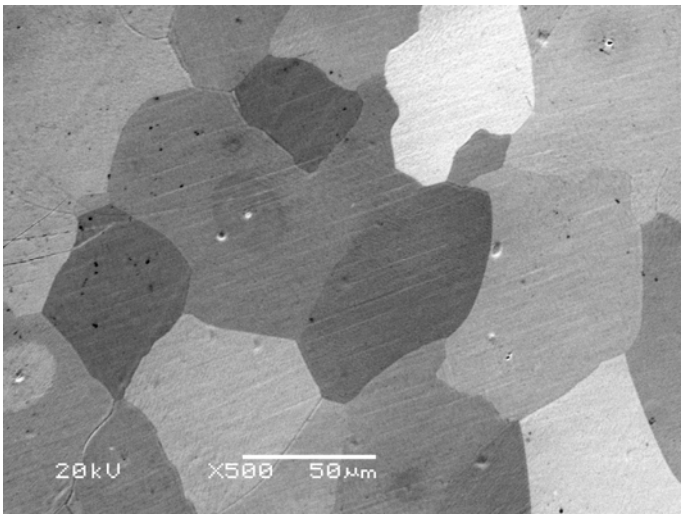
Figure 4.13: Time-dependent growth of Fe_3O_4 onto gold/glass substrates at 80 ^oC under a constant potential of 25 mV. (a) 10 s; (b) 30 s; (c) 60 s; (d) 300 s; (e) 600 s; (f) 1800 s.

4.3 Growth of multilayered Fe-based oxides

RABiTS Ni substrates with {100}<001> crystallographic orientation were used to grow air-formed NiO. The microstructure of RABiTS tape is shown in Figure 4.14a. The average grain size is approximately 50 μm. Figure 4.14b shows an X-ray pole figure of single phase Ni tape, corresponding to exactly (100) texture with a FWHM value of 8-10^{o} (See appendix A-4). AFM images (Figure 4.15) show the surface topography of Ni{100}<001> substrates before and after etching. The Ni tape with the thick native nickel oxide on the top has a relatively rougher surface compared to as-etched one, though un-etched Ni tape has a smaller rms roughness. Note that triple-point grain boundaries are found on the as-etched Ni tape in Figure 4.15b. The deepest depth of grain boundaries is about 20 nm. As a result, the formation of grooving has to be taken into account if growing a thin oxide layer on the substrate for spintronic application.

In order to obtain a condensed oxide structure Ni tapes were placed in a desiccator for 72 hrs. The electrodeposition used a three-electrode cell apparatus under galvanostatic control using an ACM GillAC potentiostat. The electrolyte consists of 0.01 M $(NH_4)_2Fe(SO_4)_2{\cdot}6H_2O$ and 0.05 M CH_3COOK (pH buffer). Under this electrolyte composition, Fe_3O_4 and α-FeOOH can be grown at 80 ºC and 60 ºC at 0.025 $mA{\cdot}cm^{-2}$, where a platinum wire and gold slab serves as counter and reference electrodes, respectively. The sandwich structure of Fe_3O_4/α-FeOOH/Fe_3O_4 onto the NiO/Ni substrate for MTJ's can be obtained by a successive electrodeposition at two different electrolyte baths.

(a)



(b)

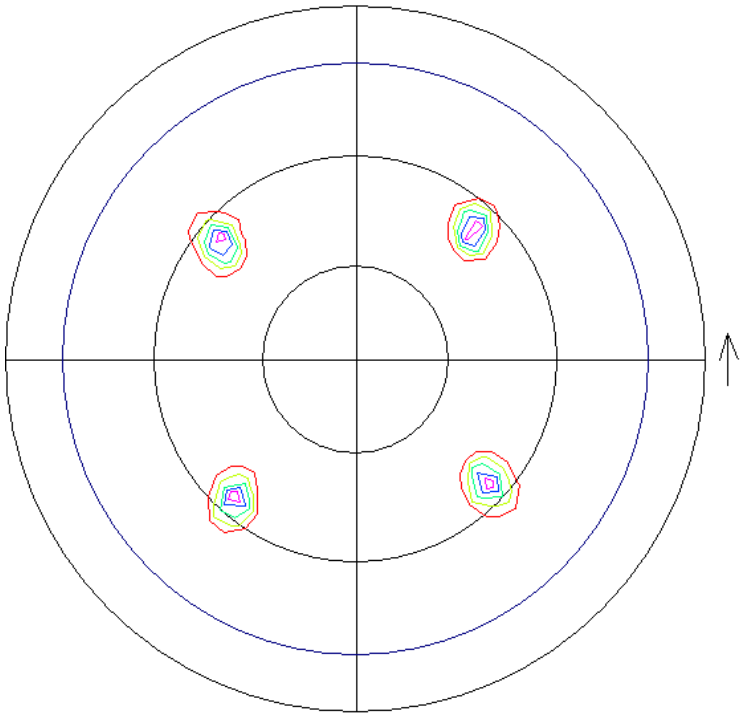


Figure 4.14: (a) SEM image of the RABiTS Ni Tape, (b) (111) pole figure of Ni{100}<001>.

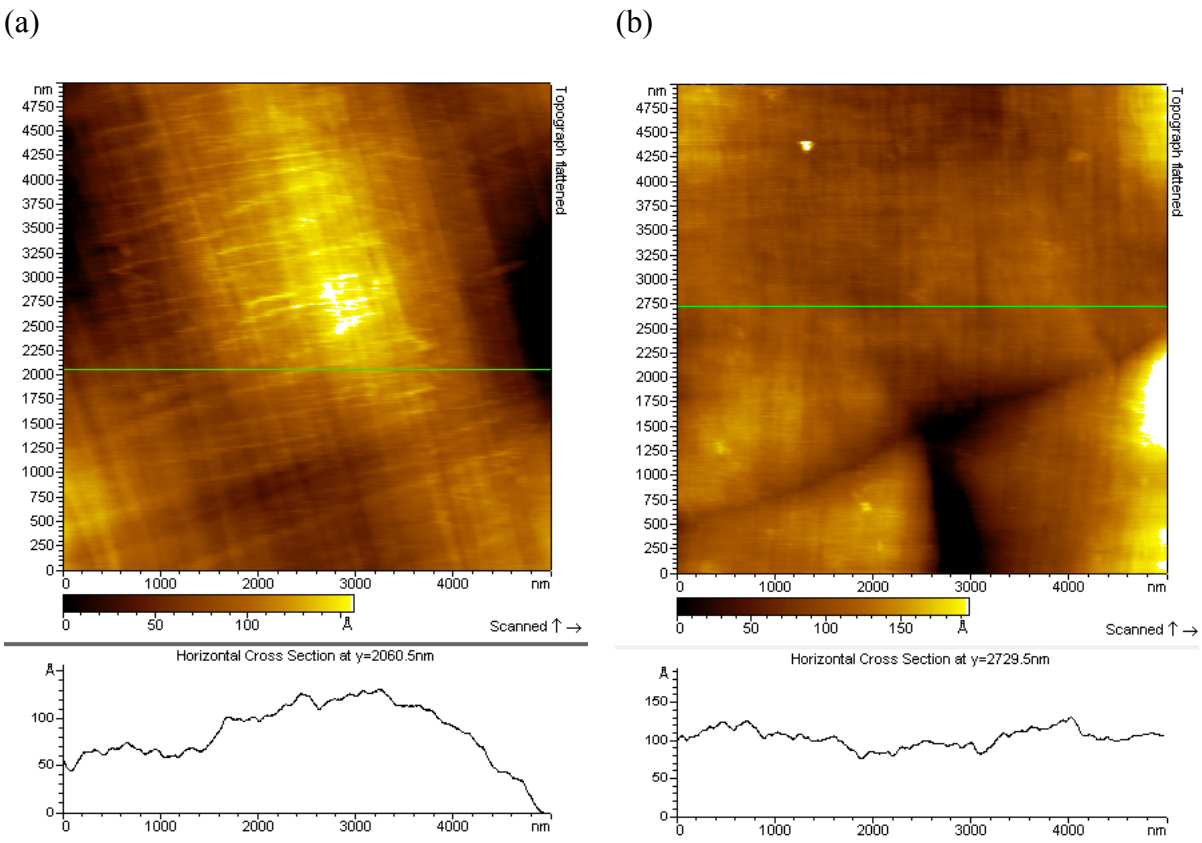


Figure 4.15: AFM images of the Ni{100}<001> substrate. (a) before (rms roughness = 19 nm) and (b) after etching (rms roughness = 357 nm).

Growth of Fe_3O_4 on air-formed NiO/Ni{100}<001>

Fe_3O_4 thin film was electrodeposited upon air-formed NiO/Ni{100}<001> substrate for 30 min. The average deposition rate was about 0.08 $nm \cdot s^{-1}$ based on final film thickness measurements. The XRD pattern of as-deposited film is shown in Figure 4.16, corresponding to a characteristic pattern of polycrystalline Fe_3O_4 where the (311) plane has the strongest reflection (JCPDS No. 19-0629), although the crystallographic structure of native nickel oxide must be examined for further ascertainment. No detectable peak for NiO was found in this case because the air-formed NiO is too thin (on the order of 2 nm, and so below the detector limit of the lab XRD). There is no observed crystallographic preferential orientation present for as-deposited Fe_3O_4 thin film despite the strong texture in the substrate material. AFM images (Figure 4.17) obtained in contact mode show the surface topography of air-formed NiO and as-deposited Fe_3O_4, respectively. The topography image of the air-formed NiO shows

that the surface is even, and the nickel oxide is homogeneously formed onto the nickel substrate. The Fe_3O_4 film displays a granular morphology and the surface is generally smooth with a root-mean-square (rms) roughness of 130 nm at a scan size of 5 μm x 5 μm; considerably smoother than before deposition. (Note that the rms value is 354 nm prior to electrodeposition; the high rsm value is due to grooves present in the nickel substrate)

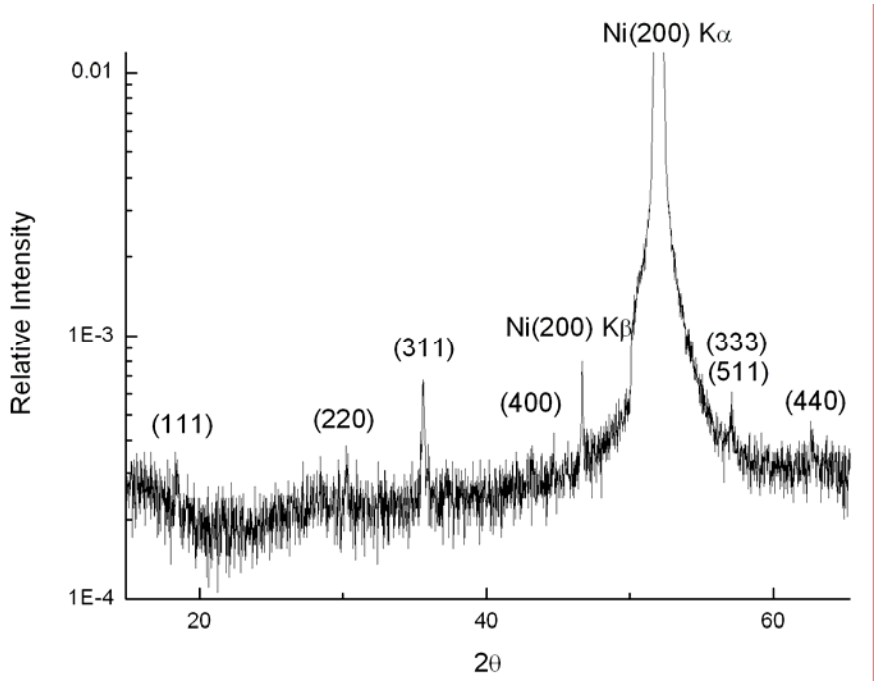


Figure 4.16: Bragg-Brentano scan of Fe_3O_4 thin film (~145 nm in thickness) deposited on air-formed nickel oxide on Ni{100}<001> substrate.

(a) (b)

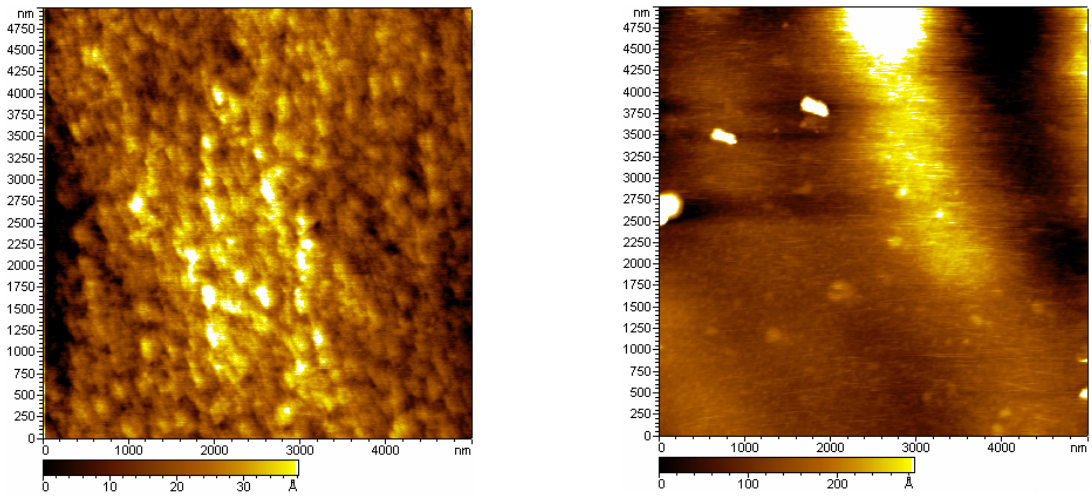
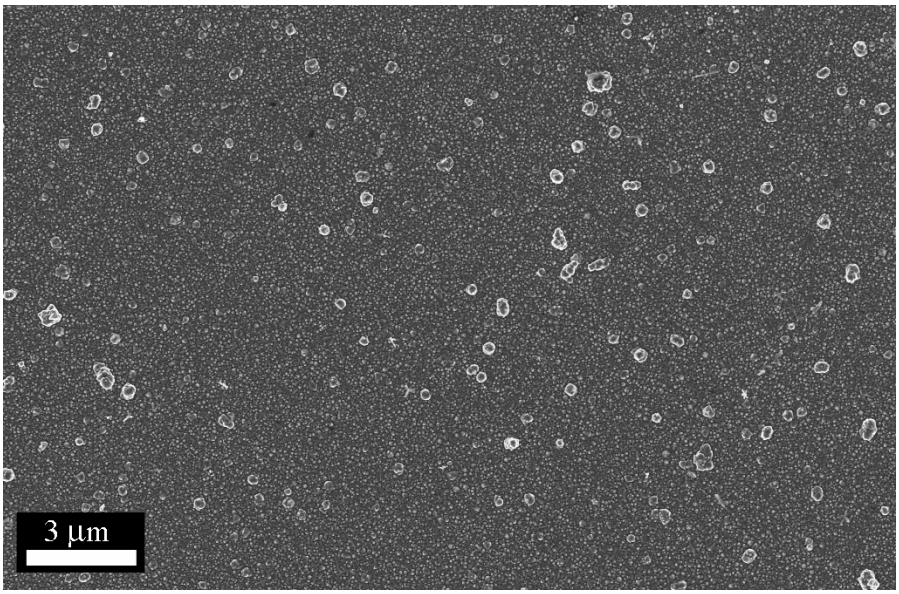


Figure 4.17: AFM images of Fe_3O_4 thin film show the detailed surface topography (a) before (rms roughness = 354 nm); (b) after (rms roughness = 132 nm).

The FEGSEM micrograph (Figure 4.18) reveals that the Fe_3O_4 film is grown continuously, and the grain size ranges from 50 nm to 200 nm. The formation of some surface clusters due to secondary nucleation on the growing Fe_3O_4 film is observed and the size of these clusters increases with deposition time. We found the size of these clusters increases with increasing time. EDS analysis (Table 4.2) indicate clusters have a similar composition with Fe_3O_4 film.

(a)



(b)

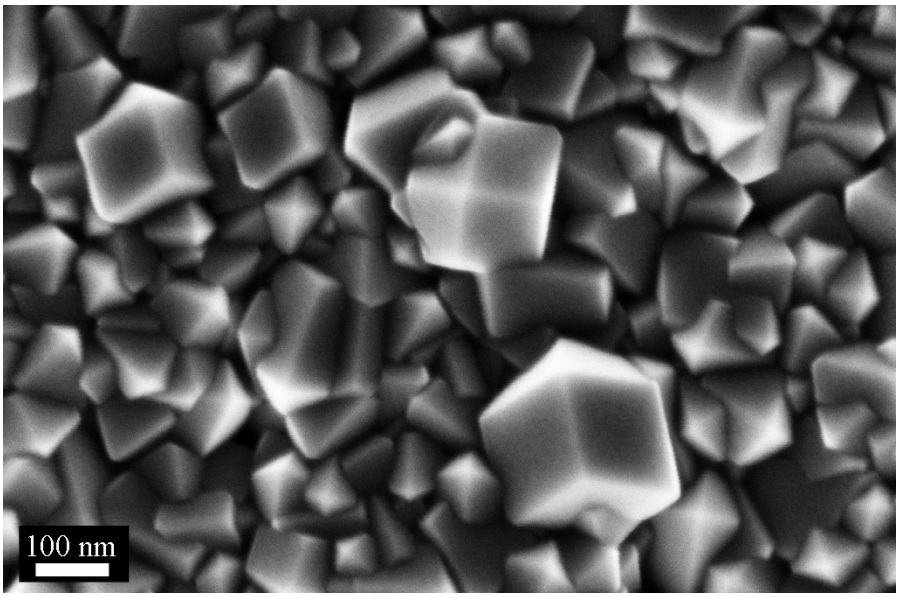


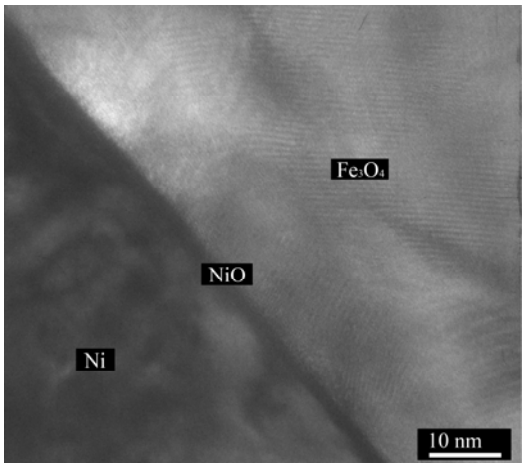
Figure 4.18: (a) FEGSEM micrograph of Fe_3O_4 thin film reveals film morphology; (b) magnetite cubic structure with different facets.

Spot area	Spectrum	O	Fe
Film	1	58.10	41.90
	2	57.77	42.23
	3	57.47	42.53
	4	58.16	41.84
	5	58.33	41.67
Cluster	1	58.74	41.26
	2	58.18	41.82
	3	58.32	41.68
	4	58.33	41.67
	5	57.95	42.05

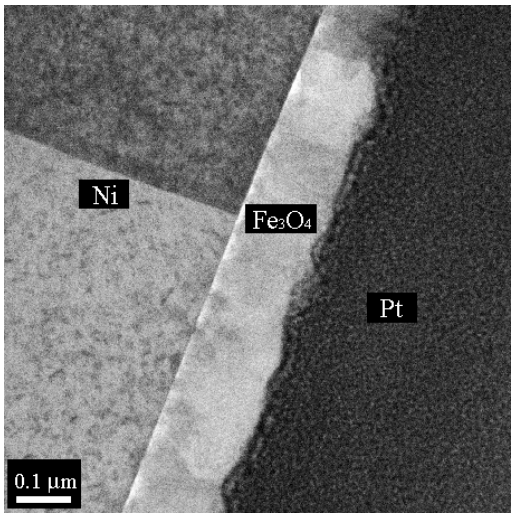
Table 4.2: EDS analysis of electrodeposited Fe_3O_4 (all results in atomic %)

In order to investigate the film homogeneity, scanning electron transmission microscopy (STEM) was employed. The Fe_3O_4 film grown on air-formed nickel oxide exhibits a columnar microstructure, which is also found at Fe_3O_4 films grown on conducting stainless-steel substrates [97]. The annular dark-field (ADF) STEM image (Figure 4.19c) reveals the Fe_3O_4 film has a uniform composition. In contrast the previous work on Fe_3O_4 grown on polycrystalline copper substrates, shows non-uniform composition on Fe_3O_4 films [100], with explicit phase contrast on ADF STEM image associated with averaged atomic configuration difference although it is given in low magnification. Therefore, it can be concluded that the film growth is clearly affected by grains or grain boundaries in the substrate materials.

(a)



(b)



(c)

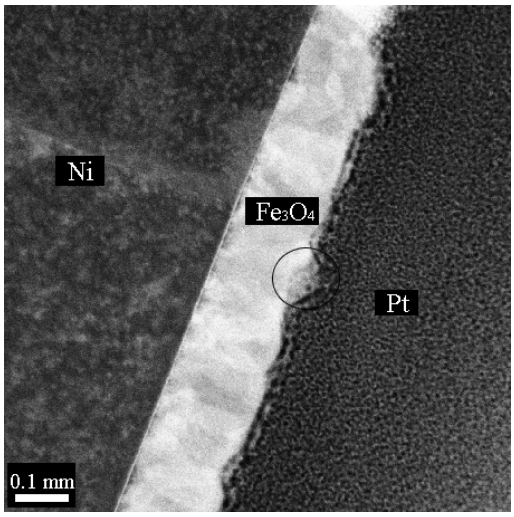


Figure 4.19: (a) HRTEM image shows thickness of air-formed NiO is about 2 nm; (b) bright-field image; (c) annular dark-field (ADF) STEM image. The circle indicates the cluster has a loose structure in comparison with Fe_3O_4 film.

Growth of multilayered Fe-based oxides

Polycrystalline tunneling barriers have been suggested theoretically [101] and realised experimentally [102] to yield higher tunneling spin polarization (TSP) or tunneling magnetoresistance due to the decay of certain wave function across the tunneling barrier. In our previous work, polycrystalline α-FeOOH thin films have been successfully grown onto polycrystalline copper foils at relatively low temperature [100]. Here the aim is to make the sandwich architecture of Fe_3O_4/α-FeOOH/Fe_3O_4 (Figure 4.20a) for spin-manipulating devices *via* an electrochemical route. As can be seen from the image in Figure 4.20b, the thickness of two ferromagnetic layers is around 200 nm; whereas there is no clear distinction between the Fe_3O_4 and α-FeOOH interface. The growth of Fe_3O_4 columnar structure is not continuous due to the presence of acicular α-FeOOH as shown in Figure 4.20b. Figure 4.20c displays the α-FeOOH conherently formed between two ferromagnetic Fe_3O_4 layers. The presence of α-FeOOH (JCPDS No. 29-0713) has been confirmed through synchrotron x-ray diffraction (Figure 4.21). Additionally, we find that there are no anti-phase domain boundaries present since the (220) or the odd index peaks are not broader than the (400), (440), *etc* (Figure 4.21c), and the lattice parameter of the Fe_3O_4 (a_0 = 0.8389 nm) is lower than that of bulk material (a_0 = 0.8396 nm). This value has a tendency to increase with increasing applied current density. The average value of three main diffraction peaks are 0.8384 nm, 0.8389 nm and 0.8389 nm for 0.005, 0.05 and 0.5 $mA \cdot cm^{-2}$ respectively, which suggests the lowest current density is a somewhat lower than the other two. There is also an unidentified peak observed in the XRD pattern at $2\theta = 27.4^o$. The peak does not match with standard XRD patterns of any iron oxides or hydroxides. A similar result was observed in the relevant literature [65] (although not explicitly commented upon by the authors).

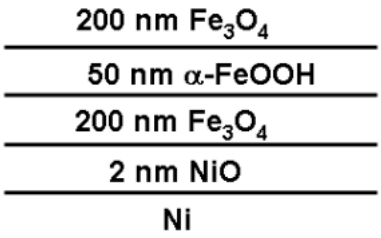
The growth mechanism of the first-layered Fe_3O_4 onto the NiO substrate is believed that the NiO substrate provides a hydrophilic surface where $FeOH^+$ ions can be adsorbed to form bonds on it. With an oxidizing-reagent such as $NaNO_2$, air or anodic current, some of Fe^{2+} ions are oxidized to Fe^{3+} ions. At the same time, the layer of ferrite without a preferred orientation forms on the substrate. The electrochemical reaction equation can be given as before.

$3Fe^{2+} + 4H_2O \rightarrow Fe_3O_4 + 8H^+ + 2e^-$

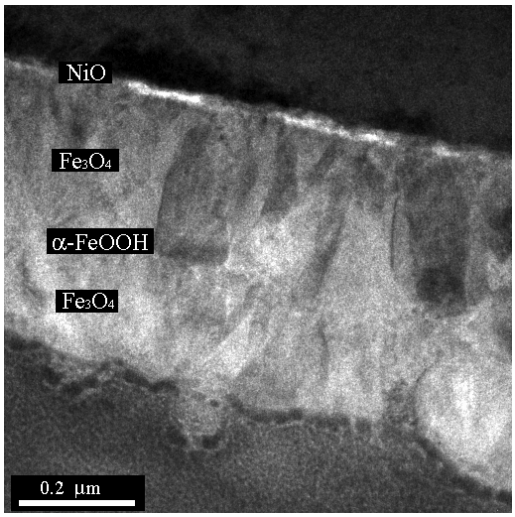
Since the new surface has OH groups, the deposition will continue as long as the Fe^{2+} ions and oxidizing reagent are present. Such this deposition process can be carried out at low temperature (< 100 ^oC) and there is no restriction on the substrate material. The deposition rate of second-layered α-FeOOH onto Fe_3O_4/NiO substrate is about 1 $nm \cdot s^{-1}$. The α-FeOOH film grown under this rate has a rough and loose microstructure. To approach smoother and condenser film surface it is necessary to decrease the deposition rate by lowering the applied anodic current. The understanding of the formation for third-layered Fe_3O_4 onto α-FeOOH is more complicated compared with that grown onto conducting materials. It is not solely an electrodeposition process because the band gap of α-FeOOH (E_g = 2.10 eV) is much higher than Fe_3O_4 (E_g = 0.1 eV) [18]. There might exist an electroless deposition of Fe_3O_4 to form a condenser layer onto the α-FeOOH/Fe_3O_4/NiO/Ni substrate, meaning that magnetite can be formed at very low overpotential.

In summary, the multilayered growth of Fe_3O_4/α-FeOOH/Fe_3O_4 on to air-formed NiO substrates has been successfully demonstrated by a successive deposition. Different growth mechanisms were proposed to clarify the formation of Fe_3O_4 on to air-formed NiO and α-FeOOH surfaces, respectively. The phase identification of iron oxides was performed by the synchrotron x-ray scattering technique, indicating there are no antiphase boundaries present either in Fe_3O_4 or α-FeOOH films.

(a)



(b)



(c)

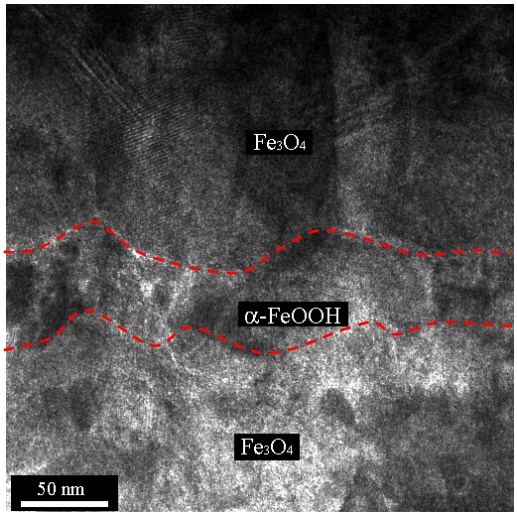
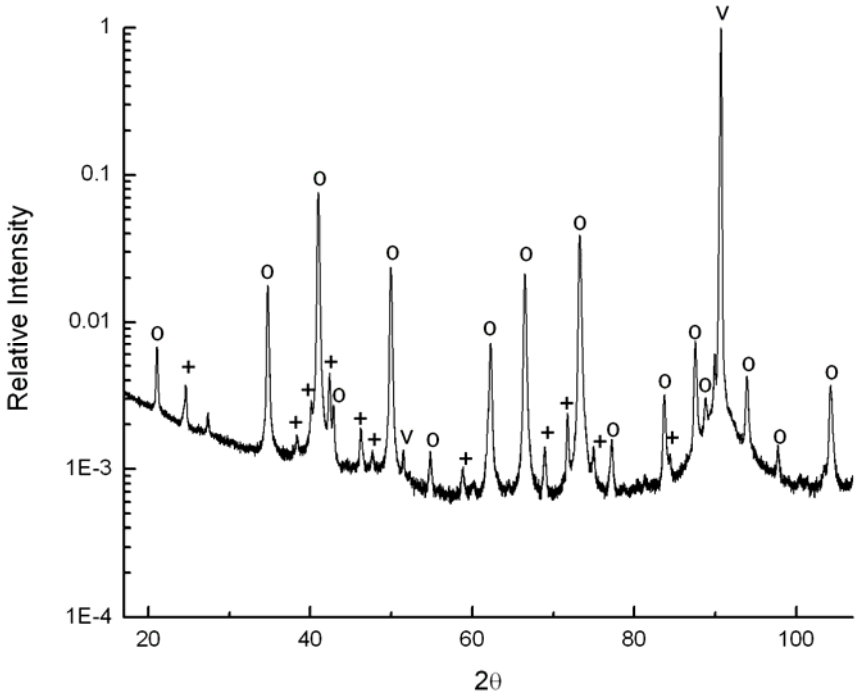


Figure 4.20: (a) A schematic illustration of Fe-oxide based spin manipulating device; (b) TEM micrographs of Fe_3O_4/α-FeOOH/Fe_3O_4 cross-section, showing two Fe_3O_4 layers separated by α-FeOOH; (c) loose α-FeOOH interlayer found grown on Fe_3O_4. (red dashed line represents the interface between Fe_3O_4 and α-FeOOH)

(a)



(b)

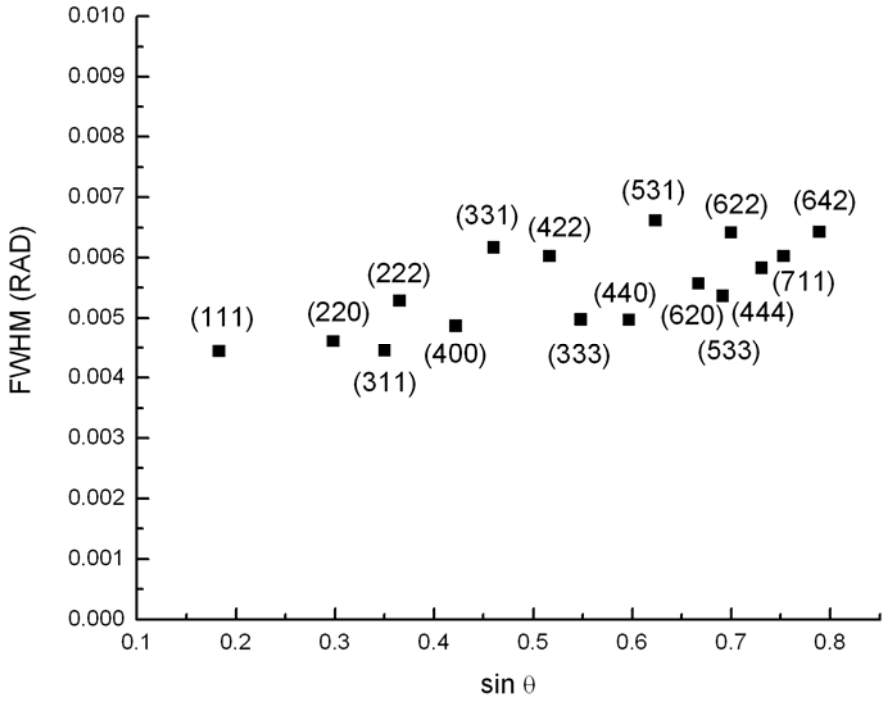


Figure 4.21: (a) Synchrotron x-ray scattering spectrum under an accelerating voltage of 7001.5 eV. The symbols "o", "+"and "v" represent Fe_3O_4, α-FeOOH and Ni. (b) a plot of FWHM *vs.* sin θ for Fe_3O_4 showing there is not apparent anti-phase boundary present. The average crystal size is 35 nm.

4.4 Influence of buffer concentrations on structure, film morphology and magnetic properties

In this section, the influences of the solution chemistry on crystal structure and film morphology were investigated by adding different amount of buffer *i.e.* CH_3COOK. The Fe_3O_4 films were grown on to Au/glass substrates at 80 ^oC with an applied potential of 25 mV *vs.* Au electrode. The deposition time was 1800 s. The initial pH value for different concentrations of CH_3COOK was recorded before electrodeposition. (Figure 4.22) This value is not constant, and decreases with increasing deposition time due to the production of H^+ ions from electrochemical reactions [41].

Figure 4.23 shows XRD spectra of Fe_3O_4 films grown at different concentrations of CH_3COOK. All diffraction intensities were plotted on logarithmic scale. As seen, the XRD spectra match with the standard powder pattern of Fe_3O_4 (JCPDS No. 19-0629), with high crystallinity. Sorenson *et al*. reported that Fe_3O_4 grown onto single crystal Au(111) has a [111] and [511] orientation [65]. However, no texture was found under the growth conditions although the gold/glass substrate has a highly preferred orientation on the (111) direction (Table 4.3).

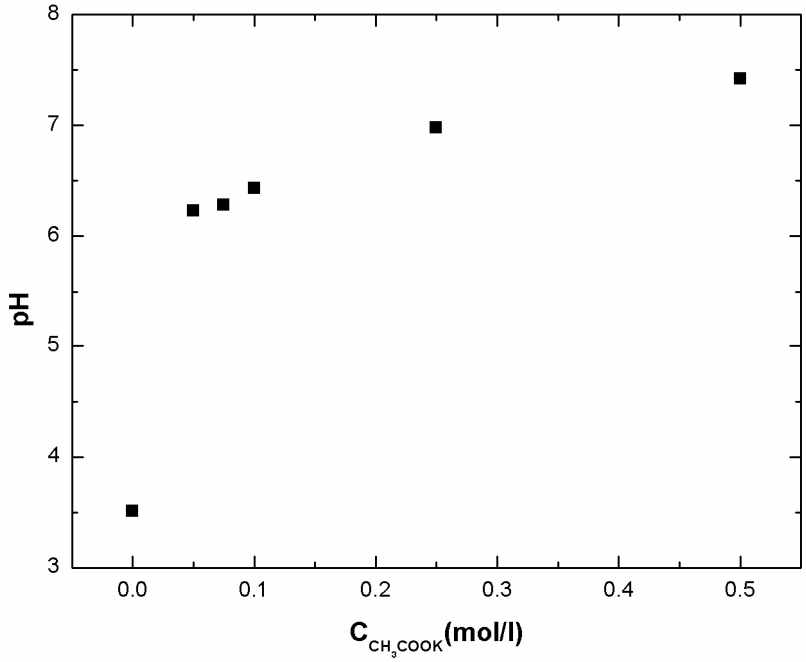


Figure 4.22: pH measurement for electrolytes containing 0.01M $(NH_4)_2Fe(SO_4)_2{\cdot}6H_2O$ at different concentrations of CH_3COOK.

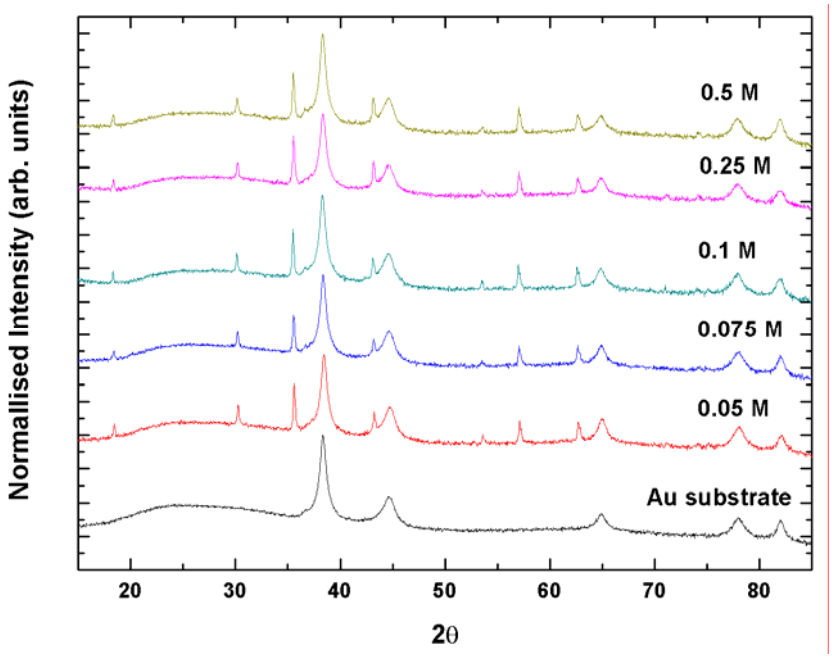


Figure 4.23: X-ray diffraction patterns of Fe_3O_4 films grown at different concentrations of CH_3COOK at 25 mV *vs.* Au electrode.

Plane (hkl)	Fe_3O_4 (Standard)	0.05 M	0.075 M	0.1 M	0.25 M	0.5 M
1 1 1	8.00	11.20	8.08	8.21	7.16	11.00
2 2 0	30.00	28.37	31.72	25.30	19.29	21.55
3 1 1	100.00	100.00	100.00	100.00	100.00	100.00
2 2 2	8.00	*	*	*	*	*
4 0 0	20.00	25.08	25.74	22.17	29.83	31.53
4 2 2	10.00	5.78	4.55	5.14	3.40	-
5 1 1	30.00	18.46	20.41	20.04	19.91	21.27
4 4 0	40.00	14.63	22.06	15.20	12.34	12.84
5 3 1	2.00	*	*	*	*	*
6 2 0	4.00	-	-	-	-	-
5 3 3	10.00	-	-	-	-	-
6 2 2	4.00	-	-	-	-	-
4 4 4	2.00	*	*	*	*	*

Table 4.3: Comparison of relative intensity between standard Fe_3O_4 (JCPSD No. 19-0629) and electrodeposited Fe_3O_4 film grown at different concentrations of CH_3COOK. ("*" and "-" represent the overlap and no-detectable peak, respectively)

The average particle size of Fe_3O_4 has a tendency to increase with increasing concentration of CH_3COOK, from 45 nm (0.05 M) to 51 nm (0.1 M). However, further increase of CH_3COOK leads particle size to decrease (Figure 4.24). This is attributed to the higher pH value; more $FeOH^+$ ions are produced *via* a hydration process [92], and then react with molecular oxygen. As a result, less $FeOH^+$ ions can be absorbed onto the gold/glass substrate and grow the crystallites. The lattice constant is about 0.8392±0.0001 nm, which is less than the bulk value of Fe_3O_4 (0.8396 nm). Additionally, there is no significant dependence of lattice constant with concentration of CH_3COOK. A similar surface morphology was found for the Fe_3O_4 films grown at different concentrations of CH_3COOK (Figure 4.24). The grain size ranges from a few 10 nm to 100 nm, and is not a function of concentration of CH_3COOK. Clusters due to anomalous nucleation still occur and become more prominent at higher concentrations.

In this section, the influence of the buffer (CH_3COOK) was studied. The XRD spectra showed no significant change in lattice constant, but the particle size showed a strong dependence on CH_3COOK concentration. Additionally, the Fe_3O_4 films had no crystallographically preferred orientation.

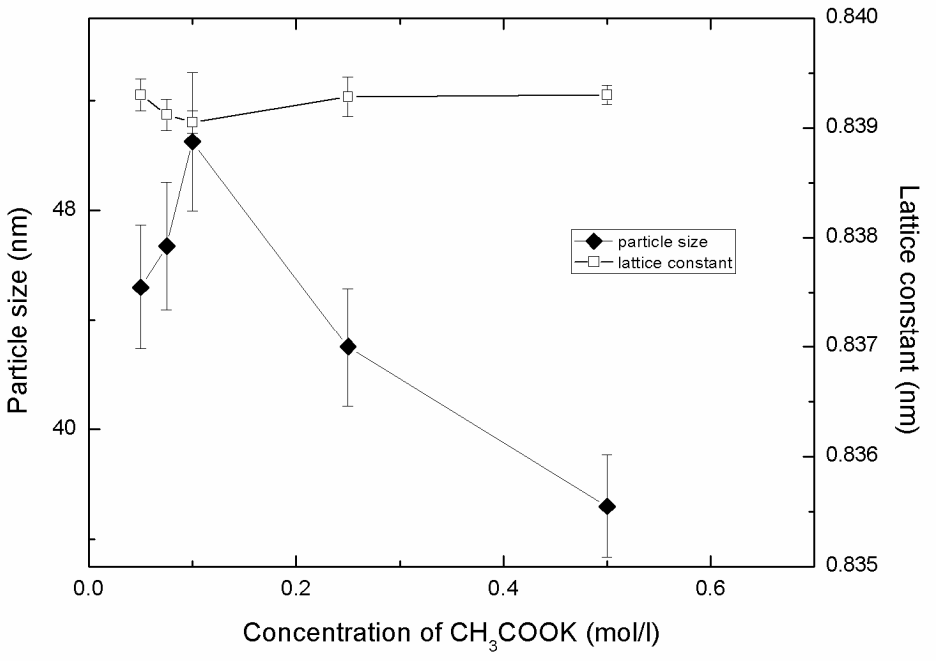


Figure 4.24: Average particle size and lattice constant of Fe_3O_4 grown at different concentrations of CH_3COOK.

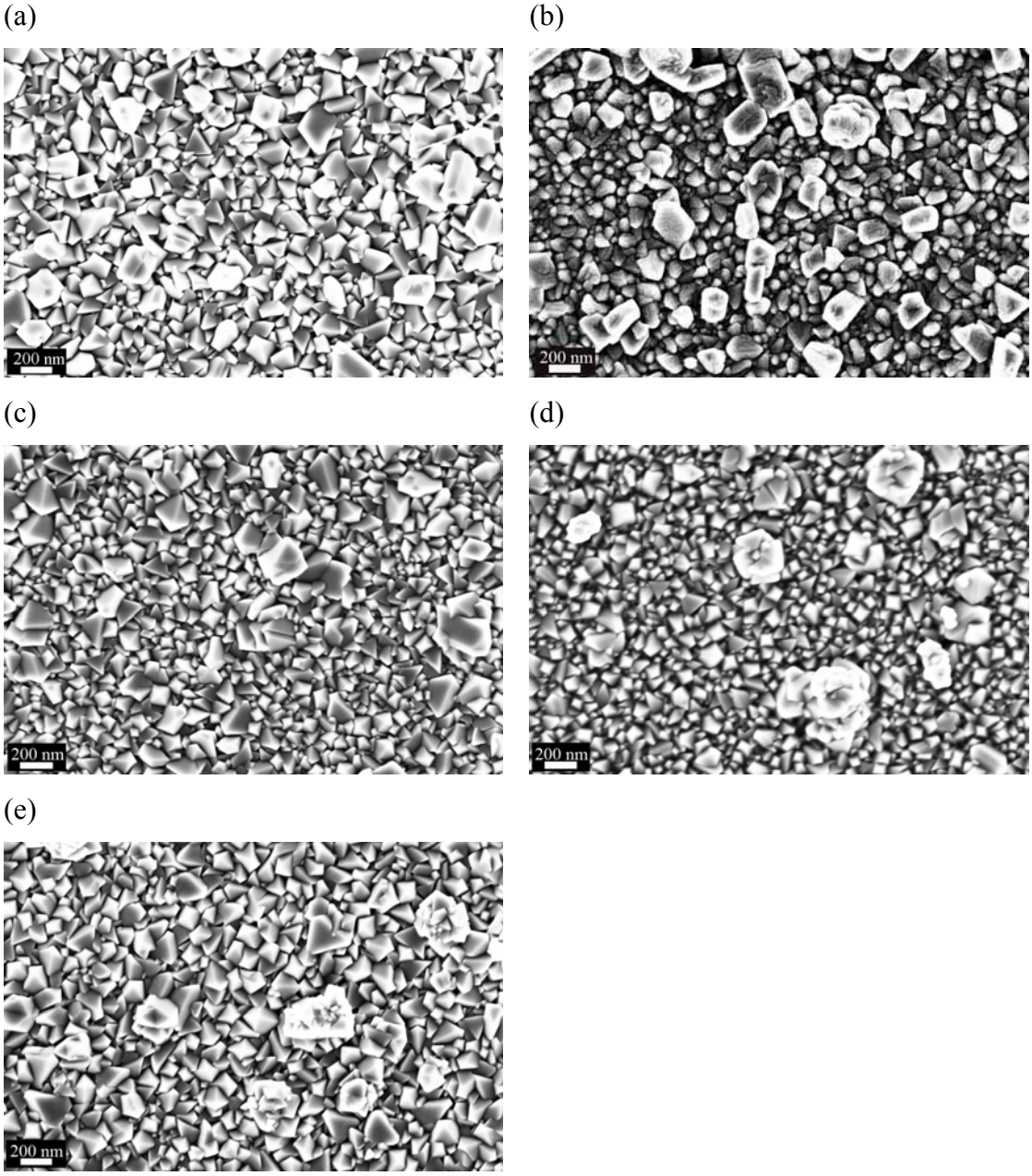


Figure 4.25: FEGSEM micrographs of Fe_3O_4 films grown at different concentrations of CH_3COOK: (a) 0.05 M; (b) 0.075 M; (c) 0.1 M; (d) 0.25 M; (e) 0.5 M.

4.5 Influence of deposition potential on structure, film morphology and magnetic properties

Copper foils and Cu (50 nm)/Si(001) substrates were used to investigate the influence of potential on structure, film morphology and magnetic properties. To study this, the electrolyte was prepared with 0.01 $mol \cdot l^{-1}$ ferrous ammonium sulphate ($(NH)_4 Fe(SO_4)_2 \cdot 6H_2O$) and 0.05 $mol \cdot l^{-1}$ potassium acetate (CH_3COOK). The bath temperature was kept at 80 ^oC and was purged with argon with vigorous stirring at least an hour prior to and during electrodeposition. The deposition time was 30 minutes.

Structure of Iron Oxide Thin Films

Phase identification was performed by x-ray diffraction (XRD) as described in the previous section. Figure 4.26 shows the XRD patterns of iron oxide thin films electrodeposited on copper foils at various potentials *vs.* an Au pseudo-reference electrode [~-210 mV *vs.* NHE]. In the low potential regime (10, 25, 50 and 100 mV) all of the XRD spectra are identical with a polycrystalline characteristic of Fe_3O_4 (JCPDS No. 19-0629), in which the iron oxides grown under these conditions are well-crystallized and there is no apparently preferred orientation present. The spectra are different from that of γ-Fe_2O_3 (JCPDS No. 39-1346) because peaks at 14.96^o, 23.77^o and 26.1^o, corresponding to (110), (210) and (211) planes are absent (see Appendix A-5). In the case of the sample prepared at 50 mV the diffraction pattern of the film remains consistent with Fe_3O_4-single phase after vacuum anneal at 400 ^oC for 5 min. To obtain the lattice constant (a_0) for iron oxide films, a plot is drawn with $\cos^2\theta/\sin\theta$ on the x-axis and a_0 on y-axis, and the linear fitting curve was extrapolated to θ to 90^o for an accurate value. The lattice constant of as-deposited Fe_3O_4 thin film is about 0.8392±0.0001 nm (Figure 4.27), which is slightly less than that reported for bulk material (0.8396 nm) [13]. For the annealed sample, the value is slightly larger at about 0.8408 nm.

The particle size (d) and lattice strain (ε) can be calculated by using Williamson-Hall approach as below [83].

$$B_{\exp} = \frac{0.9\lambda}{d\cos\theta} + 4\varepsilon\frac{\sin\theta}{\cos\theta}$$

where B_{exp} is the experimental peak broadening. It is the difference between observed peak broadening (B_{obs}) and instrumental broadening (B_{inst}). Accordingly, the total contribution of peak broadening is due to the effect of finite crystal size and lattice strain. By plotting B_{exp} cos θ on the y-axis and 4sin θ on the x-axis, the particle size can be obtained by the y-intercept and the lattice strain from the slope after linear fitting. Figure 4.28 shows the average particle size and strain of Fe_3O_4 grown at various applied potentials. An approximate calculation is found: the particle sizes are 32 nm, 44 nm, 59 nm and 71 nm, for 10 mV, 25 mV, 50 mV and 100 mV, respectively. The values of the lattice strain for all the samples are very small, less than 0.05%. It seems there is a dependence of increasing crystallite size with increasing applied potential. For the annealed sample (50 mV) there is apparent increase in strain from 0.018% to 0.062%. The result is consistent with the previous calculation of lattice constant.

As the potential is increased to 200 mV *vs.* Au electrode, the phase changes and the diffraction peaks of α-FeOOH (JCPDS No. 29-0713) appear, meaning more Fe^{2+} ions in the electrolyte were oxidised. The corresponding XRD spectrum shows that the peak intensities of (002) and (111) have a considerable increase with respect to the standard JCPDS pattern, indicating some texture in the deposit. From a consideration of the thermodynamics, the oxidation reaction and equilibrium potential at 25 ^{o}C have been suggested as below [103]:

$Fe^{2+} + 2H_2O = \alpha\text{-}FeOOH + 3H^+ + e^-$

$E = 0.89 - 0.1773\ pH - 0.0591\ \log [Fe^{2+}]$

With further increase of the potential to 400 mV, a mixture of phases with goethite (α-FeOOH) and lepidocrocite (γ-FeOOH, JCPDS No. 44-1415) are present in the film. As can been seen in Figure 4.26, γ-FeOOH is the dominant phase and exhibits a strong (101) and (002) crystallographic preferred orientation, whereas α-FeOOH exhibits no crystallographic preferred orientation. The formation of γ-FeOOH takes place *via* the following oxidation reaction [103]:

$Fe^{2+} + 2H_2O = \gamma\text{-FeOOH} + 3H^+ + e^-$

and its equilibrium potential at 25 ^oC can be estimated by

$E = 0.99 - 0.1773\ pH - 0.0591 \log [Fe^{2+}]$

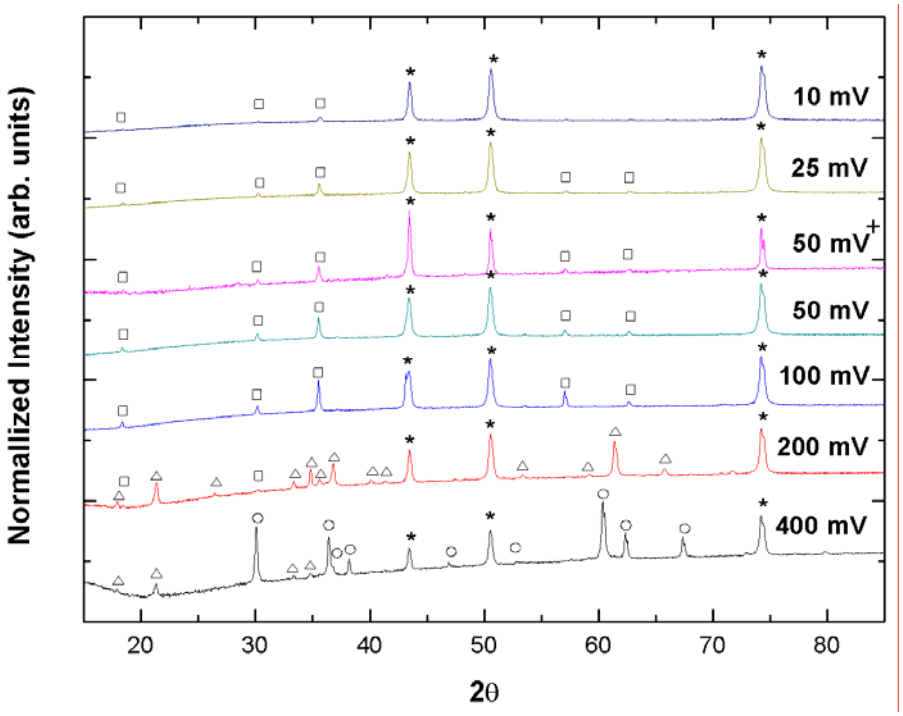


Figure 4.26: XRD patterns of iron oxide thin films on copper foils at various potential *vs.* Au reference electrode. (The symbols "*", "□", "Δ", and "○" represent Cu, Fe_3O_4, α-FeOOH and γ-FeOOH, respectively. The symbol "+" indicates that the sample is annealed at 400 ^oC under vacuum for 5 mins)

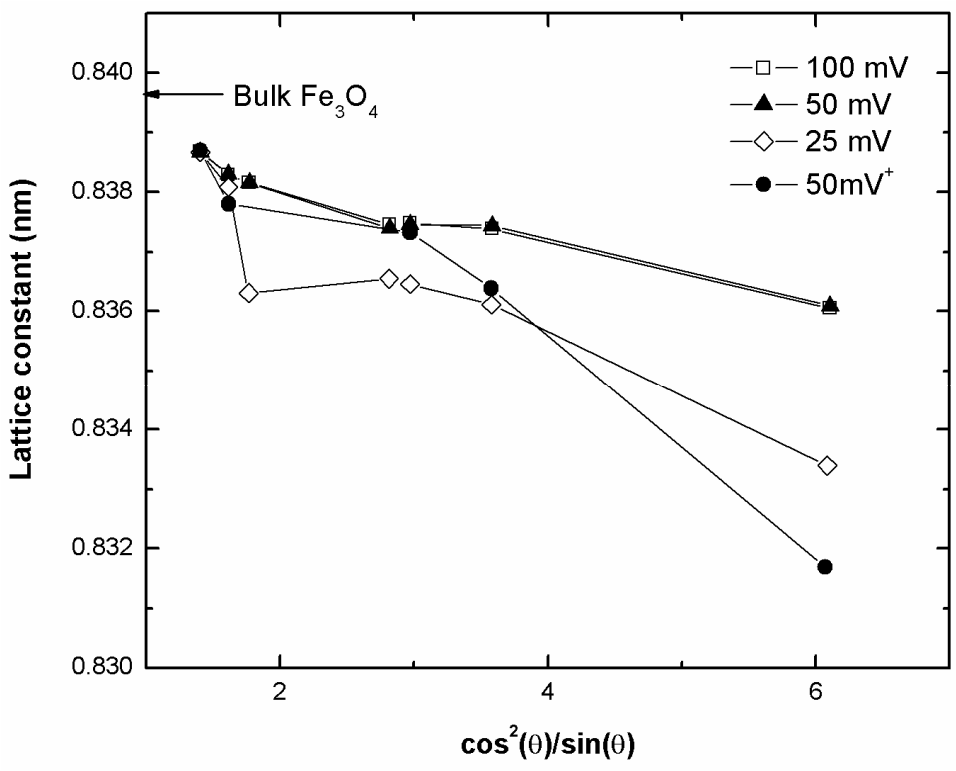


Figure 4.27: Plot of lattice constant as function of θ for Fe-oxide films deposited at different applied *E*, Extrapolation to 90^o provides accurate calculation of a_0. (The symbol "+" indicates that the sample is annealed at 400 ^{o}C under vacuum)

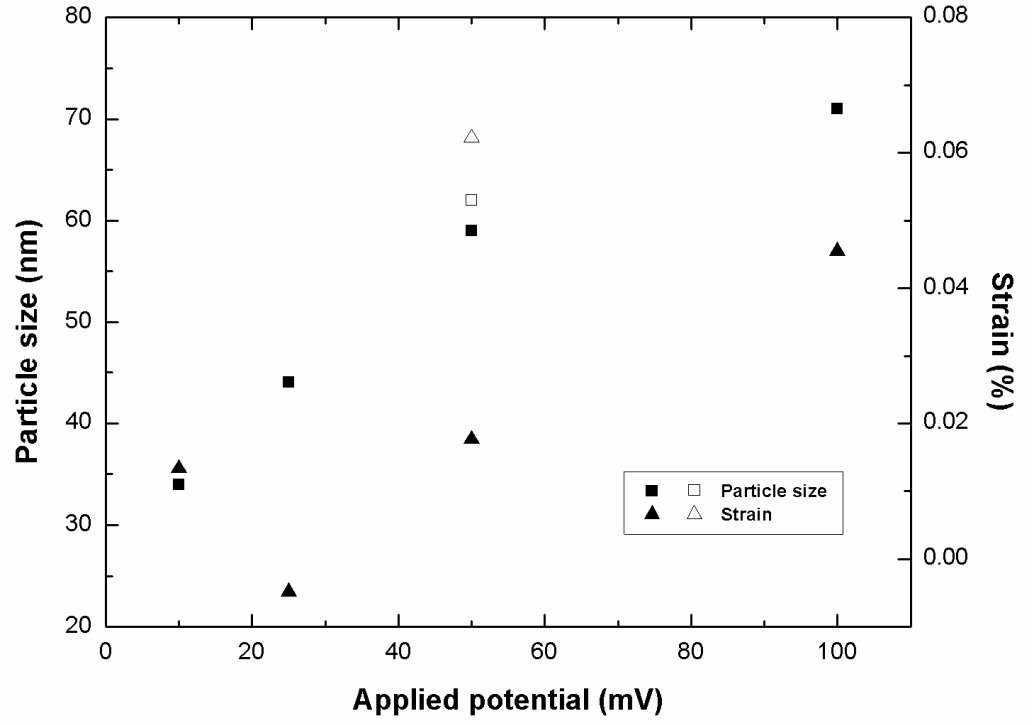


Figure 4.28: Average particle size and strain of Fe_3O_4 grown at different applied potentials calculated *via* Williamson-Hall approach. (open symbols at 50 mV indicate that the sample was annealed)

Morphological study of Iron Oxide Thin Films

Here, iron oxide thin films electrochemically deposited at a range of potentials between -5 mV to +400 mV *vs.* gold reference electrode on to copper foils and Cu/Si substrates have been examined by field-emission-gun scanning electron microscope (FEGSEM), in which the accelerating voltage and working distance were set to 3 keV and 5 mm, respectively, and secondary electron (SE) signals were received by a coaxial in-lens detector.

Figure 4.29 shows the FEGSEM micrographs of the iron oxide thin films grown on copper foils at different applied potentials. At E = +400 mV (Figure 4.29a), the γ-FeOOH shows a porous and lath-like or tabular microstructure where the all the grains are formed normal to the substrate surface. A similar structure has been reported in the some literature articles [104, 105]. The microstructure drastically changes as the potential is decreased to 200 mV. The bipyramidal goethite crystals were observed [18]. This is because the formation of α-FeOOH is preferred over γ-FeOOH at this potential. The formation of the polydomainc α-FeOOH is due to the high ionic strength of sulphate ions which retard the nucleation and growth of certain planes [106]. The film structure becomes more compact at a potential of +100 mV and grain size ranges from 100 to 500 nm. At the oxide films grown at 50, 25 and 10 mV (Figure 4.29d-f), the grain has either an octahedral or rhombic shape because the grain growth has a tendency to minimize surface energy. This has been discussed in Section 4.2. Additionally, the grain has a sharp edge, and its size decreases with decreasing potential. The film is not fully covered onto the copper foil at the case of 10 mV. It is attributed to lower potential which does not have enough driving force to form sufficient oxide nuclei onto copper foils. Moreover, few grains with an acicular-shape are observed as arrowed in Figure (4.29f). It is a formation of the iron oxyhydroxide (α-FeOOH). The observation is in line with synchrotron x-ray scattering results in the previous section. At lower applied potential of 5 mV, the surface morphology is different from the films grown at higher potentials. The film surface mainly consists of different forms of iron oxides, such as layered, acicular and particle-like structure as shown in Figure 4.29g. With a negative potential of -5 mV applied on the working electrodes it seems it is not possible to form the desired Fe_3O_4 phase (Figure 4.29h) although the theoretical calculation and cyclic voltammogram (Figure 4.1b) suggests

that a small negative potential could produce Fe_3O_4.

Identical process parameters are used for electrodeposition on Cu/Si substrates (Figure 4.30). The surface morphology of the iron oxides films has a similar feature with those grown onto copper foils (Figure 4.29). Compared with Figure 4.29b and 4.30b, the crystallographic nature of the iron oxide film grown onto the copper foil is less well-defined. Additionally, it is worth noticing that the iron oxide films grown at a low potential regime (25 mV and 10 mV) onto the Cu/Si substrates have distinct triangular grain and better orientation. This is because the Fe_3O_4(111) grows epitaxially on to Cu(111)/Si(001).

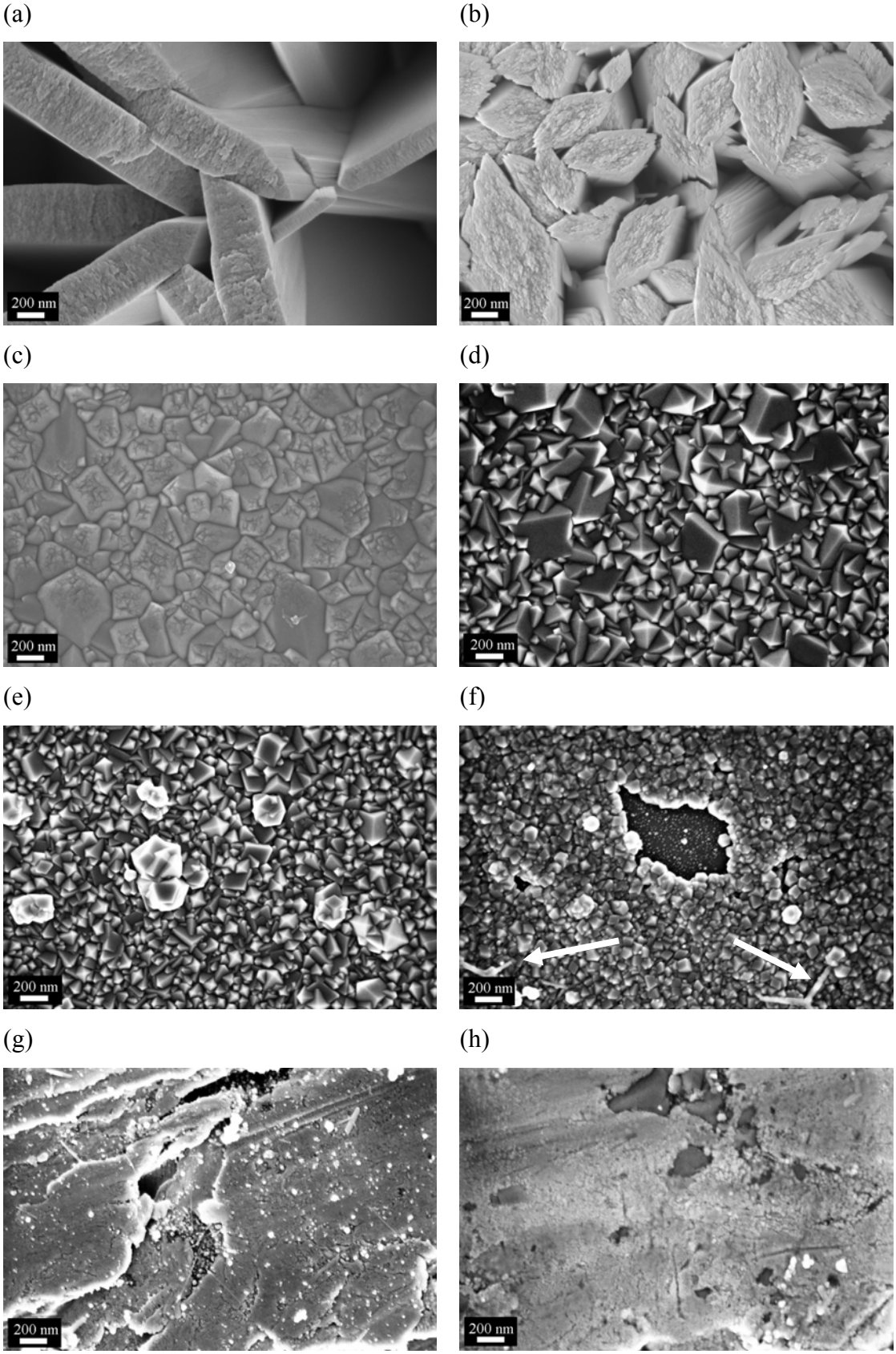


Figure 4.29: FEGSEM micrographs of iron oxide thin films on copper foils at various potential *vs.* Au reference electrode. (a) 400 mV; (b) 200 mV; (c) 100 mV; (d) 50 mV; (e) 25 mV; (f) 10 mV; (g) 5 mV; (h) -5 mV.

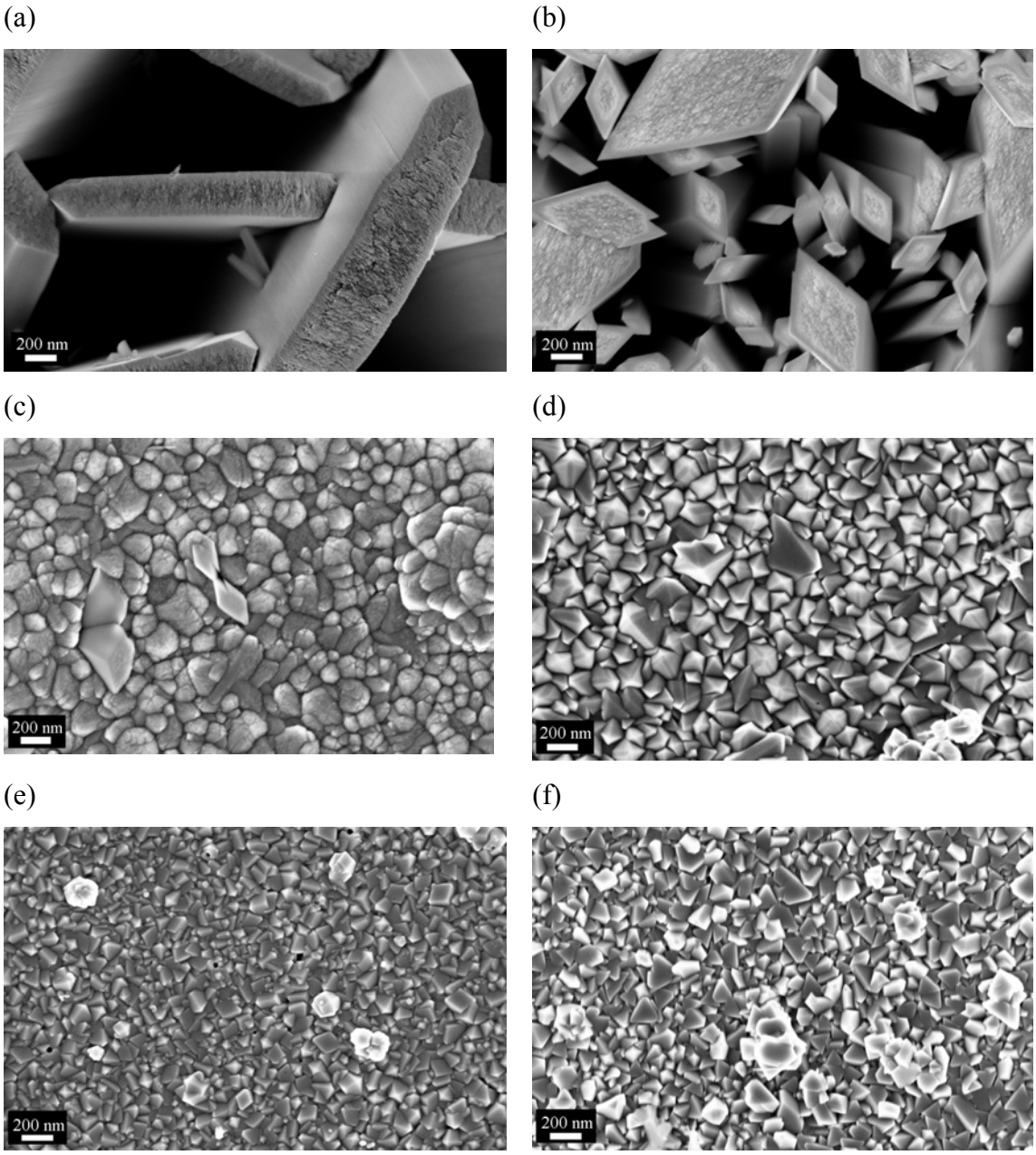


Figure 4.30: FEGSEM micrographs of iron oxide thin films on Cu/Si substrates. (a) 400 mV; (b) 200 mV; (c) 100 mV; (d) 50 mV: (e) 25 mV; (f) 10 mV.

X-ray Absorption Near Edge Structure (XANES)

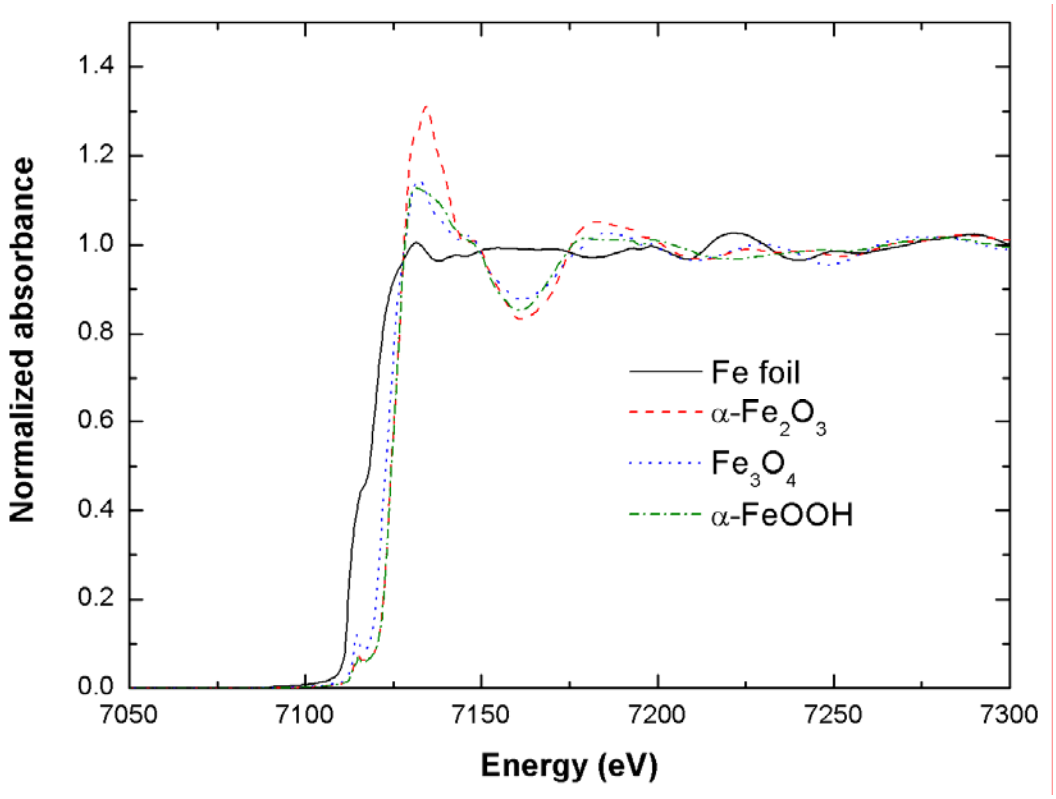
Fe x-ray *K*-edge absorption spectra were collected at Beamline 10-2 at SSRL. The experimental details were described in the previous section. The energy scale was calibrated by measuring the spectrum from an iron foil. The absorption peak position is 7112.1 eV, obtained by taking the peak in the first derivative of this spectrum. The energy resolution is ~0.4 eV in the scan energy range. However, this value is affected intrinsically by the core-hole life-time broadening of Fe *K* shell [107]. The energy resolution is about 1.2 eV if the core-hole width is taken into account. All of the spectra were normalized and processed by using AUTOBK program for background removal [108].

Several types of iron oxides or oxyhydroxides: Fe_3O_4 (99.999%), α-Fe_2O_3 (99%) and α-FeOOH (99%), all purchased from Sigma-Aldrich, Inc. were used as references. X-ray absorption spectra of the standard samples (including an iron foil) measured in transmission geometry are shown in Figure 4.31. As can be seen in Figure 4.31a, the XANES spectra show distinct differences between the standard samples, where iron oxides and oxyhydroxides exhibit apparent pre-edge feature whereas the Fe spectra gives a broadened shoulder. Generally, variation in absorption intensity of edge features is ascribed to the coordination change for electronic dipole transition from the 1*s* to higher *d* orbital [109]. Moreover, the edge position (energy) shift is associated with valence change due to the change of binding energy (electrostatic force) of the electron at 1*s* core shell [110]. Variation of coordination number does not affect the edge position since the change of bonding length is not significant enough to influence the effective charge of metal ions [111]. Comparison of the pre-edge features (Figure 4.31b) reveals that Fe_3O_4 has a slight energy shift toward low photon energy owing to low oxidation state with respect to α-Fe_2O_3 and α-FeOOH [112, 113]. For α-Fe_2O_3 and α-FeOOH, the pre-edge is a doublet, attributed to the transitions of $1s \rightarrow t_{2g}$ and $1s \rightarrow e_g$. It is because the x-ray absorption in the energy range contains all of Fe ions from octahedral sites [114]. The characteristic pre-edge peak of Fe_3O_4 arises from the 1*s* to 3*d* transition, mainly dominated by Fe^{3+} ions at tetrahedral sites with the mixing of 3*d* and 4*p* states [115].

The single pre-edge peak in Fe_3O_4 is associated with less crystal field splitting between *e* and t_2 states in tetrahedral sites [15].

Figure 4.32 shows the comparison of Fe *K*-edge absorption between electrodeposited iron oxides films and the standard samples. All of these spectra have a similar absorption feature in the XANES region. (Figure 4.32a) However, pre-edge features of these iron oxides/oxyhydroxides are different. (Figure 4.32b) The results imply that the electrodeposited iron oxide films grown at the range of 25~100 mV *vs.* Au electrode possess close oxidation state with the standard Fe_3O_4 power sample. The actual oxidation state was not obtained although it is theoretically possible to use the peak shift to quantitatively calculate amount of Fe^{2+} and Fe^{3+} ions in Fe_3O_4. The separation of two absorption peaks at Fe^{2+} and Fe^{3+} is only 1.4 eV [116], and this is the same order of magnitude as the experimental energy resolution. Additionally, the pre-edge intensity of as-deposited iron oxide films is somewhat smaller than that of standard Fe_3O_4 power sample. Since the pre-edge feature is solely originated from Fe^{3+} ions in the tetrahedral (A) sites [115], the reduction of intensity can be associated with less tetrahedral Fe^{3+} ions in the as-deposited films, and smaller value was found for the film grown at 25 mV *vs.* Au electrode. For the annealed sample prepared at 50 mV, the Fe *K*-edge absorption spectrum is identical to that of the sample without annealing, meaning there is no alteration on crystallographic structure after the post-treatment process.

(a)



(b)

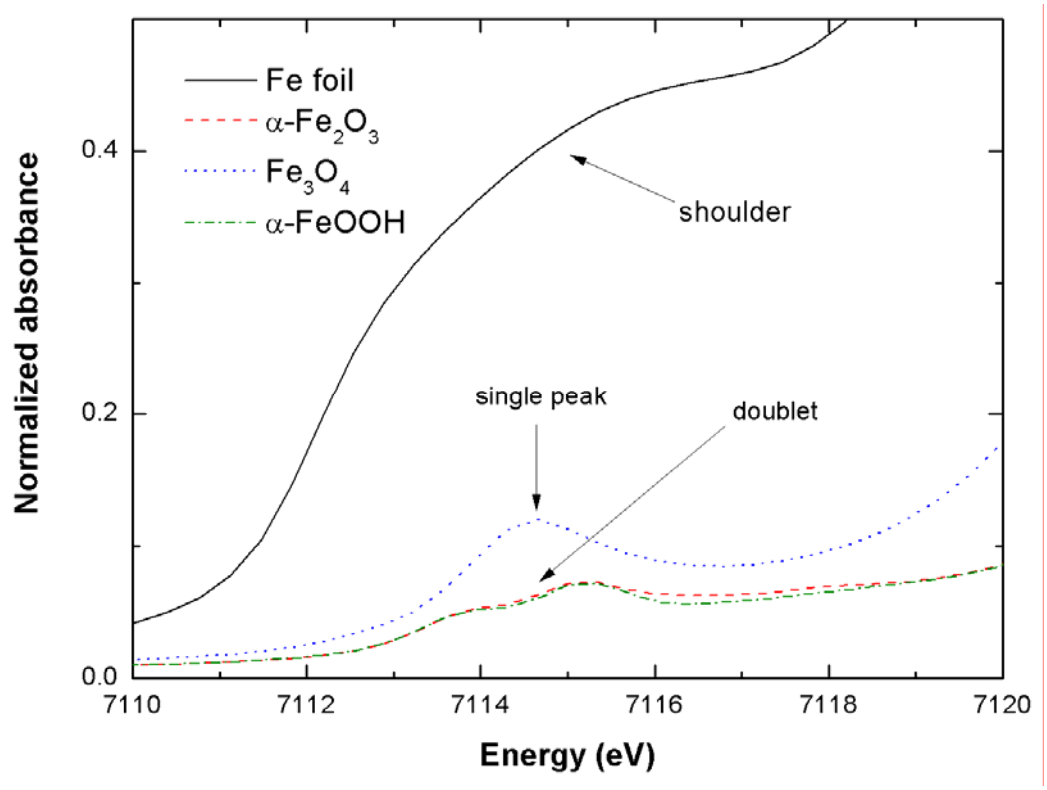
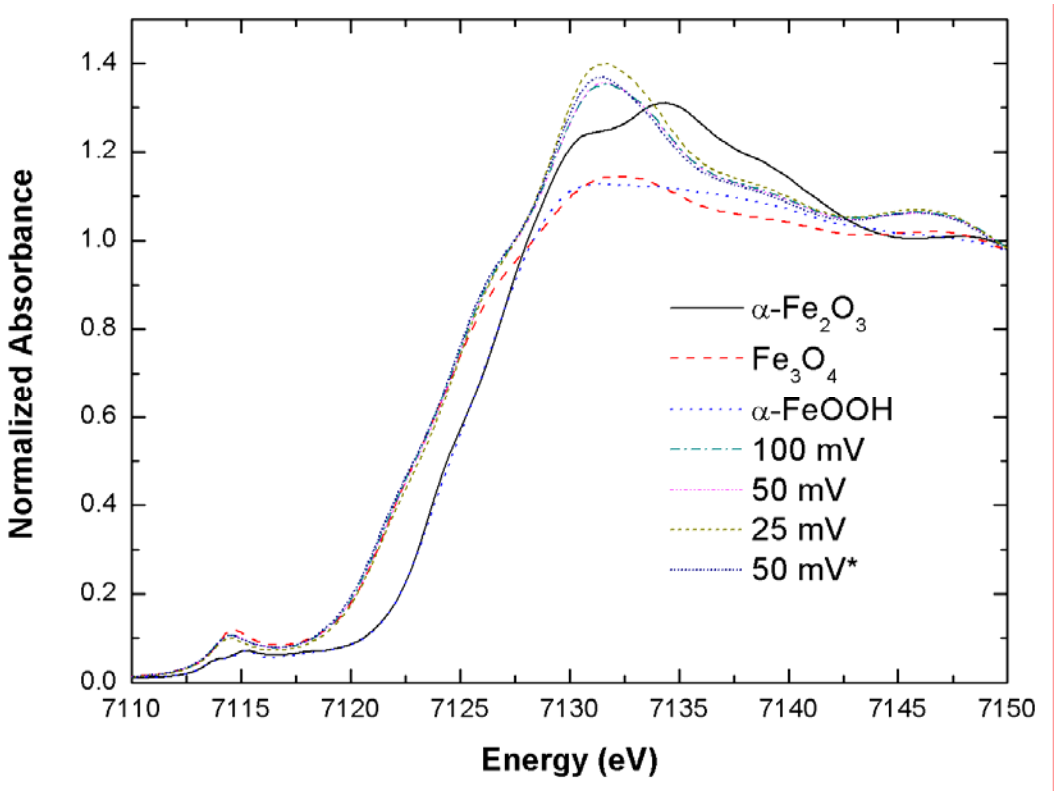


Figure 4.31: (a) Normalized Fe *K*-edge x-ray absorption spectra of the standard samples; (b) details of pre-edge features in (a).

(a)



(b)

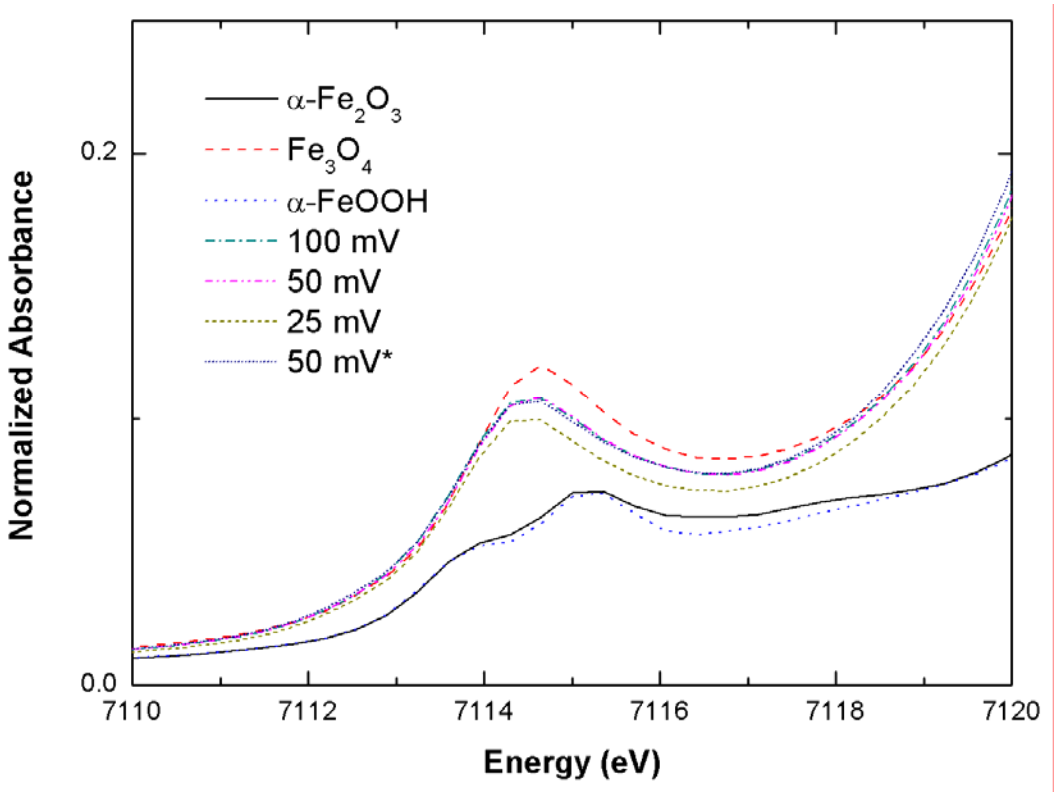


Figure 4.32: (a) Fe *K*-edge x-ray absorption spectra of the iron oxides compared with the standard samples; (b) details of pre-edge features in (a).

Fe $L_{2,3}$-edge magnetic circular dichroism

Iron oxide thin films grown electrochemically onto copper foils were examined using magnetic circular dichroism (XMCD) in soft x-ray absorption spectroscope (XAS). The samples were mounted on to conductive carbon tape and put in an ultra-high vacuum chamber (~10^{-10} torr). The XAS spectra of Fe_3O_4 thin films were taken in the total electron yield (TEY) mode with a bias of +100 volts applied on to the sample holder to gather more electronic signals during measurements. The photon-energy resolution of ~0.4 eV in the scan range of 695-735 eV, and the incident angle is 90^o with respect to the sample surface. The probing depth is about 5 nm or more and is considered equivalent to the bulk analysis [117]. Typically, the raw XAS spectra are composed of a linear function and an arctangent-like edge-jump function. Figure 4.33 shows XAS spectra of iron oxides grown at different potentials (100 mV, 50 mV and 25 mV *vs*. Au reference electrode) on copper foils at a bath temperature of 80 ^{o}C. The whole absorption spectra can be divided into Fe L_2 and Fe L_3-edges which are separated because of spin-orbit interaction, with an energy separation of around 12 eV [118]. All of the spectra have been normalized followed by linear fitting and removal of the contribution of *sp* state.

As seen in Figure 4.33(a), the absorption peaks of Fe $L_{2,3}$-edge for the iron oxides films grown at 25 mV, 50 mV *vs.* Au electrode are similar, even after thermal treatment under vacuum. The absorption spectra are characteristic of Fe_3O_4 [63]. Yet, the spectral feature changes for the iron oxide film prepared at 100 mV where the Fe L_3-edge peak exhibits a doublet with a distinct shoulder at 709 eV similar to that of Fe_2O_3 [119, 120]. By carefully examining the B/A ratio, the value is 1.8 and the structure of the iron oxide is closed to α-Fe_2O_3 [118]. In comparison with the XANES result, the iron oxide film grown at 100 mV possesses close oxidation state with that of the standard Fe_3O_4 power sample. The contradiction could be because the Fe *K*-edge XANES measurement has a relative higher probe depth in comparison with that of the XAS. Consequently, the signals of Fe *K*-edge absorption are gathered from several tens of nm below the film surface, which is Fe_3O_4.

The values of full width at half maximum (FWHM) for Fe L_3-edge are 1.73 eV, 3.01

eV, 2.97 eV and 3.10 eV, corresponding to the samples grown at 100 mV, 50 mV, 25 mV and 50 mV (with annealing). The magnitude of the FWHM indicates that the peak broadening is ascribed to the co-existence of Fe^{3+} ions occupying both tetrahedral (A) and octahedral (B) sites while the core-hole lifetime broadenings of Fe L_2 and L_3 edges are 0.37 eV and 0.2 eV, respectively [107]. Moreover, a significantly smaller value was found for the 100 mV sample, showing a different microstructure from the iron oxide films grown at relatively lower potentials. Figure 4.33(b) shows Fe $L_{2,3}$-edge XAS spectra of the iron oxide films under applying alternating magnetic filed of 1 T. The solid (I_+) and dash (I_-) lines are the spectra taken with spin of photons parallel and anti-parallel to that of Fe 3*d* majority electrons. Apart from the sample prepared at 100 mV, all of others have distinct absorption difference between two spin directions. Interpretation of 2*p* absorption spectra for 3*d* transition metal compounds is associated with atomic multiplet calculation of the dipole transition from the ground state ($3d^n$) to final state ($2p^5 3d^{n+1}$) [121].

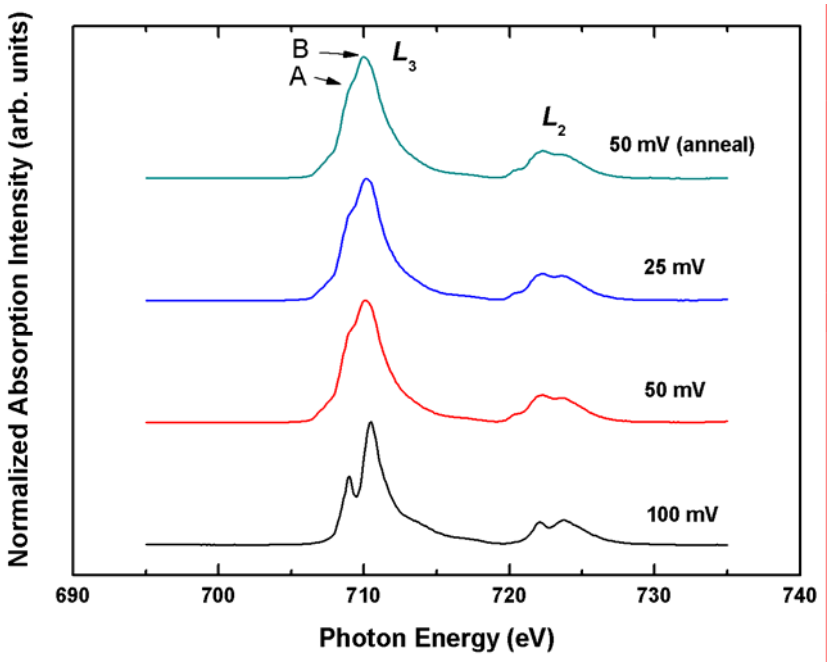
Although it is difficult to separate the contributions from two different Fe occupation sites on XAS spectra, the MCD asymmetry ratio, $(I_+-I_-)/(I_++I_-)$, can still provide useful information on the total magnetic moment originating from Fe ions at different sites. An integral difference calculation can be performed for either Fe L_2 or Fe L_3 edge. However, the former is more applicable owing to self-absorption and saturation artifacts on Fe L_3-edge region [122]. Table 4.4 shows the integrated values of the Fe L_2 edge spectra between 719 and 730 eV for I_+ and I_- spectrum separately. Significantly we find that the asymmetry ratio increases with decreasing applied potential indicating a change in the local magnetic properties of the material. In addition there is a notable increase in the asymmetry ratio on annealing without changing the crystallographic structure of Fe_3O_4 shown in Figure 4.26. The increase of the asymmetry ratio may be attributed to conversion of minor impurity phases formed in Fe_3O_4 or annealing of defects in the sublattice. Yet, this change was not observed in our Fe-edge XANES analysis. It is probably within the limits of the experimental resolution in *K*-edge measurement.

The normalized Fe $L_{2,3}$-edge XMCD spectra as indicated in Figure 4.34 is the difference of the I_+ and I_- spectrum. Consequently, there is no apparent MCD signal observed for the iron oxide grown at 100 mV *vs.* Au reference electrode. According to

the XRD analysis (Figure 4.26) the phase is Fe_3O_4, meaning strong magnetic dichroism should be observed due to its ferromagnetic behaviour [120]. Even if a few layers of Fe_3O_4 were oxidized into γ-Fe_2O_3 in air environment, the MCD signal should still be observed from sub-surface Fe_3O_4 [118]. Taking into account these facts one can conclude that there is a thin non–magnetic layer (> 50 Å) of iron oxide with similar structure to Fe_2O_3 present on top of the Fe_3O_4 thin film grown during electrodeposition at an applied potential of 100 mV *vs*. Au (Figure 4.35). For the cases of 50 mV (including the annealed sample) and 25 mV, the L_3 edge in the MCD spectra is composed of three peaks which can be assigned to different contributions of Fe^{2+} and Fe^{3+} at tetrahedral (A) and octahedral (B) sites. The chemical shift between d^5 and d^6 at B sites in the L_3 edge is 1.81 eV, which is in agreement with the reported values in the literature [123].

Additionally, from a comparison of MCD spectra at 50 mV the intensity of Fe^{3+}(B) peak shows a pronounced decrease after heating under vacuum as other two peaks at L_3 edge has no change, indicating part of Fe^{3+} ions at B sites are reduced. Hence, the increase on MCD asymmetry ratio after post-treatment is possibly associated with a change in the Fe^{3+} octahedrally co-ordinated sites.

(a)



(b)

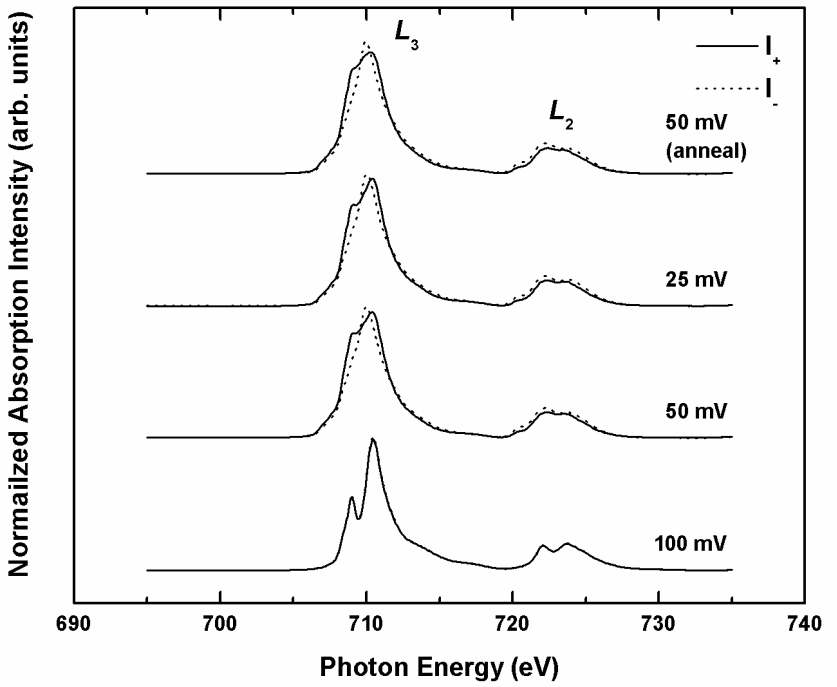


Figure 4.33: X-ray absorption spectrum of Fe_3O_4 thin film (a) without and (b) with an applied magnetic field of 1 T under a drain current mode operation.

Potential (mV)	I_+	I_-	I_+-I_-	I_++I_-	Asymmetry ratio
100	0.71731	0.74449	0.02718	1.4618	0.018594
50	0.75214	0.88069	0.12855	1.63283	0.078728
25	0.7967	0.9508	0.1541	1.7475	0.088183
50*	0.78586	0.98724	0.20138	1.7731	0.113575

Table 4.4: Calculation of MCD asymmetry ratio from Fe L_2-edge from XAS spectra (The Symbol "*" denotes the sample has been annealed before measurement)

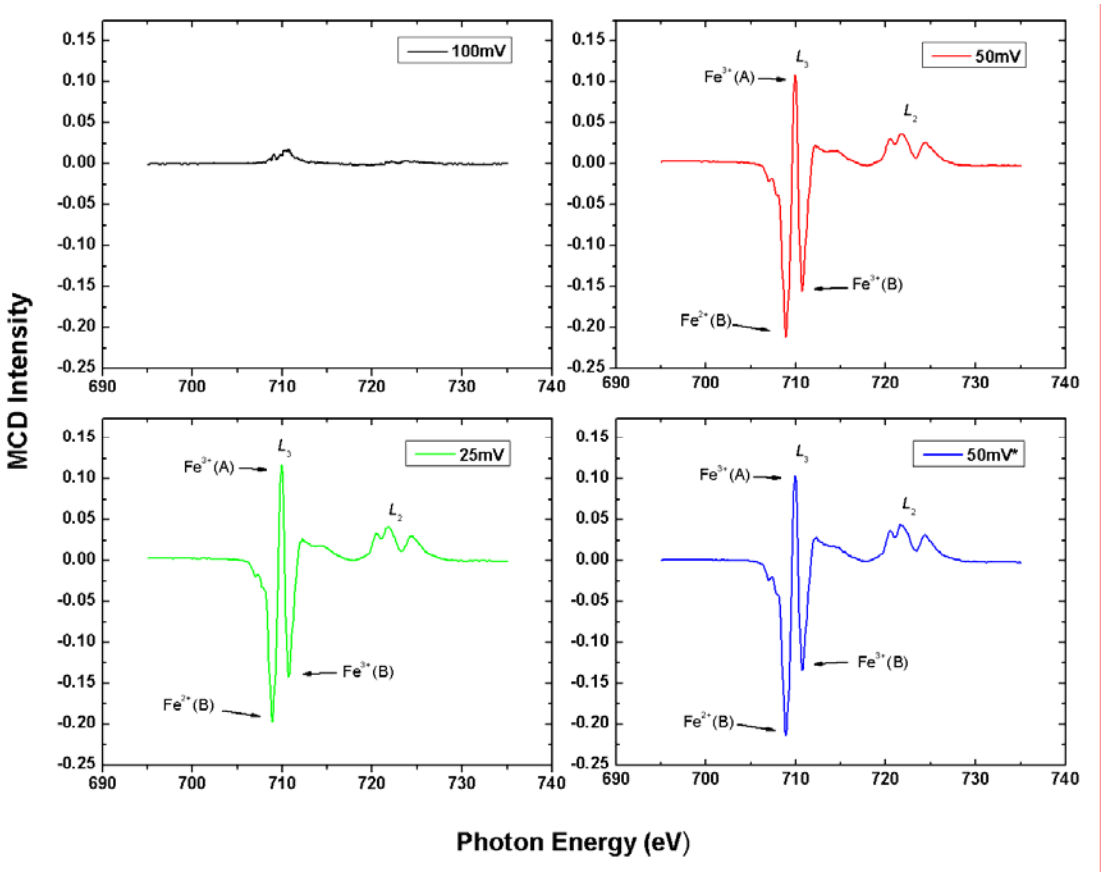


Figure 4.34: Fe $L_{2,3}$-edge MCD spectra of Fe_3O_4 grown at various potentials *vs.* Au reference electrode.

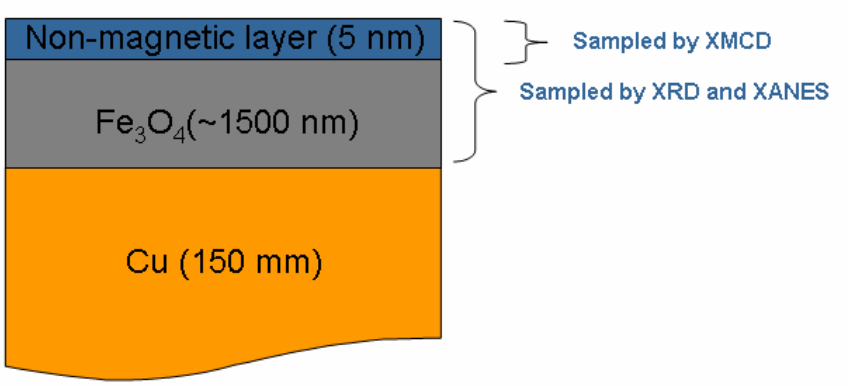


Figure 4.35: Schematic representation of Fe-oxide grown on to the copper substrate at 100 mV *vs.* Au reference electrode.

Vibrating Sample Magnetometer (VSM)

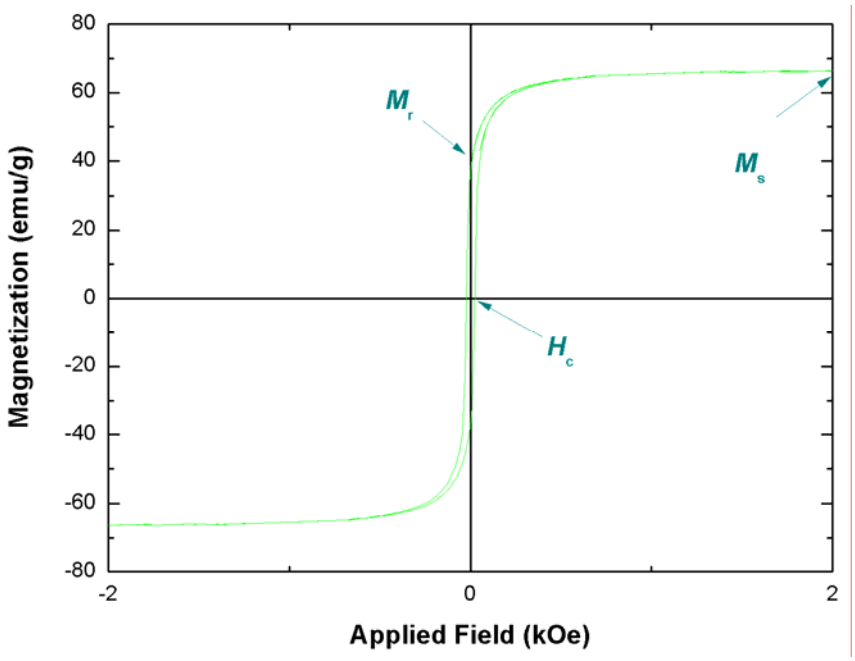
Magnetic hysteresis was performed for the iron oxide films grown on to Cu/Si substrates. All the data were recorded at a maximum applied field of 2 kOe. The curves were levelled to correct for diamagnetic effects of the substrate, sample holder, and any other linear background effects. Figure 4.36b shows magnetic hysteresis loops of the iron oxides prepared at different applied potentials *vs*. Au reference electrode. The field was applied in the plane of the film. As can be seen, the iron oxide grown at 200 mV and 400 mV exhibits relatively low magnetization compared with those grown at low applied potential regime (≤ 100 mV). This is consistent with the results measured by using X-ray diffraction (XRD), showing that the iron oxides are either α-FeOOH or γ-FeOOH with expected antiferromagnetic behaviour [124, 125]. At a potential ranging from 10 mV to 100 mV, the unsaturated behaviour was observed at 2 kOe. Surprisingly, the saturation magnetization increases significantly with increasing applied potential, more than doubles from 30 emu/g at 10 mV to 65 emu/g at 100 mV. However, the saturation magnetization values are lower than 92 emu/g measured for bulk Fe_3O_4 [48]. Some literature has attributed this to the presence of antiferromagnetic antiphase domain boundaries, resulting in difficulty to align the spins [38]. However, the lack of evidence in our x-ray scattering is observed. Another possibility could be the misplacement of Fe^{2+} and Fe^{3+} ions due to the low temperature process in which depositing atoms do not have enough kinetic energy to situate thermodynamically at spinel atomic positions [37] or "high-field" deposition due to very thin double layer existing between the working electrode and electrolyte.

The coercivity does seem to be the same at this regime with a value of about 25 Oe, and differs from that reported by Chatman *et al.* who suggested that magnetic coercivity has a tendency to increase with increasing applied deposition potential [126]. Nevertheless, the influence of applied potential occurs in the remanent magnetization (M_r/M_s). The remanent magnetizations for iron oxide films are 0.56, 0.66, 0.68 and 0.68 of M_s for 100 mV, 50 mV, 25 mV and 10 mV, respectively. It implies that magnetic response is somewhat slower for the iron oxides grown at high potentials. With small coercivity and large remanent magnetization the iron oxide films grown in this regime exhibit the characteristics of pseudo-single-domain (PSD) while the critical grain size for the single domain (SD) cubic Fe_3O_4 is below 76 nm, showing large values on coercivity and remanent [127]. This is agreement with the SEM observations with grain sizes ranging from 100 to 300 nm (Figure 4.30).

Figure 4.37 shows a comparison of two M-H loops recorded at 77 K and 300 K; the curves are virtually identical. This suggests that the temperature dependence is flat, which is what would be expected for a Curie temperature >> 300 K. The slightly smaller squareness found at 77 K can be associated with the reduction of thermally assisted spin rotation [128].

In this section, various characterization techniques such XRD, FEGSEM, VSM, EXAFS and XMCD have been used to study the electrodeposited Fe_3O_4 thin films grown at different potentials. According to XRD data, single phase of Fe_3O_4 can be formed only in the low potential regime (E < 100 mV). At higher potentials (E > 100 mV), the growth of α-FeOOH and γ-FeOOH is favourable. FEGSEM micrographs showed the distinct morphological changes that occur for the iron oxides prepared at different potentials. VSM data indicated that the saturation magnetization of electrodeposited Fe_3O_4 is somewhat lower than that of the bulk material. XANES spectra showed the amount of Fe^{3+} ions at tetrahedral sites is less in the as-deposited Fe_3O_4 than in bulk material suggesting that lattice defects may be the reason for the reduced magnetisation. Additionally, XMCD data indicates that the magnetic properties are influenced by a change of site occupancy of octahedral Fe^{3+} ions.

(a)



(b)

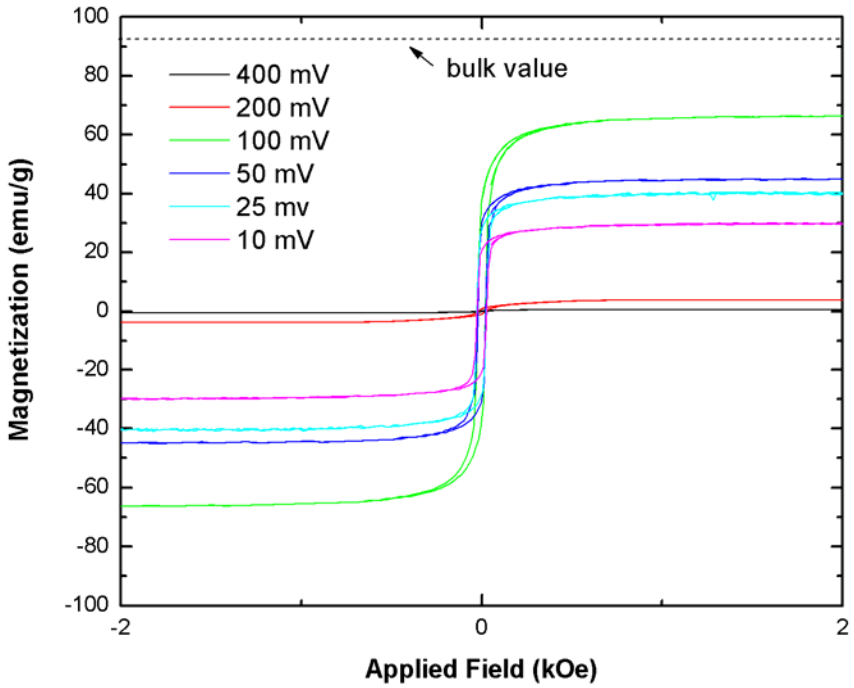


Figure 4.36: (a) Taking an example (100 mV case) showing the indications of the coercivity (H_c), remanent (M_r) and saturation magnetization (M_s). (b) Magnetic hysteresis loops of iron oxide films grown at various potentials *vs.* Au reference electrode recorded with respect to applied filed in-plane at 300 K.

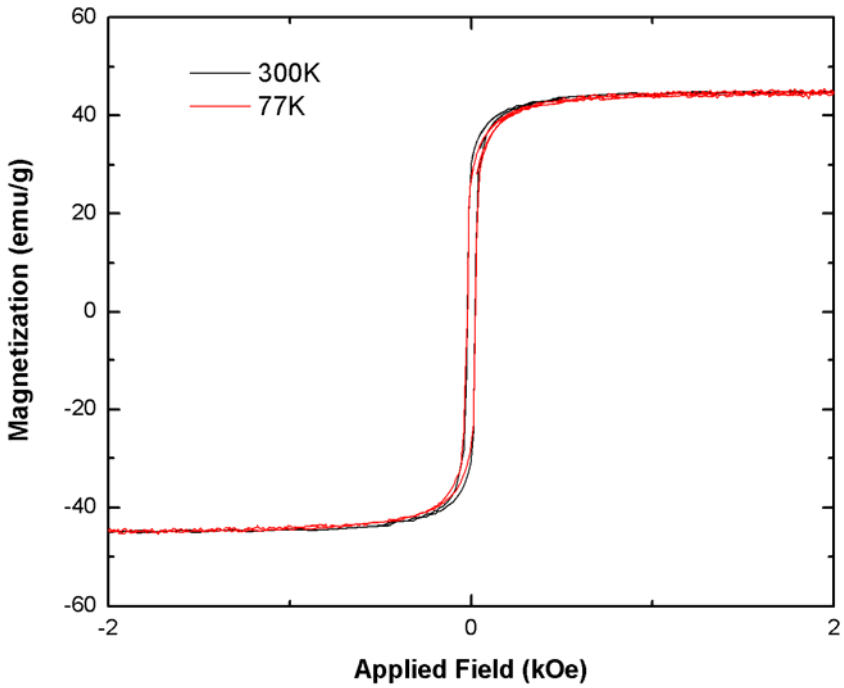


Figure 4.37: Temperature dependence of magnetic hysteresis loops of the iron oxide films grown at 50 mV *vs.* Au reference electrode measured with applied field in-plane.

5. Conclusions

In the present work, Fe_3O_4 thin films have been successfully electrodeposited on to copper substrates. Identification of Fe_3O_4 was carried out *via* XRD and EDS. AFM and FEGSEM measurements indicate that the Fe_3O_4 thin films are smooth, with a root-mean-square roughness of 12 nm over a 1x1 μm field of view. The formation of small clusters is also observed on the film surface and their size is a function of the applied current density. Acicular α-FeOOH (Néel temperature = 400 K) has been found at a relatively low growth temperature. This may be a candidate material as an insulating layer in spin-manipulating devices. Moreover, cross-section film homogeneity is revealed by ADF STEM images and shows that the growth of Fe_3O_4 is affected by substrate grain boundaries; this in turn is likely to affect the functional properties of such deposited films.

In order to investigate the detailed growth mechanism, the time-dependent growth of Fe oxide films on to Au/glass substrates was carefully studied. The grain size increased with increasing deposition time, and the homogeneous growth of Fe_3O_4 was obtained up to 300 s at an applied potential of 25 mV *vs.* Au reference electrode. Moreover, the microstructure of Fe_3O_4 exhibited an octahedral or rhombic grain shape, associated with the stability of specific surfaces in the spinel lattice, *i.e.* {111} and {110}.

NiO substrates were used to grow Fe-based oxides. Phase identification was confirmed by XRD and EDX measurements. The electrodeposited Fe_3O_4 film was grown homogeneously on air-formed NiO/Ni because the surface is hydrophilic in these electrolytes. AFM and FEGSEM results show that the Fe_3O_4 film surface is smooth with a sharp cubic structure except for a few clusters formed due to anomalous nucleation effect. The ADF STEM image reveals that electrodeposited Fe_3O_4 film has a uniform composition. Moreover, the multi-layered Fe_3O_4/α-FeOOH/Fe_3O_4 can been obtained through successive electrodeposition, although a thick and loose interlayer has been observed. These problems can be solved by adjusting the applied current density/potential, deposition time as well as

solution chemistry to improve the film morphology. To my understanding, this is first demonstration of a pure iron-based heterojunction producing by an electrochemical route. The aim is to grow a dense and thin insulator (< 10 nm), which is feasible for spintronic applications. From synchrotron x-ray diffraction experiments, it was found that the lattice parameter of Fe_3O_4 is slightly lower than that of bulk material and significantly there are no anti-phase boundaries in the as-deposited films. Owing to the poor conductivity of thicker NiO (> 10 nm), attempts to electrochemically deposit Fe_3O_4 on NiO/Ni{100}<001> were not successful. Since highly-textured NiO is easily grown by surface oxidation epitaxy (SOE) [129], more work still needs to be performed.

The influence of potential on structure, film morphology and magnetic properties were also investigated. According to the XRD results, iron oxide films grown on to Cu and Cu/Si substrates at a higher potential regime (> 100 mV) are either α-FeOOH or γ-FeOOH. Below 100 mV, single phase Fe_3O_4 can be obtained with highly crystallinity but no preferred orientation present. The film morphology changes drastically with applied potential, corresponding to the formation of different iron oxide phase. XANES analysis shows the iron oxide grown at the range of 25 mV~100 mV possesses an oxidation state close to the standard Fe_3O_4 power sample. In XMCD data, the iron oxide grown at 100 mV shows no MCD signal. This can be attributed to the formation of a non-ferromagnetic layer formed on top of the Fe_3O_4. Additionally, the asymmetry ratio increased with decreasing applied potential, indicating a microstructure change associated with Fe^{2+} and Fe^{3+} at different site occupancies. VSM measurement gave more detailed magnetic properties. The saturation magnetization of as-deposited Fe_3O_4 films has a lower value than reported for the bulk Fe_3O_4. It could be due to the presence of anti-phase grain boundaries or misplacement of Fe^{2+} and Fe^{3+} ions. Additionally, the squareness decreases with increasing applied potential. In the other words, the magnetic response is slower for the iron oxide films grown in the higher potential regime.

Solution chemistry in the electrolyte has given effects on the crystal structure and film morphology. By adding different amounts of CH_3COOK, the particle size of Fe_3O_4 film tends to increase up to reach a maximum of 50 nm (1 M CH_3COOK). However,

the value decreases with further increase in CH_3COOK. FEGSEM micrographs show that the number of surface clusters due to anomalous nucleation increases as concentration of CH_3COOK increases.

In summary, a variety of characterization techniques have been employed to investigate electrodeposited Fe_3O_4 thin films in order to understand its growth mechanism and material characteristics including structural and magnetic properties. The results indicate that single phase of Fe_3O_4 can be grown *via* an electrochemical route by adjusting appropriate growth temperature, bath composition and anodic potential, and that the magnetic properties such as saturation magnetization, coercivity and remanent are comparable with those of the Fe_3O_4 thin films prepared using vacuum deposition techniques, *i.e.* vapour deposition and sputtering. Consequently, it is possible to integrate electrodeposited Fe_3O_4 films with a suitable tunnelling barrier to fabricate spintronic devices. However, more studies on electronic and magnetic properties are required to understand the relation to electron spin and tunnelling behaviours in the fabricated device structure.

6. Future work

Electrodeposition of highly oriented or epitaxial Fe_3O_4

The soft solution process (SSP) is a potential approach to prepare metal oxides with novel structures, chemistry and properties. In this study polycrystalline Fe_3O_4 thin films have been electrochemically grown on several diamagnetic substrate materials. Although the quality of the Fe_3O_4 was comparable to that of vacuum deposition techniques, the actual application to spintronics is limited due to the isotropic behaviour of polycrystalline structure. In order to obtain anisotropic properties, it is necessary to grow the thin film with a highly preferred orientation or on epitaxial structure. This can be achieved by either using a single crystal working electrode or altering processing parameters (temperature and pH value) during deposition. In the present work, triangular-shape Fe_3O_4 has been found grown on to Cu/Si(001) substrates in Section 4.4. Further materials characterization still needs to be carried out to verify its anisotropic behaviour. Another interesting way to obtain preferred-orientated structure is to use magnetic-field-induced growth during electrodeposition. Electrochemical mass transport [130] and film properties [131] may be extremely sensitive to applied fields during deposition. One dimensional (1D) nanostructured Fe_3O_4 have been grown by applying a magnetic field to a hydrothermal cell [132]. The use of field gradients during processing could be investigated as a way to affect film orientation, defect density and possible nanostructuring.

Measurement of magnetic properties for various ferrous oxide films

In the present work, VSM measurements have been carried out to quantify total magnetic moment for iron oxide films. It is necessary to combine XMCD data to separate spin and orbital magnetic moments of Fe_3O_4. The band-structure calculation could be involved with a local density approximation [117]. Additionally, further magnetic measurements such as zero field cooled (ZFC) and field cooled (FC) measurements are needed in order to understand the magnetic properties of

electrodeposited iron oxides at low temperature.

Growth of insulating barriers

α-FeOOH is a candidate as an insulating barrier for MTJ devices. A smooth and thin layer (< 10 nm) of α-FeOOH are the basic requirements to meet. Lower anodic current density/applied potential or reducing Fe^{2+} ions in electrolyte can be a good approach. Besides, the final product of α-FeOOH *via* thermal treatment at 400 ^{o}C is α-Fe_2O_3 [133]. The idea is to electrochemically form a sandwich structure of Fe_3O_4/α-Fe_2O_3/Fe_3O_4 for spintronic applications. To my understanding, such a structure has not been demonstrated. Materials characterization (*i.e.* structural, electrical, magnetic properties) will become more challenging since it only contains Fe and O atoms with a very small variation on chemical composition. Another possible insulator is $ZnFe_2O_4$ (a = 0.844 nm) [134] which could potentially be grown *via* co-deposition under certain growth conditions [135]. Therefore, epitaxial growth of Fe_3O_4/$ZnFe_2O_4$/Fe_3O_4 could be obtained.

Furthermore, it has been shown that the synchrotron technique is a powerful tool to study core-level behaviours even though the theoretical understanding is complex. However, it is vital to investigate a variety of material characteristics by employing various synchrotron techniques in order to continue with device/structure minimization.

Appendices

A-1: Nernst Equation

The Gibbs's free energy can be expressed as the electric work that is done from the point of view of electrochemistry.

$$\Delta G = -W = -q\Delta E \quad \text{(A-1-1)}$$

In a redox reaction, the total amount of electrons (n) participating in the reaction is related to the charge transferred. Therefore,

$$q = nF \quad \text{(A-1-2)}$$

where F is the Faraday's constant with the magnitude of 96485 Columb. Equation (A-1-1) can be rewritten into

$$\Delta G = -nF\Delta E \quad \text{(A-1-3)}$$

Under a standard condition (25 ^{o}C and 1 atm), equation (A-1-3) becomes

$$\Delta G^{0} = -nF\Delta E^{0} \quad \text{(A-1-4)}$$

For a redox reaction where reactants A and B react into C and D, the chemical reaction formula is

$$aA + bB = cC + dD \quad \text{(A-1-5)}$$

In order to correlate the Gibbs's free energy, and electromotive force (EMF), it is convenient to set a parameter called reaction quotient below

$$Q = \frac{[C]^c[D]^d}{[A]^a[B]^b} \qquad \text{(A-1-6)}$$

Moreover,

$$\Delta G = \Delta G^0 + RT \ln Q \qquad \text{(A-1-7)}$$

Put equations (A-1-3), (A-1-4) into (A-1-7),

$$-nF\Delta E = -nF\Delta E^0 + RT \ln G \qquad \text{(A-1-8)}$$

where R and T are gas constant (8.314 J·mol^{-1}K^{-1})and absolute temperature (K), respectively. After arranging equation (A-1-8), we have

$$\Delta E = \Delta E^0 - \frac{RT}{nF} \ln \frac{[C]^c[D]^d}{[A]^a[B]^b} \qquad \text{(A-1-9)}$$

A-2: Derivation of Steady-State Current Density [69]

Consider an infinitesimal area of the electrode surface. The adion concentration can be expressed as below.

$$\left(i_{a,x} \Big/ zF \, dxdy \right) = \left(i_{c,x} \Big/ zF \right) dxdy + D \left(\partial^2 c_{ad,x} \Big/ \partial x^2 \right) dxdy \qquad \text{(A-2-1)}$$

Since

$$i_{a,x} \Big/ zF = \left(i_0 \Big/ zFc^0_{ad,x} \right) c_{ad,x} \exp\left\{ \left[(1-\beta) zF \Big/ RT \right] \eta_a \right\} = K_{a,\eta} c_{ad,x} \qquad \text{(A-2-2)}$$

and

$$i_{a,x}/zF = \left(i_0/zF\right)\exp\left[-\left(\beta zF/RT\right)\eta_a\right] \quad \text{(A-2-3)}$$

Equation (A-3-2) becomes

$$c_{ad,x} - \left(D/K_{a,\eta}\right)\left(\partial^2 c_{ad,x}/\partial x^2\right) = c_{ad}^{\infty} \qquad \text{(A-2-4)}$$

where

$$c_{ad}^{\infty} = \left(i_c/zFK_{a,\eta}\right) = c_{ad}^{0}\exp\left[-\left(zF/RT\right)\eta_a\right] \qquad \text{(A-2-5)}$$

Using boundary condition

$$c_{ad,x=0} = c_{ad}^{0} \qquad \text{(A-2-6)}$$

And assume the equilibrium remain undisturbed at the growth line, that is

$$\left(dc_{ad,x}/dx\right)_{x=x_0} = 0 \quad \text{(A-2-7)}$$

To solve equation (A-2-4) with equation (A-2-6) and (A-2-7)

$$c_{ad,x}/c_{ad}^{0} = \exp\left[-\left(zF/RT\right)\eta_a\right] + \frac{1-\exp\left[-\left(zF/RT\right)\eta_a\right]}{1+\exp\left[-2\left(i_0/zFv_0\right)^{1/2}p\right]}$$

$$\cdot\left\{\exp\left[-2\left(i_0/zFv_0\right)^{1/2}p\right]\exp\left[\left(i_0/zFv_0\right)^{1/2}p\left(\frac{x}{x_0}\right)\right]+\exp\left[-\left(i_0/zFv_0\right)^{1/2}p\left(\frac{x}{x_0}\right)\right]\right\}$$

(A-2-8)

where

$$p=\exp\left\{\left[(1-\beta)zF/RT\right]\eta_a\right\} \quad \text{(A-2-9)}$$

and

$$v_0=\left(Dc_{ad}^0/x_0^2\right) \quad \text{(A-2-10)}$$

Now, the current density is described

$$i_x=i_0\left\{\left(c_{ad,x}/c_{ad}^0\right)\exp\left[\left[(1-\beta)zF/RT\right]\eta_a-\exp\left[-\left(\beta zF/RT\right)\eta_a\right]\right]\right\} \quad \text{(A-2-10)}$$

Replace the distribution of adion concentration in equation (A-2-10) with (A-2-8)

$$i=i_0^{1/2}\left(zFv_0\right)^{1/2}\exp\left[\left[-(1+\beta)zF/2RT\right]\eta_a\right]$$

$$\cdot\left\{\exp\left[\left(xF/RT\right)\eta_a\right]-1\right\}\frac{1-\exp\left[-2\left(i_0/zFv_0\right)^{1/2}p\right]}{1+\exp\left[-2\left(i_0/zFv_0\right)^{1/2}p\right]} \quad \text{(A-2-11)}$$

Equation (A-2-11) can be rewritten as

$$y=\left[(1+\beta)zF/4.6RT\right]\eta_a+\log\frac{1+\exp\left[-2\left(i_0/zFv_0\right)^{1/2}p\right]}{1-\exp\left[-2\left(i_0/zFv_0\right)^{1/2}p\right]}-\frac{1}{2}\log\left(i_0zFv_0\right) \quad \text{(A-2-12)}$$

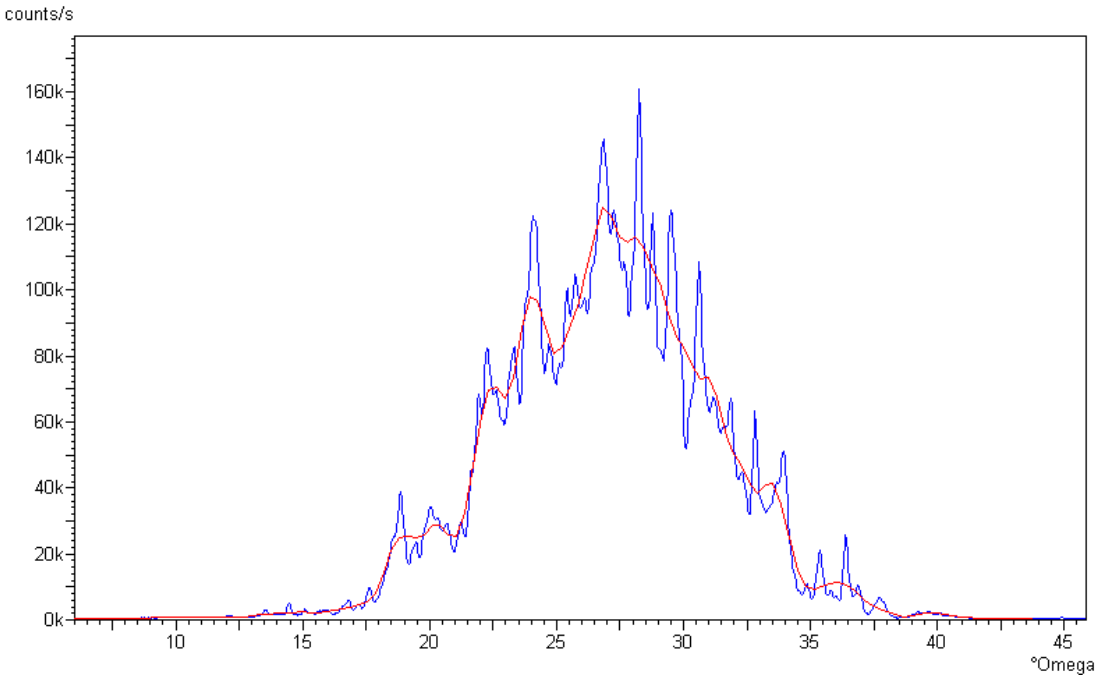
where

$$y = \exp\left\{\left[\left(zF/RT\right)\eta_a\right] - 1/i\right\} \quad \text{(A-2-13)}$$

A-3: Calculation of crystallite site using Scherrer equation

Deposition time (min)	Crystallite size (nm)	Grain size from AFM (nm)	Average thickness (nm)
30	32	200	166
40	37	-	150
50	36	200	172

A-4: The Rocking Curves of Ni {100}<001> Tape



A-5: X-ray diffraction patterns

A-5-1: Nickel, syn (JCPDS No. 04-0850)

Formula: Ni
Space group: Fm-3m
Cell parameters: a = 3.5238 Å
Radiation: Cu K-alpha
Wavelength (Å): 1.54056

Peaks

d-spacing (Å)	Relative Intensity (%)	Angle (^{o}2Theta)	Plane (h k l)
2.03400	100.00	44.50662	1 1 1
1.76200	42.00	51.84593	2 0 0
1.24600	21.00	76.36994	2 2 0
1.06240	20.00	92.94396	3 1 1
1.01720	7.00	98.44563	2 2 2
0.88100	4.00	121.93029	4 0 0
0.80840	14.00	144.66928	3 3 1
0.78800	15.00	155.65254	4 2 0

A-5-2: Copper, syn (JCPDS No. 04-0836)

Formula: Cu
Space group: Fm-3m
Crystal system: Cubic
Cell parameters: a = 3.615 Å
Radiation: Cu K-alpha
Wavelength (Å): 1.54056

Peaks

d-spacing (Å)	Relative Intensity (%)	Angle (^{o}2Theta)	Plane (h k l)
2.08800	100.00	43.29658	1 1 0

1.80800	46.00	50.43300	2 0 0
1.27800	20.00	74.13034	2 2 0
1.09000	17.00	89.93068	3 1 1
1.04360	5.00	95.13944	2 2 2
0.90380	3.00	116.91847	4 0 0
0.82930	9.00	136.50680	3 3 1
0.80830	8.00	144.71382	4 2 0

A-5-3: Gold, syn (JCPDS No. 04-0784)

Formula: Au
Space group: Fm-3m
Crystal system: Cubic
Cell parameters: a = 4.0786 Å
Radiation: Cu K-alpha
Wavelength (Å): 1.54056

Peaks

d-spacing (Å)	Relative Intensity (%)	Angle (^{o}2Theta)	Plane (h k l)
2.35500	100.00	38.18362	1 1 0
2.03900	52.00	44.39166	2 0 0
1.44200	32.00	64.57593	2 2 0
1.23000	36.00	77.54709	3 1 1
1.17740	12.00	81.72124	2 2 2
1.0960	6.00	98.13339	4 0 0
0.93580	23.00	110.79762	3 3 1
0.91200	22.00	115.25934	4 2 0
0.83250	23.00	135.41557	4 2 2

A-5-4: Magnetite, syn (JCPDS No. 19-0629)

Formula: Fe_3O_4
Space group: *Fd-3m*
Crystal system: Cubic

Cell Parameters: a = 8.396 Å
Radiation: Cu K-alpha
Wavelength (Å): 1.54056

Peaks

d-spacing (Å)	Relative Intensity (%)	Angle (^{o}2Theta)	Plane (h k l)
4.85200	8.00	18.26930	1 1 1
2.96700	30.00	30.09453	2 2 0
2.53200	100.00	35.42225	3 1 1
2.42430	8.00	37.05176	2 2 2
2.09930	20.00	43.05187	4 0 0
1.71460	10.00	53.39085	4 2 2
1.61580	30.00	56.94246	5 1 1
1.48450	40.00	62.51455	4 4 0
1.41920	2.00	65.74296	5 3 1
1.32770	4.00	70.92376	6 2 0
1.28070	10.00	73.94797	5 3 3
1.26590	4.00	74.95995	6 2 2
1.21190	2.00	78.92855	4 4 4
1.12210	4.00	86.70153	6 4 2
1.09300	12.00	89.61696	7 3 1
1.04960	6.00	94.42525	8 0 0
0.98960	2.00	102.22408	6 6 0
0.96950	6.00	105.21849	7 5 1
0.96320	4.00	106.20470	6 6 2
0.93880	4.00	110.26860	8 4 0
0.89520	2.00	118.73559	6 6 4
0.88020	6.00	122.11819	9 3 1
0.85690	8.00	128.03155	8 4 4
0.82330	4.00	138.65080	10 2 0
0.81170	6.00	143.23461	9 5 1
0.80800	4.00	144.84784	10 2 2

A-5-5: Hematite, syn (JCPDS No. 33-0664)

Formula: α-Fe_2O_3
Space group: *R-3c*
Crystal system: Rhombohedral
Cell Parameters: a = 5.0356 Å; c = 13.7489 Å
Radiation: Cu K-alpha
Wavelength (Å): 1.54056

Peaks

d-spacing (Å)	Relative Intensity (%)	Angle (^{o}2Theta)	Plane (h k l)
3.68400	30.00	24.13782	0 1 2
2.70000	100.00	33.15224	1 0 4
2.51900	70.00	35.61116	1 1 0
2.29200	3.00	39.27564	0 0 6
2.20700	20.00	40.85438	1 1 3
2.07790	3.00	43.51774	2 0 2
1.84060	40.00	49.47908	0 2 4
1.69410	45.00	54.08920	1 1 6
1.63670	1.00	56.15039	2 1 1
1.60330	5.00	57.42752	1 2 2
1.59920	10.00	57.58851	0 1 8
1.48590	30.00	62.44902	2 1 4
1.45380	30.00	63.98916	3 0 0
1.41380	1.00	66.02603	1 2 5
1.34970	3.00	69.59875	2 0 8
1.31150	10.00	71.93517	1 0 10
1.30640	6.00	72.26014	1 1 9
1.25920	8.00	75.42820	2 2 0
1.22760	4.00	77.72716	3 0 6
1.21410	2.00	78.75771	2 2 3
1.18960	5.00	80.70852	1 2 8
1.16320	5.00	82.93693	0 2 10
1.14110	7.00	84.91340	1 3 4
1.10350	7.00	88.53889	2 2 6
1.07680	2.00	91.34243	0 4 2

1.05570	7.00	93.71229	2 1 10
1.04280	1.00	95.23566	1 1 12
1.03930	3.00	95.65940	4 0 4
0.98920	4.00	102.28155	3 1 8
0.97150	1.00	104.91038	2 2 9
0.96060	5.00	106.61883	3 2 4
0.95810	4.00	107.02106	0 1 14
0.95160	5.00	108.08597	4 1 0
0.93180	2.00	111.51391	4 1 3
0.92060	2.00	113.58972	0 4 8
0.90810	5.00	116.03990	1 3 10
0.89980	1.00	117.75339	3 0 12
0.89540	3.00	118.69238	2 0 14
0.87890	6.00	122.42546	4 1 6
0.86480	1.00	125.92345	2 3 8
0.85430	3.00	128.75174	4 0 10
0.84360	5.00	131.87094	1 2 14
0.83920	3.00	133.23450	3 0 3
0.80890	4.00	144.44755	3 2 10
0.80140	4.00	147.96105	2 4 4

A-5-6: Maghemite-C, syn (JCPDS No. 39-1346)

Formula: γ-Fe_2O_3
Space group: *P4132*
Crystal system: Cubic
Cell Parameters: a = 8.3515 Å
Radiation: Cu K-alpha
Wavelength (Å): 1.54056

Peaks

d-spacing (Å)	Relative Intensity (%)	Angle (^{o}2Theta)	Plane (h k l)
5.91800	5.00	14.95754	1 1 0
4.82200	4.00	18.38394	1 1 1
3.74000	5.00	23.77108	2 1 0

3.41100	5.00	26.10248	2 1 1
2.95300	35.00	30.24060	2 2 0
2.78400	2.00	32.12444	2 2 1
2.64350	2.00	33.88195	3 1 0
2.51770	100.00	35.63016	3 1 1
2.41190	3.00	37.24923	2 2 2
2.31630	1.00	38.84695	3 2 0
2.23200	1.00	40.37672	3 2 1
2.08860	16.00	43.28351	4 0 0
2.02550	1.00	44.70345	4 1 0
1.96850	1.00	46.07120	3 3 0
1.82240	2.00	50.00697	4 2 1
1.70450	10.00	53.73254	4 2 2
1.67030	1.00	54.92432	4 3 0
1.63790	1.00	56.10561	5 1 0
1.60730	24.00	57.27135	5 1 1
1.55070	1.00	59.56785	5 2 0
1.52480	2.00	60.68500	5 2 1
1.47580	34.00	62.92503	4 4 0
1.45370	1.00	63.99409	4 4 1
1.43220	1.00	65.07207	5 3 0
1.39190	1.00	67.20141	4 4 2
1.37300	1.00	68.25269	6 1 0
1.35470	1.00	69.30507	6 1 1
1.32040	3.00	71.37566	6 2 0
1.30420	1.00	72.40132	5 4 0
1.27300	5.00	74.47069	5 3 3
1.25900	2.00	75.44228	6 2 2
1.24500	1.00	76.44235	6 3 0
1.23140	1.00	77.44248	6 3 1
1.20530	1.00	79.44612	4 4 4
1.19310	1.00	80.43219	6 3 2
1.18100	1.00	81.41943	7 1 0
1.13650	1.00	85.33849	7 2 1
1.11590	2.00	87.30406	6 4 2
1.09660	1.00	89.24388	7 3 0
1.08720	7.00	90.22582	7 3 1
1.04390	3.00	95.10342	8 0 0

A-5-7: Goethite, syn (JCPDS No. 29-0713)

Formula: α-FeOOH
Space group: *Pbnm*
Crystal system: Orthorhombic
Cell Parameters: a = 4.608 Å; b = 9.956 Å; c = 3.0215 Å
Radiation: Cu K-alpha
Wavelength (Å): 1.54056

Peaks

d-spacing (Å)	Relative Intensity (%)	Angle (^{o}2Theta)	Plane (h k l)
4.98000	12.00	17.79586	0 2 0
4.18300	100.00	21.22262	1 1 0
3.38300	10.00	26.32262	1 2 0
2.69300	35.00	33.24091	1 3 0
2.58300	12.00	34.70041	0 2 1
2.52700	4.00	35.49466	1 0 1
2.48900	10.00	36.05503	0 4 0
2.45000	50.00	36.64919	1 1 1
2.30300	1.00	39.08039	2 0 0
2.25300	14.00	39.98423	1 2 1
2.19000	18.00	41.18585	1 4 0
2.08900	1.00	43.27481	2 2 0
2.01100	2.00	45.04340	1 3 1
1.92000	5.00	47.30487	0 4 1
1.80200	6.00	50.61274	2 1 1
1.77280	1.00	51.50685	1 4 1
1.71920	20.00	53.23672	2 2 1
1.69060	6.00	54.21034	2 4 0
1.65930	3.00	55.31949	0 6 0
1.60370	4.00	57.41186	2 3 1
1.56370	10.00	59.02335	1 5 1
1.56140	8.00	59.11892	1 6 0
1.50910	8.00	61.38408	0 0 2
1.46750	2.00	63.32204	3 2 0
1.45410	5.00	63.97439	0 6 1

1.42070	2.00	65.66480	1 1 2
1.39360	3.00	67.10856	3 3 0
1.36940	2.00	68.45697	3 0 1
1.35900	3.00	69.05464	1 7 0
1.34590	1.00	69.82376	2 6 0
1.31730	3.00	71.56946	1 3 2
1.29210	1.00	73.18871	0 4 2
1.26540	1.00	74.99467	3 3 1
1.24370	1.00	76.53671	1 4 2
1.19940	1.00	79.91528	3 4 1
1.15060	1.00	84.05071	0 8 1
1.14450	1.00	84.60233	4 1 0
1.12630	1.00	86.29880	2 4 2

A-5-8: Lepidocrocite, syn (JCPDS No. 44-1415)

Formula: γ-FeOOH
Space group: *Bbmm*
Crystal system: Orthorhombic
Cell Parameters: a = 12.52 Å; b = 3.873 Å; c = 3.071 Å
Radiation: Cu K-alpha
Wavelength (Å): 1.54056

Peaks

d-spacing (Å)	Relative Intensity (%)	Angle (^{o}2Theta)	Plane (h k l)
6.27000	61.00	14.11342	2 0 0
3.29400	100.00	27.04690	2 1 0
2.98100	8.00	29.94988	1 0 1
2.47300	76.00	36.29640	3 0 1
2.43400	34.00	36.89876	4 1 0
2.36200	36.00	38.06609	1 1 1
2.08600	9.00	43.34019	6 0 0
2.08600	9.00	43.34019	3 1 1
1.94040	53.00	46.77775	5 0 1
1.93510	72.00	46.91353	0 2 0
1.85020	12.00	49.20526	2 2 0

1.83750	8.00	49.56818	6 1 0
1.73500	21.00	52.71433	5 1 1
1.62380	5.00	56.63652	1 2 1
1.56500	3.00	58.96947	8 0 0
1.53440	33.00	60.26578	0 0 2
1.52480	30.00	60.68500	3 2 1
1.49150	5.00	62.18838	2 0 2
1.45100	5.00	64.12736	8 1 0
1.43570	8.00	64.89394	7 1 1
1.41920	3.00	65.74296	6 2 0
1.39160	12.00	67.21783	2 1 2
1.37110	12.00	68.36034	5 2 1
1.29840	4.00	72.77642	4 1 2
1.26720	3.00	74.11299	9 0 1
1.26370	5.00	74.86963	2 3 0
1.21750	2.00	75.11299	8 2 0
1.20450	9.00	79.50937	9 1 1
1.20300	11.00	79.62827	0 2 2
1.19140	7.00	80.56150	10 1 0
1.18450	7.00	81.12840	1 3 1
1.18140	7.00	81.38605	2 2 2
1.17810	4.00	81.66236	6 1 2
1.09600	1.00	89.30581	8 0 2

References

1. Prinz, G. A., *Magnetoelectronics.* Science, 1998. **282**: p. 1660.
2. Wolf, S. A., Awschalom, D. D., Buhrman, R. A., Daughton, J. M., von. Molnár, S., Roukes, M. L., Chtchelkanova, A. Y. and Treger, D. M., *Spintronics: A Spin-Based Electronics Vision for the Future.* Science, 2001. **294**: p. 1488.
3. Coufal, H., Dhar, L. and Mee, C. D., *Materials for Magnetic Data Storage: The Ongoing Quest for Superior Magnetic Materials.* MRS Bulletin, 2006. **31**: p. 374.
4. Bertram, H. N. and Williams, M., *SNR and Density Limit Estimates: A Comparison of Longitudinal and Perpendicular Recording.* IEEE Transactions on Magnetics, 2000. **36**: p. 4.
5. Tedrow, P. M. and Meservey, R., *Spin Polarization of Electrons Tunneling from Films of Fe, Co, Ni, and Gd.* Physical Review B, 1973. **7**: p. 318.
6. Julliere, M., *Tunneling Between Ferromagnetic Films.* Physics Letters, 1975. **54A**: p. 225.
7. Baibich, M. N., Broto, J. M., Fert, A., Dau, F. N. V., Petroff, F., Eitenne, P., Creuzet, G., Friederich, A. and Chazelas, J., *Giant Magnetoresistance of (001)Fe/(001Cr Magnetic Superlattices.* Physical Review Letters, 1998. **61**: p. 2472.
8. O'Handley, R. C., *Modern Magnetic Materials: Principle and Applications*. 2000, New York: John Wiley & Sons, Inc.
9. Heim, D. E., Fontana, Jr., R. E., Tsang, C., Speriosu, V. S., Gurney, B. A. and Williams, M. L., *Design and Operation of Spin Valve Sensors.* IEEE Transactions on Magnetics, 1994. **30**: p. 316.
10. Parkin, S. S. P., *Dramatic Enhancement of Interlayer Exchange Coupling and*

Giant Magnetoresistance in $Ni_{81}Fe_{19}$/Cu Multilayers by Addition of Thin Co Interface Layers. Applied Physics Letters, 1992. **61**: p. 1358.

11. Irie, Y., Sakakima, H., Satomi, M. and Kawawake, Y., *Spin-Valve Memory Elements Using [{Co-Pt/Cu/Ni-Fe-Co}] Multilayers.* Japanese Journal of Applied Physics, 1995. **34**: p. L415.
12. Yoshimura, M., *Importance of Soft Solution Processing for Advanced Inorganic Materials.* Journal of Materials Research, 1998. **13**: p. 796.
13. Wyckoff, R. W. G., *Crystal Structure*. Vol. 2. 1963, New York: Interscience.
14. Fleet, M. E., *The Structure of Magnetite.* Acta Crystallographica, 1981. **B37**: p. 917.
15. McKie, D. and Mckie, C., *Crystalline Solids*. 1974, Walton-on-Thames, Surrey: Thomas Nelson and Sons, Ltd.
16. Darken, L. S. and Gurry, R. W., *The System Iron-Oxygen. II. The Wustite Field and Related Equilibria.* Journal of the American Chemical Society, 1946. **68**: p. 708.
17. Wells, A. F., *Structure Inorganic Chemistry*. 1984, Oxford: Clarendon Press. 551.
18. Cornell, R. M. and Schwertmann, U., *The iron Oxides*. 2 ed. 2003, KGaA, Weinheim: Wiley-VCH Verlag GmbH & Co.
19. Miles, P. A., Westphal, W. B. and Happel, A. v., *Dielectric Spectroscopy of Ferromagnetic semiconductors.* Reviews of Modern Physics, 1957. **29**: p. 279.
20. Verwey, E. J. W. and Boer, J. H. d., *Cation Arrangement in A Few Oxides with Crystal Structures of the Spinel Type.* Recueil des Travaux Chimiques des Pays-Bas et de la Belgique, 1936. **55**: p. 531.
21. Verwey, E. J. W., *Electronic Conduction of Magnetite (Fe_3O_4) and its Transition Point at Low Temperature.* Nature, 1939. **144**: p. 327.

22. Verwey, E. J. W. and Haayman, P. W., *Electronic conductivity and transition point of magnetite ("Fe_3O_4").* Physica, 1941. **8**: p. 979.

23. Verwey, E. J. W., Haayman, P. W. and Romeijn, P. C., *Physical Properties and cation Arrangement of Oxides with Spinel Structures: II. Electronic Conductivity.* Journal of Chemical Physics, 1947. **15**: p. 181.

24. Bickford, Jr., L. R., *The Low Temperature Transformation in Ferrites.* Reviews of Modern Physics, 1953. **25**: p. 75.

25. Yoshida, J. and Iida, S., *X-Ray Study of the Phase Transition in Magnetite.* Journal of the Physical Society of Japan, 1979. **47**: p. 1627.

26. de Groot, R. A., Mueller, F. M., van Engen, P. G. and Buschow, K. H. J., *New Class of Materials: Half-Metallic Ferromagnets.* Physical Review Letters, 1983. **50**: p. 2024.

27. Coey, J. M. D., Versluijs, J. J. and Venkatesan, M., *Half-metallic Oxide Point Contacts.* Journal of Physics D: Applied Physics, 2002. **35**: p. 2457.

28. Zhang, Z. and Satpathy, S., *Electron States, Magnetism, and the Verwey Transition in Magnetite.* Physical Review B, 1991. **44**: p. 13319.

29. Alvarado, S. F., Eib, W., Meier, F., Pierce, D. T., Sattler, K. and Siegmann, H. C., *Observation of Spin-Polarized Electron Levels in Ferrites.* Physical Review Letters, 1975. **34**: p. 319.

30. Dedkov, Yu. S., Rüdiger, U. and Güntherodt, G., *Evidence for the Half-metalic Ferromagnetic State of Fe_3O_4 by Spin-resolved Photoelectron spectroscopy.* Physical Review B, 2002. **65**: p. 064417.

31. Steenbeck, K., Eick, T., Kirsch, K., O'Donnell, K. and Steinbeiβ, E., *Influence of a 36.8^o Grain Boundary on the Magnetoresistance of $La_{0.8}Sr_{0.2}MnO_{3-\delta}$ Single Crystal Films.* Applied Physics Letters, 1997. **71**: p. 968.

32. Versluijs, J. J., Bari, M. A. and Coey, J. M. D., *Magnetoresistance of*

Half-Metallic Oxide Nanocontacts. Physical Review Letters, 2001. **87**: p. 026601-1.

33. Coey, J. M. D., Berkowitz, A. E., Balcells, LI., Putris, F. F. and Parker, F. T., *Magetoresistance of Magnetite.* Applied Physics Letters, 1998. **72**: p. 734.
34. Anderson, P. W. and Hasegawa, H., *Considerations on Double Exchange.* Physical Review, 1955. **100**: p. 675.
35. Smith, D. L., *Thin-Film Deposition: Principles and Practice*. 1995, New York: McGraw-Hill.
36. Furubayashi, T., *Magnetoresistance of Magnetite Films Prepared by Reactive Evaporation.* Journal of Applied Physics, 2003. **93**: p. 8026.
37. Ortiz, C., Lim, G., Chen, M. M. and Castillo, G., *Physical Properties of Spinel Iron Oxide Thin Films.* Journal of Materials Research, 1988. **3**: p. 344.
38. Liu, H., Jiang, E. Y., Bai, H. L., Zheng, R. K., Wei, H. L. and Zhang, X. X., *Large Room-temperature Spin-dependent Tunneling Magnetoresisstance in Polycrystalline Fe_3O_4 Films.* Applied Physics Letters, 2003. **83**: p. 3531.
39. Liu, H., Jiang, E. Y., Zheng, R. K. and Bai, H. L., *Structure and Magnetic Properties of Polycrystalline Fe_3O_4 Films Deposited by Reactive Sputtering at Room Temperature.* Physica Status Solidi, Section A: Applied Research, 2004. **201**: p. 739.
40. Chang, H. S. W., Chiou, C. and Chen, Y., *Synthesis, Characterization, and Magnetic Properties of Fe_3O_4 Thin Films Prepared via Sol-Sel Method.* Journal of Solid State Chemistry, 1997. **128**: p. 87.
41. Abe, M. and Tamura, Y., *Ferrite-Plating in Aqueous Solution: A New Method for Preparing Magnetic Thin Film.* Japanese Journal of Applied Physics, 1983. **22**: p. L511.
42. Abe, M., Tanno, Y. and Tamaura, Y., *Direct Formation of Ferrite Films in Wet*

Process. Journal of Applied Physics, 1985. **57**: p. 3795.

43. Nishimura, K., Kitamoto, Y. and Abe, M., *Electro-Ferrite Plating of Magnetite at 24-80 ^{o}C.* IEEE Transactions on Magnetics, 1999. **35**: p. 3043.

44. Pourbaix, M., *Atlas of Electrochemical Equilibria in Aqueous Solution*. 2nd ed. 1974, Huston, TX: National Association of Corrosion Engineers. 309.

45. Carlier, D., Terrier, C., Arm, C. and Ansermet, J.-P., *Preparation and Magnetic Properties of Fe_3O_4 Nanostructures Grown by Electrodeposition.* Electrochemical and Solid-State Letters, 2005. **8**: p. C43.

46. Fitzgerald, A. G. and May, T. G., *Defects in Epitaxial Ferrite Films Grown by Chemical Vapor Deposition.* Thin Solid Films, 1976. **35**: p. 201.

47. Margulies, D. T., Parker, F. T., Rudee, M. L., Spada, F. E., Chapman, J. N., Aitchison, P. N. and Berkowitz, A. E., *Origin of the Anomalous Magnetic Behavior in Single Crystal Fe_3O_4 Films.* Physical Review Letters, 1997. **79**: p. 5162.

48. Margulies, D. T., Parker, F. T., Spada, F. E., Goldman, R. S., Li, J., Sinclair, R. and Berkowitz, A. E., *Anomalous Moment and Anisotropy Behavior in Fe_3O_4 Films.* Physical Review B, 1996. **53**: p. 9175.

49. Eerenstein, W., Palstra, T. T. M., Hibma, T. and Celotto, S., *Diffusive Motion of Antiphase Domain Boundaries in Fe_3O_4 Films.* Physical Review B, 2003. **68**: p. 014428.

50. Kurtz, R. L., Karunamuni, J. and Stockbauer, R. L., *Synthesis of Epitaxial Fe_3O_4 Films on Cu(001).* Physical Review B, 1999. **60**: p. R16342.

51. Weiss, W. and Ritter, M., *Metal Oxide heteroepitaxy: Stranske-Krastanov Growth for Iron Oxides on Pt(111).* Physical Review B, 1999. **59**: p. 5201.

52. Morrall, P., Schedin, F., Langridge, S., Bland, J., Thomas, M. F. and Thornton, G., *Magnetic Moment in An Ultrathin Magnetite Film.* Journal of Applied

Physics, 2003. **93**: p. 7960.

53. Schedin, F., Hewitt, L., Morrall, P., Petrov, V. N., Thornton, G., Case, S., Thomas, M. F. and Uzdin, V. M., *In-plane Magnetization of An Ultrathin Film of Fe_3O_4(111) grown epitaxially on Pt(111).* Physical Review B, 1998. **58**: p. R11861.

54. Soeya, S., Hayakawa, J., Takahashi, H., Ito, K., Yamamoto, C., Kida, A., Asano, H. and Matsui, M., *Development of Half-Metallic Ultrathin Fe_3O_4 Films for Spin-Transport Devices.* Applied Physics Letters, 2002. **80**: p. 823.

55. Matsuda, H., Takeuchi, M., Adachi, H., Hiramoto, M., Matsukawa, N., Odagawa, A., Setsune, K. and Sakakima, H., *Fabrication and Magnetoresistance Properties of Spin-Dependent Tunnel Junctions Using an Epitaxial Fe_3O_4 Film.* Japanese Journal of Applied Physics, 2002. **41**: p. L387.

56. Huang, P. H., Lai, C. H. and Huang, R. T., *Room-Temperature Growth of Epitaxial (111) Fe_3O_4 Films with Conductive Cu Underlayer.* Journal of Applied Physics, 2005. **97**: p. 10C311.

57. Takahashi, H., Soeya, S., Hayakawa, J., Ito, K., Kida, A., Yamamoto, C. and Matsui, M., *Fabrication and Magnetoresistive Effect of Current Perpendicular to Plan Devices Using Half-Metallic Fe_3O_4 Thin Films on Metallic Films.* Journal of Applied Physics, 2003. **93**: p. 8029.

58. Kennedy, R. J. and Stampe, P. A., *Fe_3O_4 Films Grown by Laser Ablation on Si(100) and GaAs(100) Substrates with and without MgO Buffer Layers.* Journal of Physics D: Applied Physics, 1999. **32**: p. 16.

59. Ogale, S. B., Ghosh, K., Pai, S. P., Robson, M., Li, E., Jin, I., Greene, R. L., Ramesh, R., Venkatesan, T. and Johnson, M., *$Fe_3O_4/SrTiO_3/La_{0.7}Sr_{0.3}MnO_3$ Heterostructure: Growth and Properties.* Materials Science and Engineering: B, 1998. **56**: p. 134.

60. Sena, S. P., Lindley, R. A., Blythe, H. J., Sauer, C., Al-Kafarji, M. and Gehring, G. A., *Investigation of Magnetite Thin Films Produced by Pulsed Laser Deposition.* Journal of Magnetism and Magnetic Materials, 1997. **176**: p. 111.

61. Anderson, J. F., Kuhn, M., Diebold, U., Shaw, K., Stoyanov, P. and Lind, D., *Surface Structure and Morphology of Mg-Segregated Epitaxial Fe_3O_4(001) Thin Films on MgO(001).* Physical Review B, 1997. **56**: p. 9902.

62. Shaw, K. A., Lochner, E. and Lind, D. M., *Interdiffusion Study of Magnesium in Magnetite Thin Films Grown on Magnesium Oxide (001) Substrates.* Journal of Applied Physics, 2000. **87**: p. 1727.

63. Schedin, F., Hill, E. W., van der Laan, G. and Thornton, G., *Magnetic Properties of Stoichiometric and Nonstoichimetric Ultrathin Fe_3O_4(111) films on Al_2O_3(0001).* Journal of Applied Physics, 2004. **96**: p. 1165.

64. Nikiforov, M. P., Vertegel, A. A., Sumsky, M. G. and Switzer, J. A., *Epitaxial Electrodeposition of Fe_3O_4 on Single-Crystal Au(111).* Advanced Materials, 2000. **12**: p. 1351.

65. Sorenson, T. A., Morton, S. A., Waddill, G. D. and Switzer, J. A., *Epitaxial Electrodeposition of Fe_3O_4 Thin Films on the Low-Index Planes of Gold.* Journal of the American Chemical Society, 2002. **124**: p. 7604.

66. Bockris, J. O. M., Bonciocat, N. and Gutmann, F., *An Introduction to Electrochemical Science*. 1974, London: Wykeham Publications Ltd.

67. Newman, J. S., *Electrochemical Systems*. 2nd ed. 1991, New Jersey: Prentice Hall.

68. Mehl, W. and Bockris, J. O. M., *Mechanism of Electrolytic Silver Deposition and Dissolution.* Journal of Chemical Physics, 1957. **27**: p. 818.

69. Despic, A. R. and Bockris, J. O. M., *Kinetics of the Deposition and Dissolution of Silver.* Journal of Chemical Physics, 1960. **32**: p. 389.

70. Rashkov, S., Stoichev, D. S. and Tomov, I., *Influence of Current Density and Temperature on the Morphology and Preferred Copper Coatings.* Electrochimica Acta, 1972. **17**: p. 1955.

71. Switzer, J. A., Kothari, H. M. and Bohanna, E. W., *Thermodynamic to Kinetic Transition in Epitaxial Electrodeposition.* Journal of Physical Chemistry B, 2002. **106**: p. 4027.

72. Kern, W. and Puotinen, D. A., *Cleaning Solution Based on Hydrogen Peroxide for Use in Silicon Semiconductor Technology.* RCA Review, 1970. **31**: p. 187.

73. Binning, G. and Quate, C. F., *Atomic Force Microscope.* Physical Review Letters, 1986. **56**: p. 930.

74. Bonnell, D., *Scanning Probe Microscopy and Spectroscopy*. 2nd ed. 2001, Canada: Wiely-VCH, Inc.

75. Zworykin, V. K., Hiller, J. and Snyder, R. L., *A Scanning Electron Microscope.* ASTM Bulletin, 1942. **117**: p. 15.

76. Goldstein, J. I., Newbury, D. E., Echlin, P., Joy, D. C., A. D. Romig, J., Lyman, C. E., Fiori, C. and Lifshin, E., *Scanning Electron Microscopy and X-Ray Microanalysis*. 2nd ed. 1992, New York and London: Plenum Press.

77. Russ, J. C., *Fundamentals of Energy Dispersive X-Ray Analysis*. 1984: Butterworths & Co Ltd.

78. Cullity, B. D. and Stock, S. R., *Elements of X-Ray Diffraction*. 3rd ed. 2001, Upper Saddle River, New Jersey: Prentice Hall.

79. Williams, D. B. and Carter, C. B., *Transmission Electron Microscopy: Basics*. Vol. I. 1996, New York: Springer Science+Business media, Inc.

80. Foner, S., *Vibrating Sample Magnetometer.* The Review of Scientific Instruments, 1956. **27**: p. 548.

81. Foner, S., *The Vibrating Sample Magnetometer: Experiences of A Volunteer.*

Journal of Applied Physics, 1996. **79**: p. 4740.

82. http://www2.slac.stanford.edu/vvc/experiments/spear.html.

83. Birkholz, M., *Thin Film Analysis by X-ray Scattering*. 2006, Weinheim: Wiley-VCH.

84. Kronig, R. d. L., *Zur Theorie der Feinstruktur in den Rontgen-absorptionsspektren.* Zeitschrift Für Physik A, 1931. **70**: p. 317.

85. Stern, E. A., *Theory of the Extended X-ray-absorption Structure.* Physical Review B, 1974. **10**: p. 3027.

86. Teo, B. K. and Joy, D. C., *EXAFS Spectroscopy, Techniques and Application*. 1981, New York: Plenum Press.

87. Bianconi, A., *Surface X-ray Absorption Spectroscopy: Surface EXAFS and Surface XANES.* Applications of Surface Science, 1980. **6**: p. 392.

88. Kincaid, B. M. and Eisenberger, P., *Synchrotron Radiation Studied of the K-Edge Photoabsorption Spectra of Kr, Br2 and $GeCl_4$: A Comparision of Theory and Experiment.* Physical Review Letters, 1975. **34**: p. 1361.

89. Erskine, J. L. and Stern, E. A., *Calculation of the M_{23} Magneto-Optical Absorption Spectrum of Ferromagnetic Nickel.* Physical Review B, 1975. **12**: p. 5016.

90. Thole, B. T., van der Laan, G. and Sawatzky, G. A., *Strong Magnetic Dichroism Predicted in the $M_{4,5}$ X-Ray Absorption Spectra of Magnetic Rare-Earth Materials.* Physical Review Letters, 1985. **55**: p. 2086.

91. Chen, C. T. and Sette, F., *Performance of the Dragon Soft X-ray Beamline.* Review of Scientific Instruments, 1989. **60**: p. 1616.

92. Misawa, T., *The Thermodynamic Consideration For Fe-H_2O System at 25^{o}C.* Corrosion Science, 1973. **13**: p. 659.

93. Abe, M., *A Soft Solution Processing Technique for Preparing Ferrite Films*

and Their Applications. MRS Bulletin, 2000. **25**: p. 51.

94. Lincot, D., *Electrodepositon of Semiconductors.* Thin Solid Films, 2005. **487**: p. 40.

95. Cullity, B. D., *Introduction to Magnetic materials*. 1972, London: Addison-Wesley.

96. Nedkov, I., Merodiiska, T., Kolev, S., Krezhov, K., Niarchos, D., Moraitakis, E., Kusano, Y. and Takada, J., *Microstructure and Magnetic Behaviour of Nanosized Fe_3O_4 Powders and Polycrystalline Films.* Monatshefte für Chemie, 2002. **133:** p. 823.

97. Kothari, H. M., Kulp, E. A., Limmer, S. J., Poizot, P., Bohannan, E. W. and Switzer, J. A., *Electrochemical Deposition and Characterization of Fe_3O_4 Films Produced by the Reduction of Fe(III)-Triethanolamine.* Journal of Materials Research, 2006. **21:** p. 293.

98. Kostov, I., *Mineralogy.* 1968, Edinburgh and London: Oliver and Boyd.

99. Porter, D. A. and Easterling, K. E., *Phase Transformations in Metals and Alloys.* 2nd ed. 1992, London: Chapman & Hall.

100. Teng, C. L. and Ryan, M. P., *A Morphological Study of Nanocrystalline Magnetite Electrodeposited onto Polycrystalline Copper Substrates.* Electrochemical and Solid-State Letters, 2007. **10:** p. D108.

101. Mavropoulos, Ph., Papanikolaou, N. and Dederichs, P. H., *Complex Band Strucuture and Tunneling through Ferromagnet/Insulator/Ferromagnet Junctions.* Physical Review Letters, 2000. **85:** p. 1088.

102. Parkin, S. S. P., Kaiser, C., Panchula, A., Rice, P. M., Hughes, B., Samant, M. and Yang, S., *Giant Tunnelling Magnetoresistance at Room Temperature with MgO(100) Tunnel Barriers.* Nature Materials, 2004. **3:** p. 862.

103. Génin, J., Bourrié, G., Trolard, F., Abdelmoula, M., Jaffrezic, A., Refait, P.,

Maitre, V., Humbert, B. and Herbillon, A., *Thermodynamic Equilibria in Aqueous Suspensions of Synthetic and Natural Fe(II)-Fe(III) Green Rusts: Occurences of the Mineral in Hydromorphic Soils.* Environmental Sciences & Technology, 1998. **32:** p. 1058.

104. Antony, H., Peulon, S., Legrand, L. and Chaussé, A., *Electrochemical Synthesis of Lepidocrocite Thin Films on Gold Substrate-EQCM, IRRAS, SEM and XRD Study.* Electrochimica Acta, 2004. **50:** p. 1015.

105. Martinez, L., Leinen, D., Martin, F., Gabas, M., Ramos-Barrado, J. R., Quagliata, E. and Dalchiele, W. A., *Electrochemical Growth of Diverse Iron Oxide (Fe_3O_4, α–FeOOH and γ–FeOOH) Thin Films by Electrodeposition Potential Tuning.* Journal of the Electrochemical Society, 2007. **154:** p. D126.

106. Cornell, R. M., Giovanoli, R. and Schindler, P. W., *Effect of Silicate Species on the Transformation Ferrihydrite into Geothite and Hematite in Alkaline Media.* Clays and Clay Minerals, 1987. **35:** p. 21.

107. Fuggle, J. C. and Inglesfield, J. E., *Unoccupied Electronic states.* 1992, Berlin: Springer-Verlag.

108. Newville, M., Līviņš, P., Yacoby, Y., Rehr, J. J. and Stern, E. A., *Near-Edge X-Ray-Absorption Fine Structure of Pb: A Comparison of Theroy and Experiment.* Physical Review B, 1993. **47:** p. 14126.

109. Parratt, L. G., *X-Ray Resonance Absorption Lines in the Argon K Spectrum.* Physical Review, 1939. **56:** p. 295.

110. Tossell, J. A., Vaughan, D. J. and Johnson, K. H., *The Electronic Structure of Rutile, Wustite and Hematite from Molecular Orbital Calculations.* American Mineralogist, 1974. **59:** p. 319.

111. Waychunas, G. A., Apted, M. J. and Brown, Jr., G. E., *X-Ray K-Edge Absorption Spectra of Fe Minerals and Model Compounds: Near-Edge*

Structure. Physics and Chemistry of Minerals, 1983. **10:** p. 1.

112. Srivastava, U. C. and Nigam, H. L., *X-Ray Absorption Edge Spectrometry (XANES) as Applied to Coordination Chemistry.* Coordination Chemistry Reviews, 1973. **9:** p. 275.

113. Davenport, A. J. and Sansone, M., *High Resolution In Situ XANES Investigation of the Nature of the Passive Film on Iron in a pH 8.4 Borate Buffer.* Journal of the Electrochemical Society, 1995. **142:** p. 725.

114. Combes, J. M., Manceau, A., Calas, G. and Bottero, J. Y., *Formation of Ferric Oxides from Aqueous Solution: A Polyhedral Approach by X-Ray Absorption Spectroscopy: I. Hydrolysis and Formation of Ferric Gels.* Geochimica et Cosmochimica Acta, 1989. **53:** p. 583.

115. Maruyama, H., Harada, I., Kobayashi, K. and Yamazaki, H., *Magnetic Circular X-Ray Dichroism at Fe K-Edge in Ferrimagnetic Fe-Oxides.* Physica B, 1995. **208/209:** p. 760.

116. Wilke, M., Farges, F., Petit, P., Brown, Jr., G. E. and Martin, F., *Oxidation State and Coordination of Fe in Minerals: An Fe K-XANES spectroscopic Study.* American Mineralogist, 2001. **86:** p. 714.

117. Huang, D. J., Chang, C. F., Jeng, H.-T., Guo, G. Y., Lin, H.-J., Wu, W. B., Ku, H. C., Fujimori, A., Takahashi, Y. and Chen, C. T., *Spin and Orbital Magnetic Moments of Fe_3O_4.* Physical Review Letters, 2004. **93:** p. 077204-1.

118. Krasnikov, S. A., Vinogradov, A. S., Hallmeier, K.-H., Höhne, R., Ziese, M., Esquinazi, P., Chassé, T. and Szargan, R., *Oxidation Effects in Epitaxial Fe_3O_4 Layers on MgO and $MgAl_2O_4$ substrates Studied by X-ray Absorption Fluorescence and Photoemission.* Materials Science and Engineering: B, 2004. **109:** p. 207.

119. Kuiper, P., Searle, B. G., Rudolf, P., Tjeng, L. H. and Chen, C. T., *X-Ray*

Magnetic Dichroism of Antiferromagnet Fe_2O_3: The Orientation of Magnetic Moments Observed by Fe 2p X-Ray Absorption Spectroscopy. Physical Review Letters, 1993. **70:** p. 1549.

120. Pellegrin, E., Hagelstein, M., Doyle, S., Moser, H. O., Fuchs, J., Vollath, D., Schuppler, S., James, M. A., Saxena, S. S., Niesen, L., Rogojanu, O., Sawatzky, G. A., Ferrero, C., Borowski, M., Tjernberg, O., and Brookes, N. B., *Characterization of Nanocrystalline γ–Fe_2O_3 with synchrotron Radiation Techniques.* Physica Status Solidi, Section B: Basic Research, 1999. **215:** p. 797.

121. van der Laan, G. and Kirkman, I. W., *The 2p Absorption Spectra of 3d Transition Metal Compounds in Tetrahedral and Octahedral Symmetry.* Journal of Physics: Condensed Matter, 1992. **4:** p. 4189.

122. Pong, W. F., Chang, Y. K., Su, M. H., Tseng, P. K., Lin, H. J., Ho, G. H., Tsang, K. L. and Chen, C. T., *Magnetic Orientation of Ni in Zn-Ni Ferrite Studied by Soft-x-ray Magnetic Circular Dichroism.* Physical Review B, 1997. **55:** p. 11409.

123. Kuiper, P., Searle, B. G., Duda, L.-C., Wolf, R. M. and van der Zaag, P. J., *Fe $L_{2,3}$ Linear and Circular Magnetic Dichroism of Fe_3O_4.* Journal of Electron Spectroscopy and Related Phenomena, 1997. **86:** p. 107.

124. Forsyth, J. B., Hedley, J. G. and Johnson, C. E., *The Magnetic Structure and Hyperfine Field of Goethite (α–FeOOH).* Journal of physics C: Proceedings of the Physical Society: Solid State Physics, 1968. **1:** p. 179.

125. Johnson, C. E., A*ntiferromagnetism of γ-FeOOH: a Mossbauer Effect Study.* Journal of physics C: Proceedings of the Physical Society: Solid State Physics, 1969. **2:** p. 1996.

126. Chatman, S., Noel, A. and Poduska, K., *Tuning Magnetic Hysteresis of*

Electrodeposited Fe_3O_4. Journal of Applied Physics, 2005. **98:** p. 113902.

127. Butler, R. F. and Banerjee, S. K., *Theoretical Single-Domain Grain Size Range in Magnetite and Titanomagnetite.* Journal of Geophysical Research, 1975. **80:** p. 4049.

128. Liu, H., Jiang, E. Y., Bai, H. L., Zheng, R. K. and Zhang, X. X., *Thickness Dependence of Magnetic and Magneto-Transport Properties of Polycrystalline Fe_3O_4 Films prepared by Reactive Sputtering at Room Temperature.* Journal of Physics D: Applied Physics, 2003. **36:** p. 2950.

129. Matsumoto, K., Kim, S., Wen, J. and Hirabayashi, I., *Fabrication of In-Plane Aligned YBCO Films on Polycrystalline Ni Tapes Buffered with Surface-Oxidized NiO Layers.* IEEE Transactions on Applied Superconductivity, 1999. **9:** p. 1539.

130. Hinds, G., Coey, J. M. D. and Lyons, M. E. G., *Influence of Magnetic Forces on Electrochemical Mass Transport.* Electrochemistry Communications, 2001. **3:** p. 215.

131. Tabakovic, I., Riemer, S., Vas'ko, V., Sapozhnikov, V. and Kief, M., *Effect of Magnetic Field on Electrode Reactions and Properties of Electrodeposited NiFe Films.* Journal of the Electrochemical Society, 2003. **150:** p. C635.

132. Wang, J., Chen, W., Zeng, C. and Hou, B., *Magnetic-Field-Induced Growth of Single-Crystalline Fe_3O_4 Nanowires.* Advanced Materials, 2004. **16:** p. 137.

133. Mitov, I., Paneva, D. and Kunev, B., *Comparative Study of the Thermal Decomposition of Iron Oxyhydroxides.* Thermochimica Acta, 2002. **386:** p. 179.

134. Schiessl, W., Potzel, W., Karzel, H., Steiner, M., Kalvius, G. M., Martin, A., Krause, M. K., Halevy, I., Gal, J., Schafer, W., Will, G., Hillberg, M., and Wappling, R., *Magnetic Properties of the $ZnFe_2O_4$ Spinel.* Physical Review B,

1996. **53:** p. 9143.

135. Taheri, M., Carpenter, E. E., Cestone, V., Miller, M. M. and Raphael, M. P., *Magnetism and Structure of $ZnxFe_{3-x}O_4$ Films Processed via Spin-Spray Deposition.* Journal of Applied Physics, 2002. **91:** p. 7595.